1 Answers to reviewer 1

First, we thank reviewer 1 for the positive attitude to continuing model developments of MPI-ESM. It is however true that there will be no further developments on MPI-ESM1.2 (all effort is on the new ICON model), except for advanced vertical mixing schemes in the ocean, which have considerable effects on the ocean circulation that might become of importance also for other high-resolution earth system models.

1. RC1: "Regarding MPIOM in the middle of the chapter 2.1 describing the setups I was surprised by the choice of the the GM coefficient which is 250 m2s-1 for 400 km cell width. I find this value too small as compared to what is practiced by other models. For instance, in paper by Marshall, J et at. 2017 which is cited by the authors the value of 850 m2/s is reported for 1° resolution in the control run. The same, although not that extend, is true for the Redi diffusion. All this implies that the mesoscale eddies are basically neither parameterized nor resolved in simulations denoted with HR and XR. Going through other papers using MPIOM I found that the choice made by the authors is indeed canonical for this model. From this one may conclude that the baroclinic instability in low resolution setups is "indirectly parameterized" by some diabatic processes taking place in the model. These can be for instance the explicitly specified or numerical diffusion. According to Marshall, J et al. 2017 the MOC/AMOC are far too large when the small values are used although in the ocean only configurations."

AC: There are two reasons why we chose a value of 250 m2s-1 for a 400km grid cell for the GM coefficient. First, we did not want to change this GM-parameter to be consistent with previous MPI-ESM simulations. Second, the GM coefficient was used to tune the strength of the AMOC, which was too weak in the TP04 configuration when higher values were used (as mentioned by von Storch et al. 2016). Finding an optimal configuration is, however, challenging for intermediate resolutions and is tackled differently by individual modelling centres. We note that mesoscale variability (eddies) is partly resolved and partly parameterized in our HR/XR models, which can be seen by looking at e.g. eddy kinetic energy.

We admit that the GM coefficient is lower compared to what is used by Marshall et al. (2017); however, there are strategies to turn off the GM parameterization completely for such hybrid resolutions (see for instance the GFDL model, where the GM parameterization was switched off (Delworth et al., 2012; doi=10.1175/JCLI-D-11-00316.1). In fact, Treguier (2006; Ch.3 in Chassignet and Verron (Eds.) Ocean Weather forecasing, p.100-102) discusses this issue. Although a full GM parameterization is justified for e.g. a 1/3° model, for instance in the Labrador Sea, it is not suited for all parts of the ocean because of the varying Rossby radius. A value of 800 m2s-1 for instance would destroy the eddy activity in the Gulf Stream. Thus it is still an open question how to represent the unresolved mesoscale eddy spectrum in eddy-permitting ocean models. MPIOM uses a weighted average of both central-differences and upstream methods (Marsland, 2003). It exploits the benefits of the upstream scheme to limit spurious tracer sources and sinks, while it avoids numerical diffusion in areas with strong gradients in the tracer field. Usually the central-differences scheme has more weight, except in cases where strong gradients occur. In such a case, the numerical mixing might still be too large. However, as mentioned above, the resulting AMOC is in good agreement with observations, so that we did not change the GM coefficients for our simulations.

2. RC1: "XRpp is characterized by a very small AMOC due to very low winds in ECHAM/T255 and associated collapse of the deep convection in the Labrador Sea. A similar behaviour regarding Labrador Sea MLD collapse has already been reported for several completely different climate models. In line 21, page 8 the authors discard the effect from the Southern Hemisphere saying that the collapse happens on a fast timescale. Although I tend to believe that the authors are right one still could speculate that the time range from 50 to 100 years is already not that fast. The colorbar range in Figure 5 is huge but one could see that the cold bias over ACC is coincidently the largest in XRpp. Alternatively one may look at the difference between subplots in Figure 8 to see whether the slope of the halocline in the SO changes between simulations. Otherwise it is hard to guess it by eye. How do the interranual timeseries of the MLD in the Labrador Sea look like? After which year does the first Labrador Sea MLD collapse happen?"

AC: We discard the Southern Ocean (SO) to be the reason for the collapse of the AMOC and rely on the study of Putrasahan et al. 2019 (JAMES, now accepted, doi: 10.1029/2018MS001447), who explicitly demonstrated that the SO is not the reason for the collapse. We did not go into details here, because the Putrasahan et al. paper is all on exploring the collapse of the Labrador Sea convection that occurs within the first 20 years of the simulation (Fig.7 in their manuscript). Unfortunately, the Putrasahan et al. paper was not publically accessible at the time we wrote our manuscript. A brief note on the topic: the weaker westerlies over the SO decrease the upwelling in the SO which in turn reduces the return flow and thus the AMOC strength. In their paper, they performed a sensitivity simulation in which the wind bias over the SO was corrected (by adding the mean wind stress from HR) to test this hypothesis. As a result, they find only a negligible effect from the SO and conclude that biases from the SO might affect the AMOC only on longer time-scales, but not within a few decades. From Fig. A8 (revised manuscript; A4 in the first submission), we conclude that the slopes of the halocline are similar in all HR and XR simulations, only in ER is the slope less steep, which better agrees with EN4 data. Additionally, the cold bias in the SO remains even when using KPP in the XR setup, which indicates that the sensitivity of deep convection in the Labrador Sea is mainly responsible for the stability of the AMOC in XR. The time series of the mixed layer depth in the Labrador Sea (averaged over 58-48◦W, 55-65◦N, attached Fig. 1) show that the mixed layers in XR-PP are shallower than in HRpp in the first two decades, and drop to almost zero afterwards.

3. RC1: "In Figure 9 I would expect to see the sea ice in the Labrador Sea in XRpp. Is it masked by the choice of colorbar. Honestly, I would add even more material regarding the Labrador Sea collapse as it has been often discussed in literature. See for instance the paper by Moriaki Yasuharaet al. 2008 in PNAS titled as “Abrupt climate change and collapse of deep-sea ecosystems”."

AC: Thank you very much for this comment. We have added the contour lines for the 15% sea-ice concentration from the simulations (magenta) and from the EUMETSAT OSI SAF observational product (dark blue) to Fig. 9 (attached Fig. 2). We also have slightly adjusted the colour bar range. We decided to not include a discussion of the impacts of a Labrador Sea deep-convection collapse into the manuscript, because it is not the topic for this overview manuscript. Thus, although the Yasuharaet et al. 2008 paper is of interest for sure, it is too specific (ecosystems) for our purpose.

4. RC1: "The authors solved the problem with too cold North Atlantic in XRpp by changing the mixing scheme from PP to KPP. I speculate that it would be sufficient to increase the upper mixing coefficient in PP to parameterize for the wind induced turbulence but still encourage using KPP as there is more physics in it."

AC: Although we did not explicitly perform such an experiment, we think it will not solve the collapse. Putrasahan et al. performed a sensitivity experiment where they increased the wind stress received by the ocean by a factor of 1.5, which is comparable to increasing the wind mixing part of the PP scheme. It did however not rescue the AMOC. Therefore, and because the KPP scheme was on our agenda anyways, we decided to only perform a KPP simulation with XR. We speculate that the non-local transport terms in KPP better reflects the convection (probably due to entrainment of salt in the upper ocean during absence of wind forcing) than the enhanced wind-mixing parameterization for the upper ocean diffusivity used with the PP scheme. Furthermore, the diffusivity in the KPP scheme also depends on the mixed layer depth to reflect that boundary layer eddies become larger with deeper mixed layers. This dependency might further cause higher diffusivities than with the PP scheme, which then sustains sufficient mixing and convection in the Labrador Sea.

5. RC1: "Even though XRkpp is a reasonable simulation, the NADW is still not as well simulated as in ERpp where the bottom cell in AMOC is nicely visible (Fig. 12). Most probably, playing with GM is still required in order to further improve the quality of XRkpp. So far if all I wrote above regarding GM is correct, ERpp is the only simulation which physically consistent deals with the baroclinic instability. Surprisingly, ERpp looks fine even with PP."

AC: That is correct; the bottom cell is well simulated in ERpp. A comparison with HRpp suggests that the higher ocean resolution improves the bottom cell, while the KPP scheme does not. Both use the same atmosphere (T127) which does not produce the negative wind bias of the T255 atmosphere, so that a stable AMOC is simulated also with the PP scheme. It is likely that further retuning (including GM) is required for the XRkpp to improve the bottom cell; however, the HighResMIP protocol has a strong preference for not retuning of the models in order to see the pure effects coming from either increased resolution or improved phyiscs (KPP scheme in our case). This procedure received a consensus by all modelling groups within the HighResMIP. If not, the effect of subgrid-scale parameterization of ocean eddies would obscure the effect and benefit of higher model resolution.

6. RC1: "In addition to showing the differences to climatology at the surface I would also suggest to plot these differences at other depths (1000 or 2000 meters). The drawback of using KPP might be that it propagates the model error further to the deeper ocean than it was with PP."

AC: We plotted the temperature and salinity bias (attached) at 1000m and 2000m depth (see attached Fig. 3 and Fig. 4). As also shown in Fig. 7 and Fig. 8 in the manuscript (zonal mean transects), the bias at depth is of similar magnitude in XRkpp and XRpp. However, at 1050m depth (attached Fig. 3) both HRkpp and XRkpp enhance the warm bias in the Southern Ocean around 30◦S and in the Indian Ocean and Pacific. In the North Atlantic, however, the bias is similar to HRpp. At 2080m depth (attached Fig. 4) the difference of the bias between PP and the KPP simulations is much smaller. Concerning salinity, the bias of HRpp and HRkpp are comparable, with HRkpp slightly saltier in the subpolar gyre and in the GIN seas (attached Fig. 5). Although similar for large parts of the ocean, the positive salinity bias in XRpp is, however, slightly less in than in XRkpp. This salinity reduction along with a reduced wind forcing is then the reason for the collapse of deep-convection in the Labrador Sea. In addition, the Arctic Ocean freshens in XRpp, so that also more freshwater is exported into the North Atlantic, further reducing the deep-convection. At 2080m depth (attached Fig. 6) the salinity bias mostly vanishes, except for a positive bias in the subpolar gyre. The bias is slightly stronger in the HR and XR simulations with KPP, which might be due to saltier Mediterranean outflow waters into the North Atlantic. It certainly helps to sustain deep-convection in the subpolar gyre in addition to the physically more realistic KPP scheme convection.

7. RC1: "I would suggest the authors to elaborate a bit more on the text considering what I have written above. It will be not that descriptive then. The text is easy to read but I would recommend that some native speaker will read it. I found sentences containing things like “cold bias in the North Atlantic improves” in the text."

AC: Thank you very much, we will add content following your comments and we hope we did correct the flaws in the text.

2 Answers to reviewer 2

We thank the reviewer for the constructive comments and thorough reading of our manuscript.

2.1 Major comment

1. RC2: "The paper starts by discussing wind, Tair and SST biases etc., and refers to many results shown later in the paper, such as the following in section 3.1.2: line 2 of page 6 "and briefly outlined in section 4" line 18-19 North Atlantic Current (section 4.1.1) line 25 (see section 4.5) line 29-30 (see section 4) The references to later in the paper are not ideal, and I think it would read better if either i) these references were removed or, probably much better, ii) the paper re-arranged. As many properties are related to AMOC, you could start with a discussion of the ocean circulation (4.3) followed by 4.6 (AMOC) followed by 4.5 (Mixed layer Depth) followed by 4.4 (Sea ice). Then perhaps describe the rest of the ocean state (sections 4.1, 4.2) and then move to section 3 (Atmosphere state). Hopefully this or something similar would make the paper flow better."

AC: In our initial draft (before submission), we used a structure as you propose. In the course of writing however, we changed the structure to what it is now. The reason is that from a narrative point of view, we find it easier to follow when the atmosphere is described first, with its reduction of the near-surface wind speeds in the XR setup, which is independent of the ocean vertical mixing scheme or the resolution of the underlying ocean model. This wind reduction then forms the base from which we develop the collapse of the AMOC with the PP scheme, while with KPP the AMOC remains stable. However, as we are dealing with coupled models, it is hard to avoid anticipating any information that is presented in detail later in the text. For instance, if we began describing the AMOC slowdown, we would have to anticipate that wind forcing reduces with T255, which is then shown in a later section. We are grateful to the reviewer for thinking the structure of the paper through and giving us these suggestions. In the end it is probably a matter of personal taste where to describe the complex coupled system. We hope this explains why we started with the atmosphere. You can rest assured that we have long thought about the structure of the paper. The initial references to later in the paper may not be ideal, but together with the additional information we provide at this stage, it is sufficient information to understand the consequences for the atmosphere, and it prepares the reader for what to expect in the course of the manuscript.

2.2 Minor comments

1. RC2: "As the acronyms for model resolution are a bit hard to follow, you should refer to Table 1 much earlier, on page 2 (section 1) and again in 2.1. You may also want to clearly state: "atmosphere resolution is contrasted between HR and XR: ocean resolution between HR and ER or between XR and ER: ocean mixing physics between pp and kpp."

AC: We agree and we now refer to Table 1 much earlier (first half of Introduction) and make explicitly clear what the difference is between the settings (summary at the end of the Introduction).

2. RC2: "Page 5, lines 9-10. "diffusivities not matched at base of mixed layer" Do you think that this has any adverse effects?"

AC: A match of the diffusivities at the base of the ocean boundary layer (OBL) in KPP allows that interior processes can influence the diffusivity within the OBL, which adds complexity to the KPP scheme. As this matching differs for every tracer, it also implicates that the non-dimensional shape function (G) in the KPP scheme is no longer a universal function, but depends on the field that is transported. In addition, it is not straightforward how to do this smoothing for a discretized vertical ocean grid. It also means that the non-local transport terms do not smoothly go to zero at the base of the mixed layer. In unfavourable conditions, it was found that the non-local fluxes can even become larger than the surface fluxes (Griffies, 2013) near the OBL base, even though they are supposed to just redistribute the surface fluxes in the vertical. This 'overshooting' then might produce extrema in the tracer field. One example where this might happen is when in unstable conditions below the OBL the enhanced diffusivity parameterization results in very large diffusivity just beneath the OBL. In that case a matching would result in a very large shape function (G > 1.0) at the base of the mixed layer. Although there are simpler techniques of matching, referring to Griffies (2013) they were not fully tested yet. For these reasons we decided to not match the diffusivities and accept that there might be jumps at the base of the boundary layer, if not both the OBL and the interior diffusivities go to zero at the OBL base. On the other hand, the OBL diffusivities are still influenced by processes related to shear at its base, as the calculation of the OBL depth in KPP involves the resolved and turbulent shear in the Richardson number. One such area is for instance the equatorial Pacific where the near-surface underlying Equatorial Undercurrent has a strong vertical shear that might deepen the OBL and with that enhance the OBL diffusivities, which are a non-local function of OBL depth (and other OBL properties).

3. RC2: "line 20. Presumably you refer to the time mean of scalar wind speed, not the magnitude of the time-mean wind vector?"

AC: Yes we refer to the scalar wind speed here. We have revised the sentence accordingly.

4. RC2: "line 26. Changes in subtropics are very small, perhaps delete the comment."

AC: We agree the change is very small, and have deleted the sentence.

5. RC2: "page 6, line 18 "partly caused" - I don't think it is solely the NAC problem."

AC: Yes, absolutely correct. We add your suggestion, and we have added additional reasons for the SST cold bias in the extratropical NA: "Here, all simulations show a cold bias, which is a common error in state-of-the-art ESMs (Randall et al., 2007), which is mostly caused by a too zonal North Atlantic Current (NAC) (Dengg et al., 1996), or by insufficient northward heat transport by the AMOC (Wang et al., 2014a). Drews et al. (2015) demonstrated that correcting the flow field for biases removed the cold bias in the North Atlantic."

6. RC2: "page 7, line 1. I think it should be compared to HRpp, not HRkpp."

AC: That is true, we have revised and restructured the sentence.

7. RC2: "line 19. "does not modify the mean zonal wind " where are you referring to?"

AC: There is a missing part in that sentence for which we apologize. We have revised this paragraph and the one before to clarify our statements.

8. RC2: "line 25. Another reference to a later section..."

AC: See our general comment to the major point on structure above.

9. RC2: "Fig. 4. Please add more contour levels to b-f), such as some combination of +/- 0.25, 0.5, 0.75K.

AC: We have added more contour lines to the plot as you suggest (attached Fig. 7). While producing the new figure however, we noticed that we did process only the zonal mean bias over the Atlantic, and not the global zonal-mean as intended. Thus, we replaced the figure with the correct one (attached Fig. 1). Same error happened for Fig. 3, which we corrected (attached Fig. 8). We have also modified the text in manuscript accordingly, in particular with respect to the cold bias above the Antarctic continent, which was cut off from the figure before.

10. RC2: "Line 28. "We conclude that eddies play a major role" - but it could be other processes, such as resolution of boundary currents, and eddies could play a direct or indirect (via effect on mean flow) effect."

AC: This is true, we rephrased the sentence emphasizing that the eddy-resolving resolution in general improves the mean-state of the ocean and atmosphere: “We conclude that an eddy-resolving ocean resolution plays a major role for the mean-states of the large-scale temperature distribution in the atmosphere.”

11. RC2: "page 9 lines 12-15. This explanation is not backed up by results (of salt transport). It could be put in Discussion."

AC: That is correct. We have inserted a supplement figure (Fig. A1 in revised manuscript; attached Fig. 9), showing the northward heat and salt transports at every latitude. The figure clearly shows the enhanced northward heat and salt transport in the KPP simulations.

12. RC2: "line 25 “less” to “little."

AC: We have corrected the sentence.

13. RC2: " line 26-29. It would be useful to include maps of precipitation (P) and evaporation (E) , or P-E to i) look at their biases and ii) see if they relate to ocean salinity bias."

AC: We have added P-E maps as a suppl. figure A2 in the revised manuscript (attached Fig. 10). All models simulate too little precipitation or too much evaporation, resulting in negative biases for most parts of the globe. However, in the western Pacific where the upper ocean is simulated much too fresh in the XR simulations, we do not see much of a difference to HR. On the contrary, the XR models simulate even less precipitation than the HR models. Thus our conclusion that too less salt is advected by the ocean currents.

14. RC2: "page 10, lines 8-12. We also see big effects of improving the Agulhas in our ocean simulation at different resolutions. I would like to see a map of the mean ocean currents (or just zonal velocity) in the Agulhas/Retroflection region in HR and XR and ER. Also, do you see similar changes (ER relative to HR/XR) in other basins? If not, it may discount the eddy-induced cooling hypothesis."

AC: We have plotted the velocity at 100m depth and the barotropic volume transport stream function of the Agulhas Current system (attached Fig. 11 and 12). ER-PP simulates a swifter and narrower Agulhas Current (attached Fig. 11) and a stronger retroflection (attached Fig. 12; this figure we included now as a suppl. figure (Fig. A8) in the revised manuscript), compared to the HR/XR simulations. This reduces the inflow of warm and salty water from the Indian Ocean into the South Atlantic, which is why the positive salinity bias at 500 to 700m depth is reduced in ER-PP (Fig. 8 of the manuscript). On the other hand, we notice that the simulations with KPP increase the inflow from the Indian Ocean, which is why both the warm bias and the salinity bias enhance slightly. In general, ER-PP simulates swifter and narrower boundary currents in all basins.

15. RC2: "Also, it may be useful to show (as Supp. Figs) the temperature and salinity biases globally at around 700m depth."

AC: We have added your suggested plots as supplement figures (Fig. A5 and A6 in the revised manuscript) (attached Fig. 13 and 14), and discuss these plots also in the manuscript.

16. RC2: "page 11 line 24. Delete "slightly", it looks large."

AC: We have removed ‘slightly’ from the sentence.

17. RC2: "line 26 add "compared to HRpp" at end of line."

AC: We have completed the sentence.

18. RC2: "line 32-33. I did not follow "explain the positive salinity bias in N. Atlantic" Where and why?"

AC: We have changed the sentence to ”In the case of HRkpp and XRkpp the too strong volume transport of the subtropical gyre might further contribute to the positive salinity bias in the subpolar gyre at a depth of 500 to 1000 m (Fig. 8 and Fig. A6).”

19. RC2: "Page 12 line 12. "model resolution or using KPP, which increase..".."

AC: We have corrected the sentence.

20. RC2: "Fig. 9 The Lab. Sea freeze-over is hard to see - the south-west labrador Sea has small sea ice volume. Perhaps you can also show sea-ice extent, if only for case XRpp? On this subject, other climate model centers have battled with Lab. Sea freeze-over. For example, in Community Earth System Model 2 development, several cases obtained freeze-over. CESM uses kpp. So, you show it is sensitive to using pp or kpp, while with CESM it seems to be very sensitive to run-off and surface salinity. (It is not fully understood)."

AC: That is true and we have added the 15% sea-ice extent contour line in Fig. 9 for all models (magenta) and from the EUMETSAT OSI SAF observational product (dark blue) (see attached Fig. 2). We have also slightly reduced the colourbar range. The freeze-over in XRpp is now clearly visible. We think that the Labrador freeze-over, although occurring across different models, is very model specific for its origin. In the XRpp the primary reason is the reduced wind forcing that results in a reduced salinity advection by the subpolar gyre into the Labrador Sea. Freshening from increased surface runoff seems not to play a major role in that respect and Putrasahan et al. could demonstrate that the collapse is caused because of the reduced wind stress and salt advection. In that sense, a too fresh upper ocean due to reduced salt input causes the freeze-over in MPI-ESM-XR. In our XRkpp setup, it seems that KPP maintains a stronger overturning, predominantly because of its non-local formulation and the addition of the non-local flux transports. These cause a stronger deep convection that in turn steepens the isopycnals in the Labradror Sea. The steeper ispoycnals sustain a sufficiently strong subpolar gyre, even though the wind forcing is weak, so that a sufficient amount of salt is advected into the Labrador Sea, where in turn the water column overturns due to negative buoyancy. Another aspect might be that our XR setup is probably in a transition zone, where the vertical mixing scheme is important for the AMOC stability. Nevertheless, we also found that the wind bias in ECHAM was resistant to tuning efforts (as shown in Putrasahan et al., 2019, now accepted, doi: 10.1029/2018MS001447), which is also not fully understood yet.

21. RC2: "page 15, line 2. "in XRkpp" compared to?"

AC: We have corrected the sentence to: “However, even with a T255 atmosphere the resolution is too coarse to fully simulate Greenland tip jets (e.g. Martin and Moore, 2007; DuVivier and Cassano, 2016; Gutjahr and Heinemann, 2018), which have a considerable impact on triggering deep convection in the Irminger Sea due to strong associated turbulent heat and momentum fluxes driving the Irminger Gyre, so that the mixed layer depth may be underestimated in winters with high tip jet activity.”

22. RC2: "Convection in the Labrador and Irminger Sea is governed by a number of complex factors in addition to those listed. The effect of eddies may be quite different in the eddy-permitting case than in the eddy-resolved case. An idea of the complexity of the eddies and convection can be found from Kawasaki and Hasumi 2014 (Ocean Modelling) and DuVivier et al 2016 (J. Climate)."

AC: We have added a sentence to the revised manuscript: “However, the processes that lead to deep convection in the Irminger Sea are complex, and it is still not fully understood how eddies affect the preconditioning/triggering of convection and where their main formation area is (Fan et al., 2013; DuVivier and Cassano, 2016).”

23. RC2: "Section 4.5.2. Although I understand you want to focus on high latitude convection and relationship to AMOC, it would also be interesting to look at MLD in the SubAntatarctic Frontal Zone (which ranges from latitudes of 40deg. in the South Indian Ocean to 60deg. near Drake Passage). Standard resolution models have a shallow MLD bias (Sallee et al 2013, DuVivier et al 2018, JGR Oceans https://doi.org/10.1029/2018JC014275) but there is a hint that high resolution models do better (Lee et al 2011, 24, 3830-3849, J. Climate, Li and Lee 2017, 47, 2755-2772, J. Climate.)"

AC: Thank you very much for this suggestion. We did not look too much into Southern Ocean mixed layer depths (apart from the very deep mixed layers simulated in the Weddell Sea in MPI-ESM1.2). However, we produced the mixed layer depths plots for the Subantarctic Frontal zone (attached Fig. 15), which we also added as a suppl. Fig. A10 to the revised manuscript. We used the same colors as in the Fig.2 of DuVivier et al. (2018) for a better comparison with the Argo floats MLDs. There clearly is a deepening of the mixed layers with the KPP scheme, probably due to the nonlocal transport terms as suspected by DuVivier et al. (2018), so that the boundary layer penetrates deeper into the stratified, salinity maximum at deeper layers. Further, the higher ocean resolution increases the MLDs as well while confining it to a narrower band, which is in better agreement with the observations from the Argo floats, as shown by DuVivier et al. (2018) (Fig. 2 therein). However, as also noted by DuVivier et al. (2018) for their higher resolved CESM simulation, the mixed layer depths are too deep compared to the Argo float observations. We have added a paragraph at the end of section 4.5.2 discussing these results.

24. RC2: "Page 17, line 32, “featuring reduced surface winds” where?"

AC: We have corrected the sentence to: “An important finding is that XRkpp simulates a stable AMOC (14.6 Sv), despite the weak wind stress with the T255 atmosphere.”

25. RC2: "Line 24. “winter upper layer”?"

AC: We have corrected the sentence.

26. RC2: "Page 19, line 15-16. This sentence is awkward. It could be reworded like “Cold temperature biases in the Southern Hemisphere, and to a lesser extent in the Northern Hemisphere, are reduced”."

AC: Thank you we have rephrased the sentence accordingly.

27. RC2: "Line 26-27. But doesn’t XRpp, with T255, have negligible MLD in the subpolar gyre?"

AC: You are correct, what we meant is in case of XRkpp. We have however rephrased the whole paragraph.

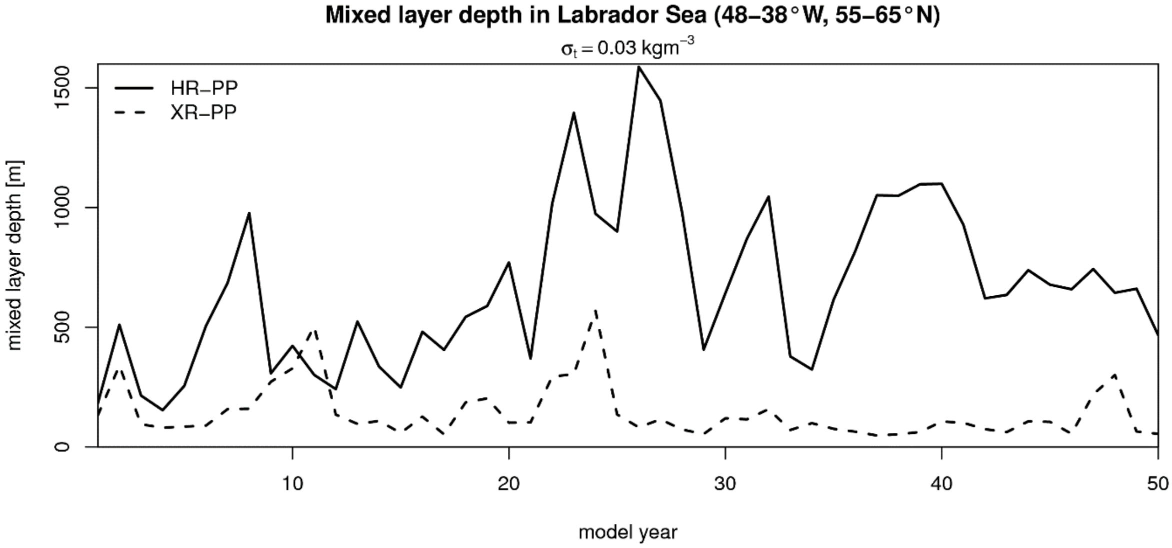

Fig. 1. Time series of the spatially averaged mixed layer depth ($\sigma_t = 0.03$ kg m^{-3}) in the Labrador Sea (58-48°W, 55-65°N) for the first 50 models years of HR_{pp} and XR_{pp}.

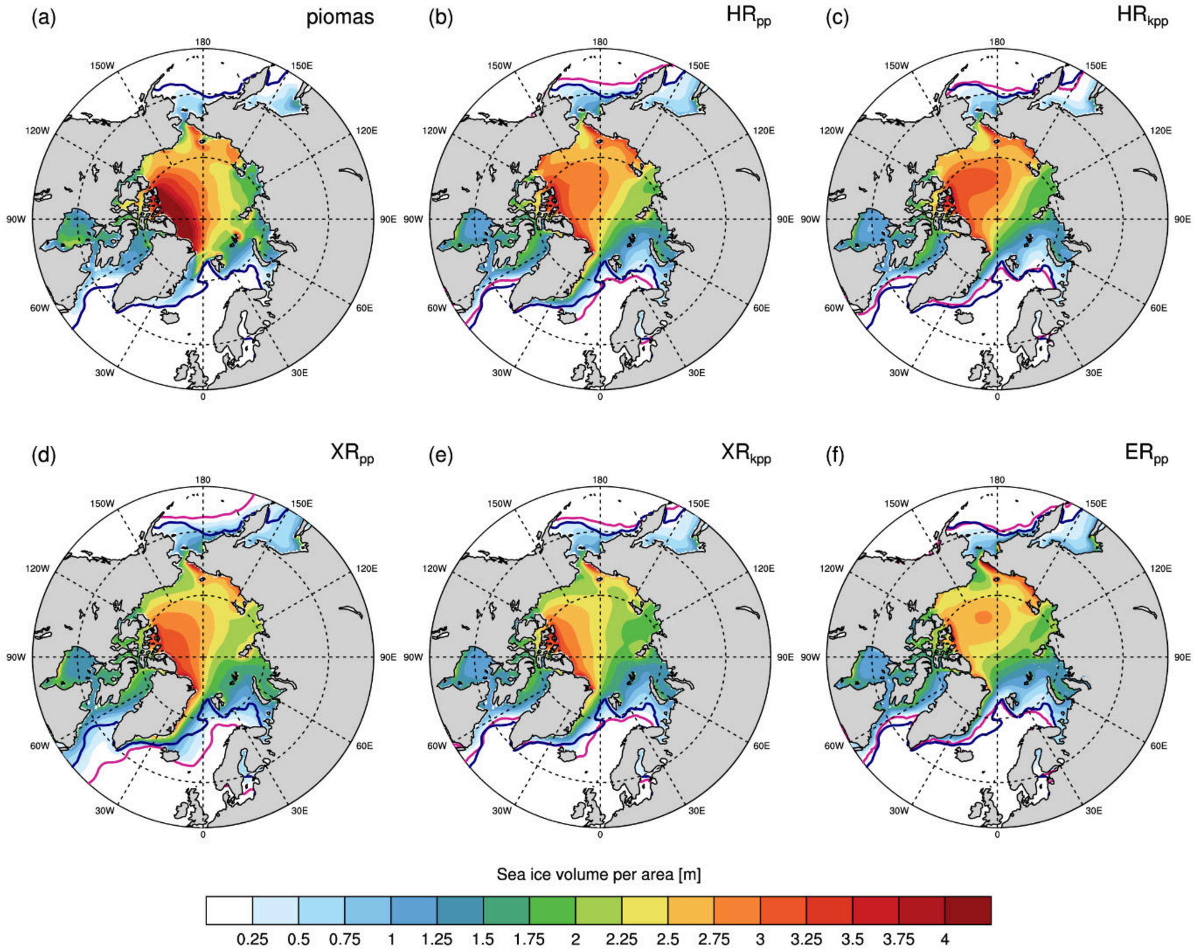

Fig. 2. Time-averaged Arctic sea ice volume in March. The 15% sea ice concentration contour line line is shown in magenta for the MPI-ESM1.2 simulations and in dark blue for the EUMETSAT OSI SAF observation.

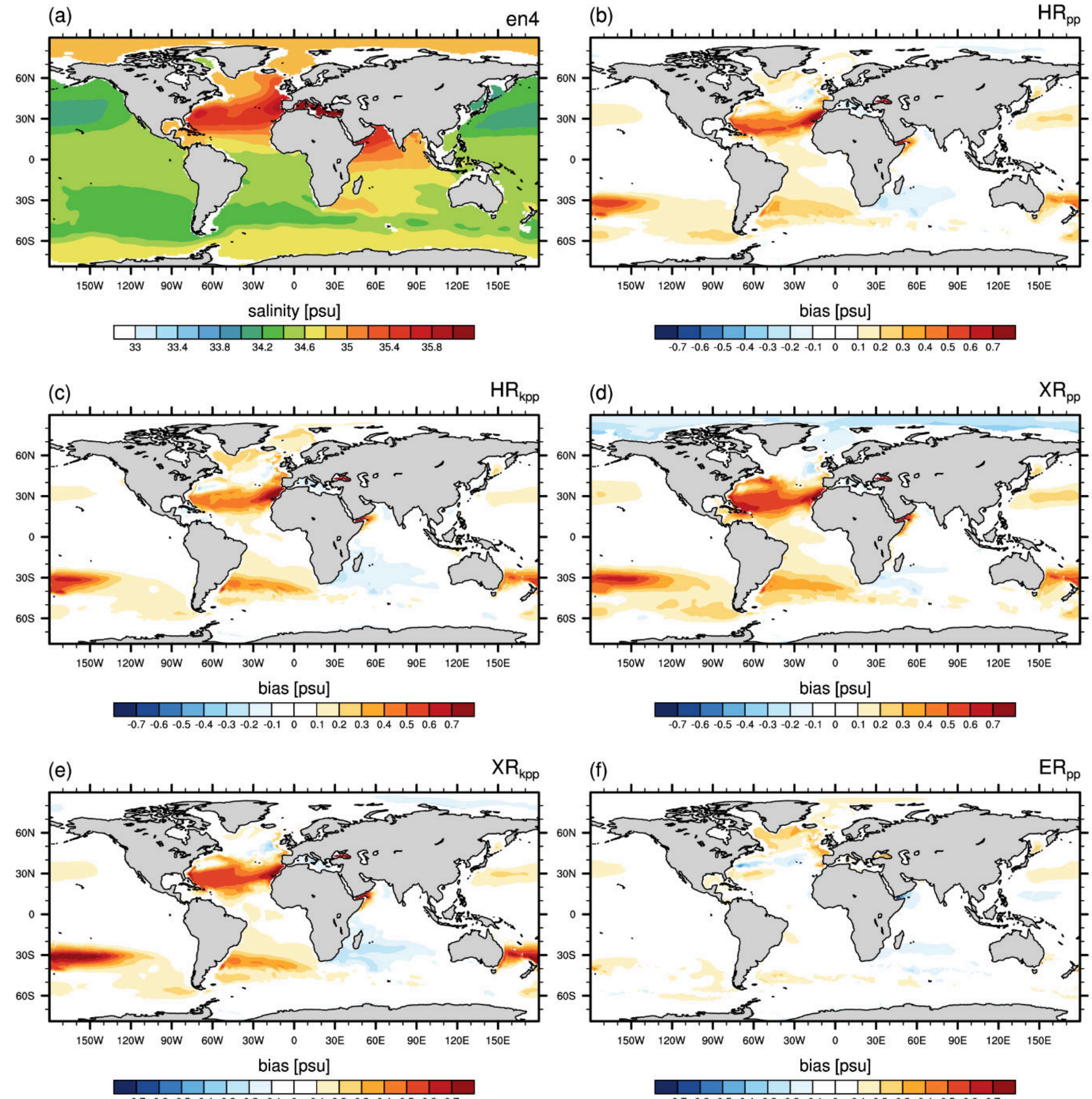

Fig. 3. Time-averaged bias of simulated potential temperature at 1085m depth (averaged over model years 30 to 80) with respect to EN4 (averaged over 1945-1955).

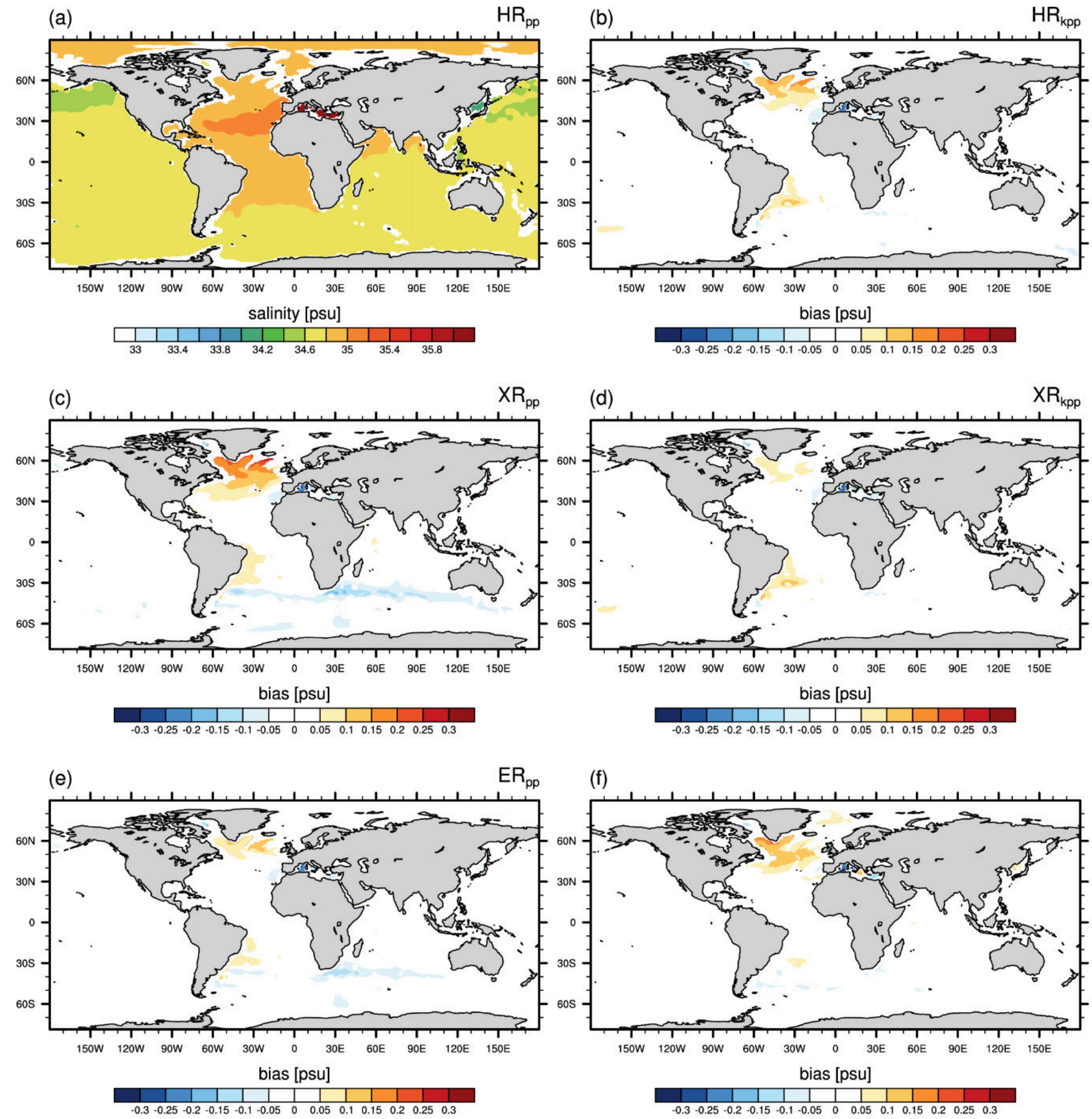

Fig. 4. same as Figure 3 but at 2080m depth.

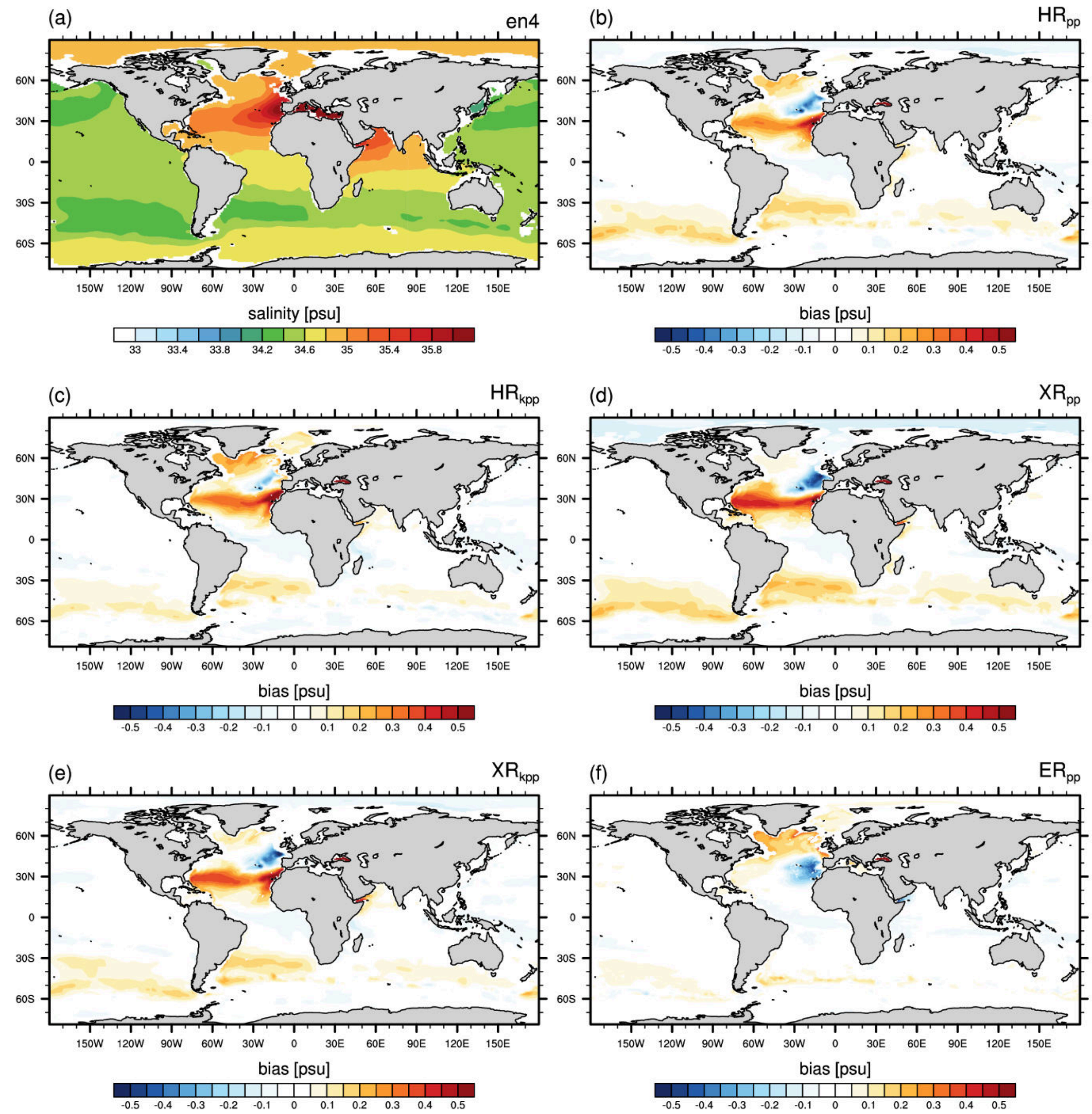

***Fig. 5**. Time-averaged bias of simulated salinity at 1085m depth (averaged over model years 30 to 80) with respect to EN4 (averaged over 1945-1955).*

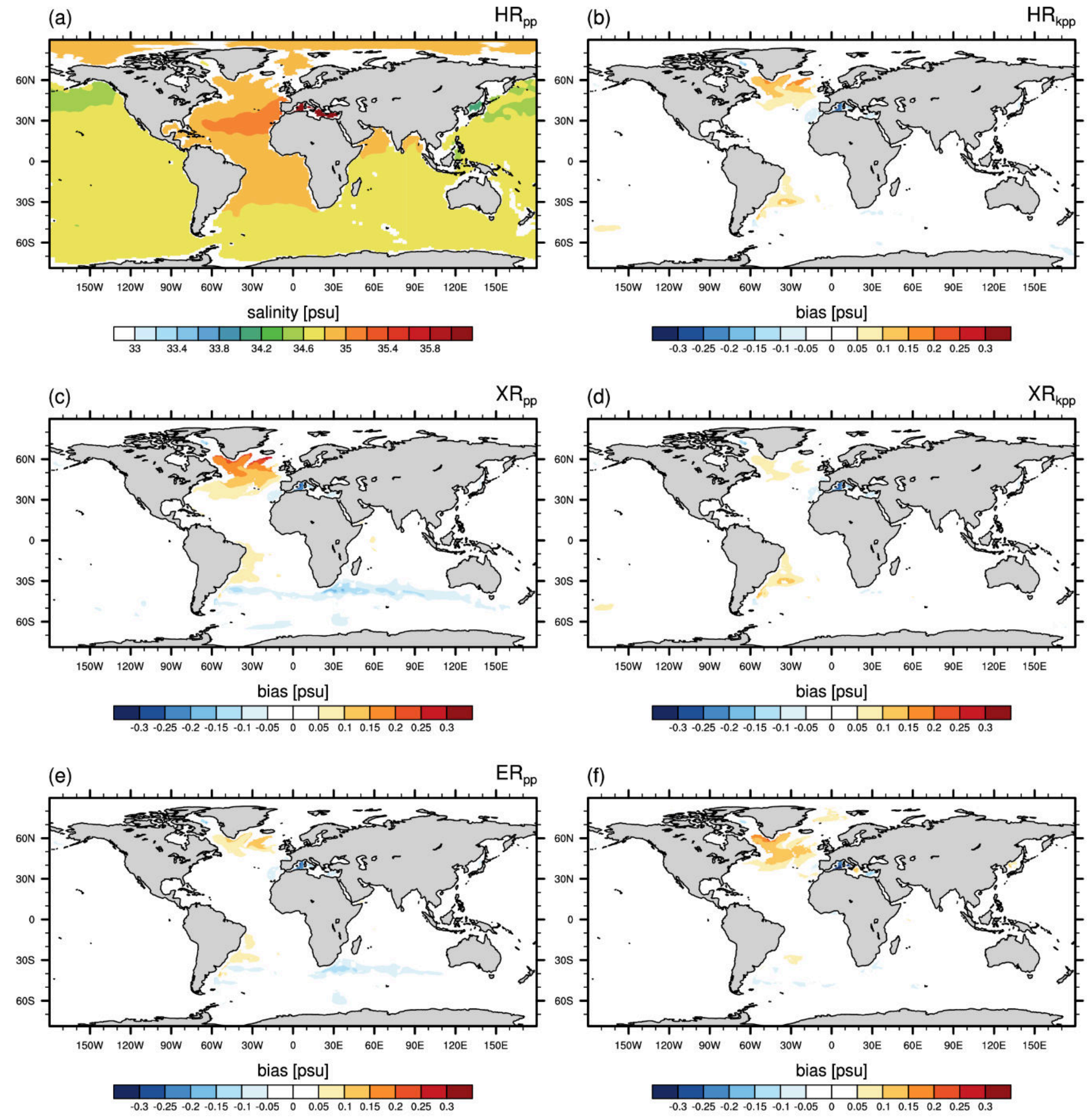

Fig.6. same as Figure 5 but at 2080m depth.

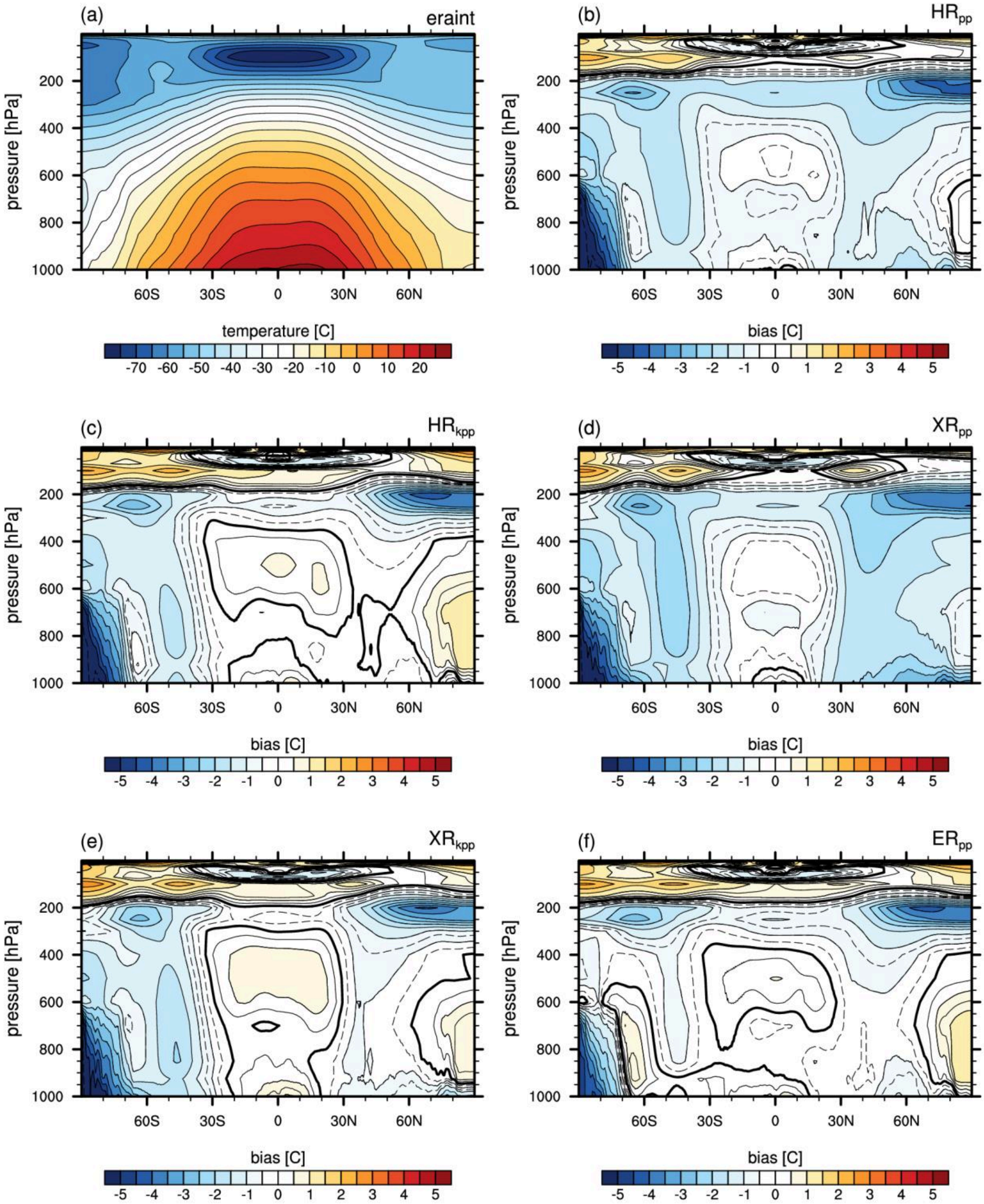

Fig. 7. Global zonally-averaged temperature. The contour lines in b-f span ±0.75 with an interval of 0.5K, and of 1.0K outside that range.

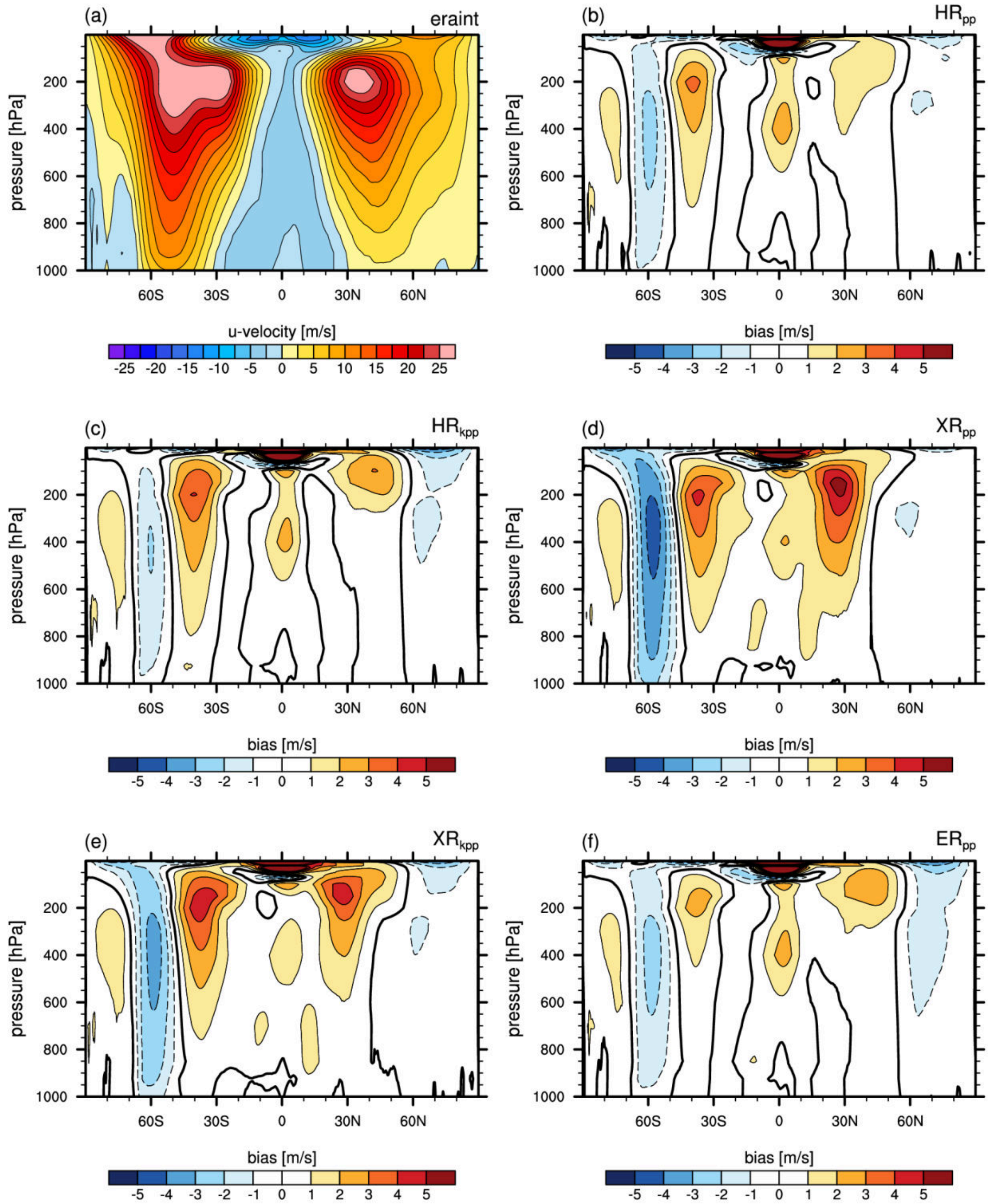

Fig.8. Global zonally-averaged u-velocity. The zero contour line is shown as a thick solid line; negative (positive) contours are dashed (solid).

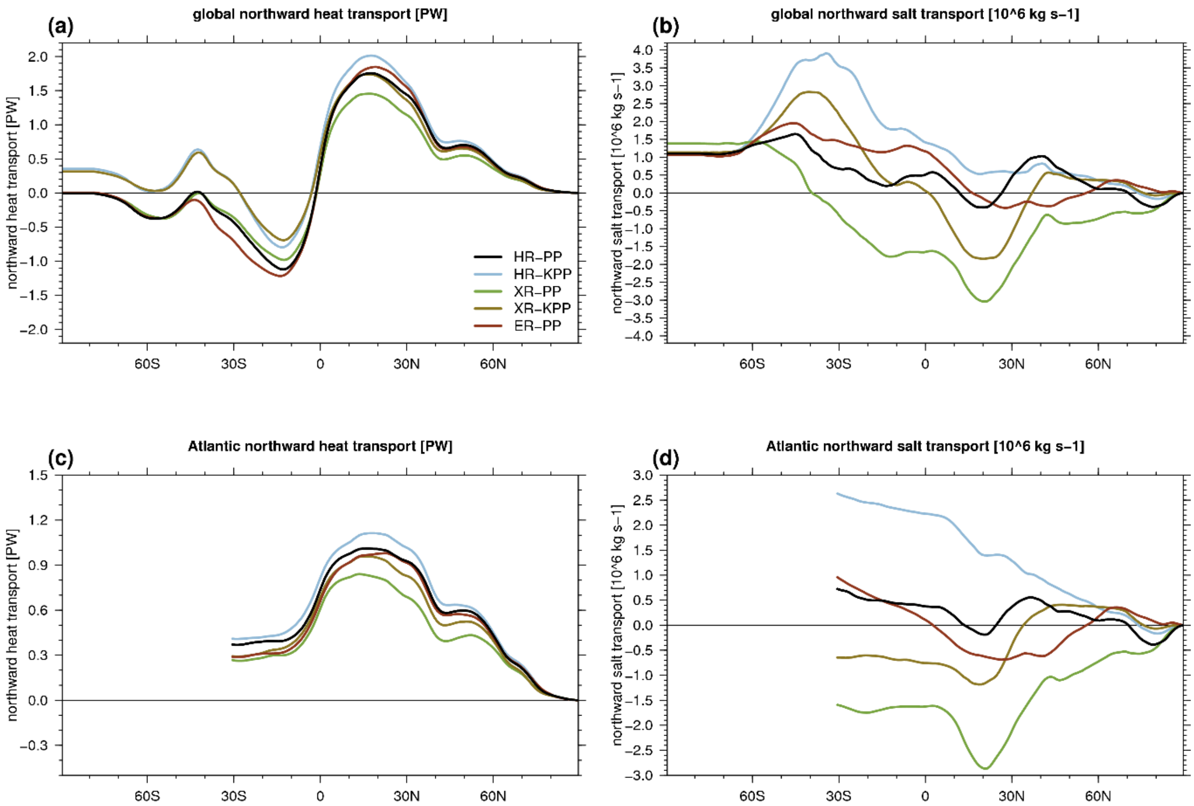

Fig. 9. Time-averaged northward heat (PW) and salt transport (106 kg s-1) in the global ocean (a,b) and in the Atlantic basin (c,d). Note the different scaling in (c) and (d).

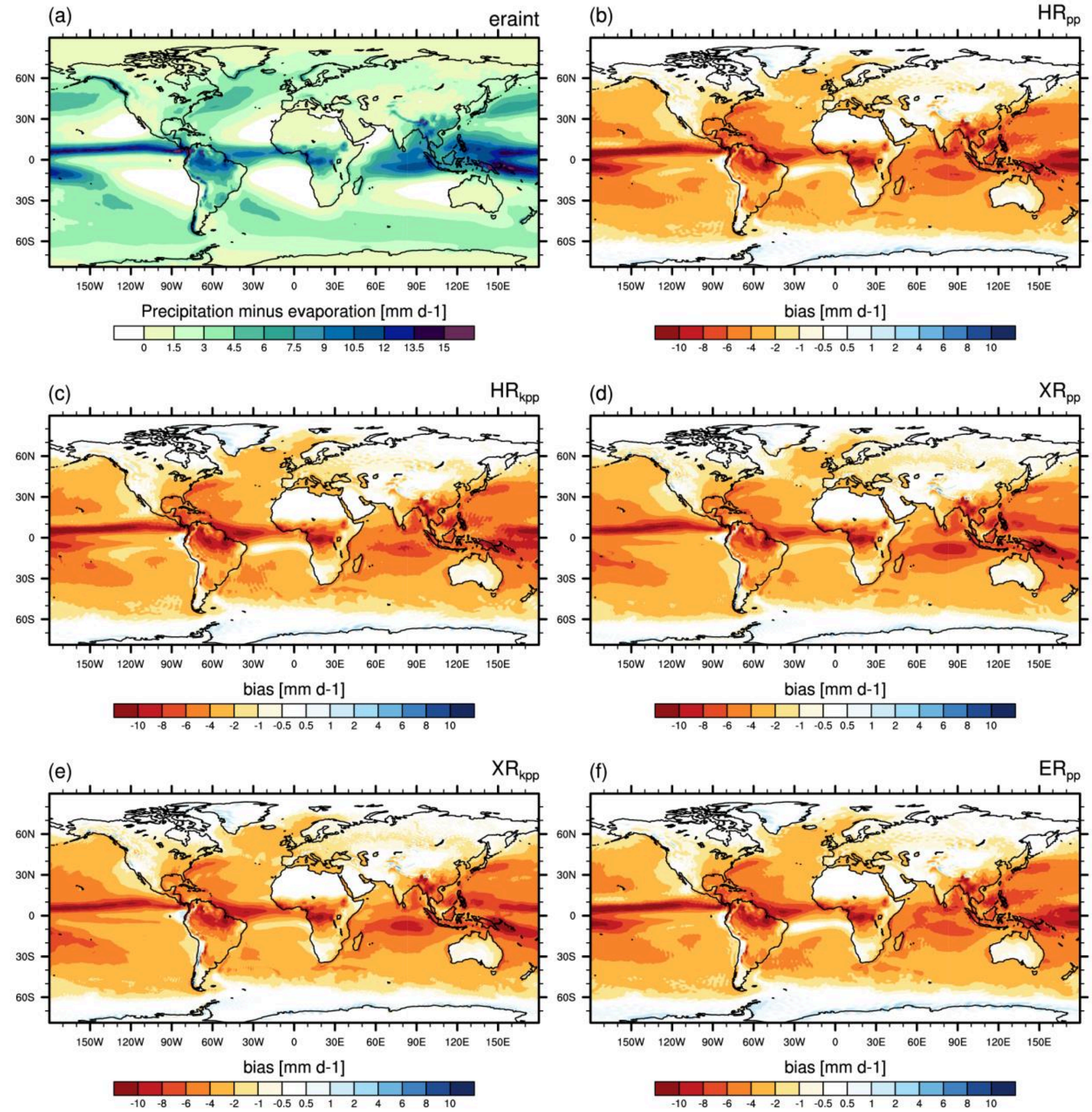

Fig. 10. Time-averaged precipitation minus evaporation from (a) ERA-Interim (1979-2005) and the bias (MPI-ESM1.2 minus ERA-Interim) of (b) HRpp, (c) HRkpp, (d) XRpp, (e) XRkpp, and (f) ERpp.

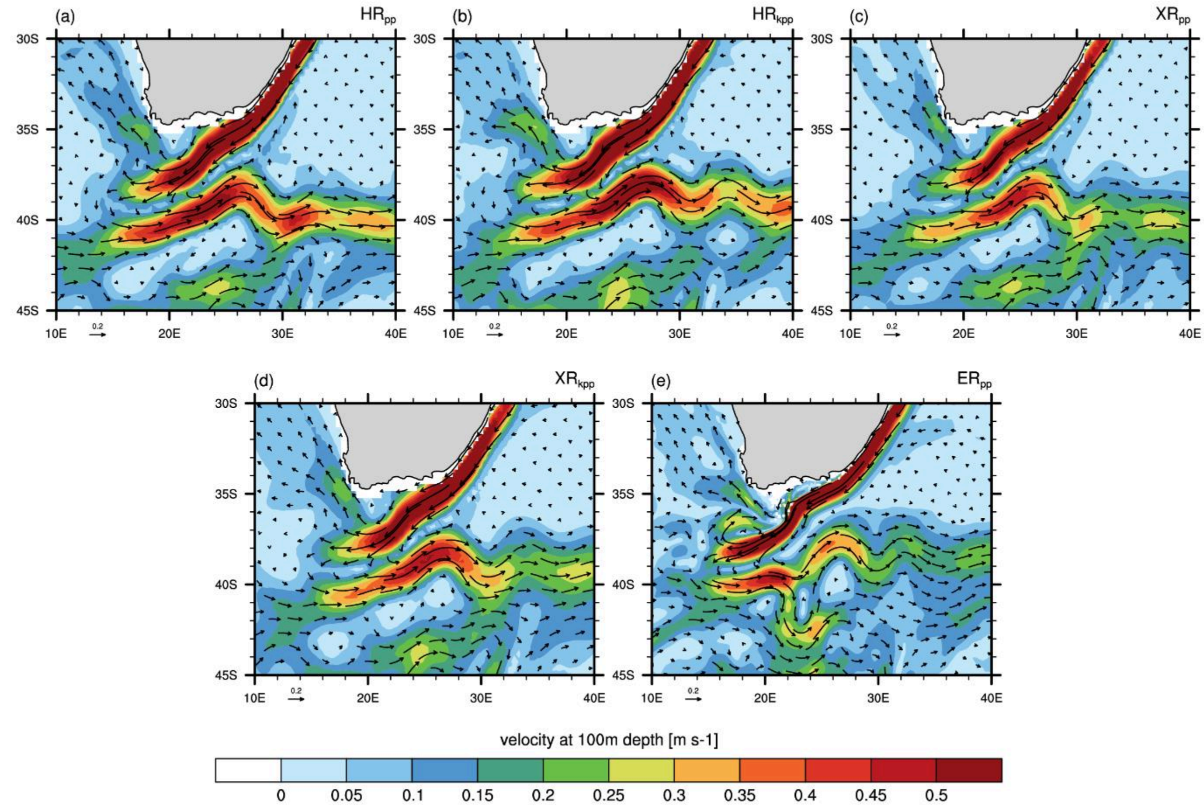

Fig. 11. Time-averaged velocity at 100m depth of the Agulhas Current system simulated by (a) HRpp, (b) HRpp, (c) HRkpp, (d) XRpp, (e) XRkpp, and (f) ERpp. The length of the reference vector is 0.2 m s^{-1}.

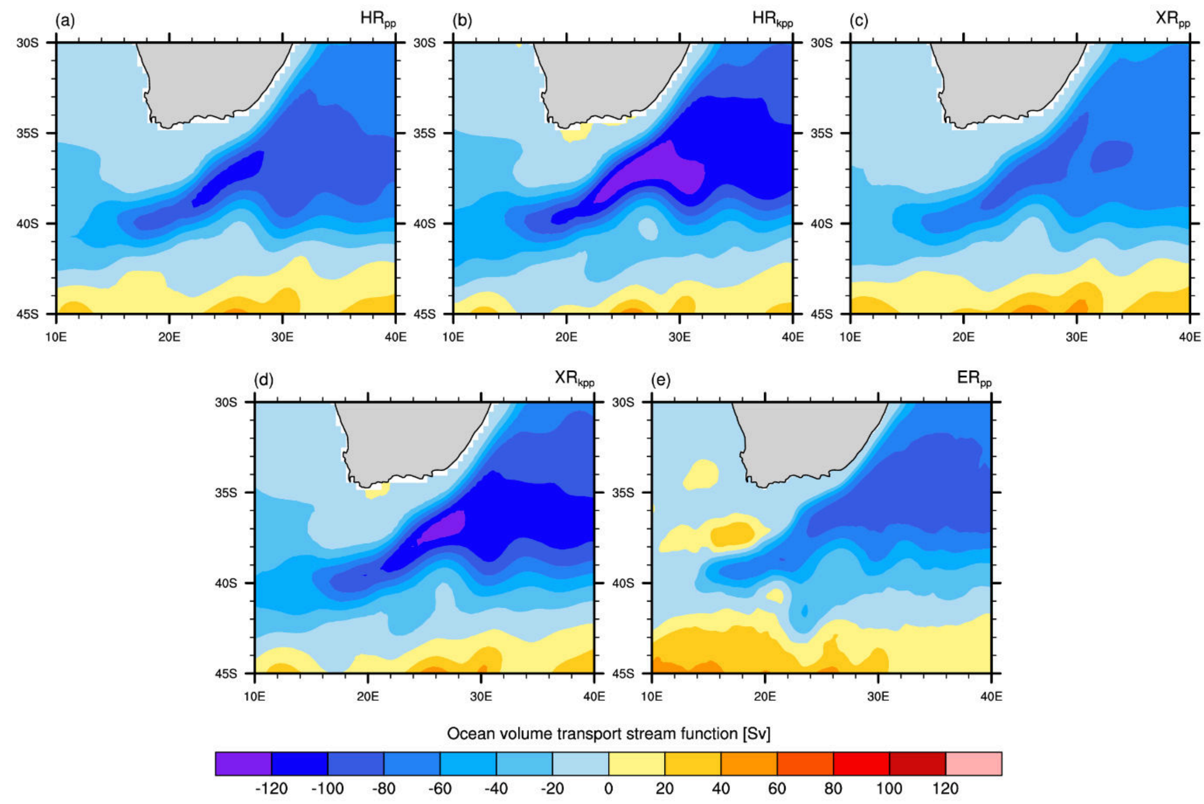

Fig. 11. Time-averaged barotropic volume transport (Sv) stream function of the Agulhas Current system simulated by (a) HRpp, (b) HRpp, (c) HRkpp, (d) XRpp, (e) XRkpp, and (f) ERpp.

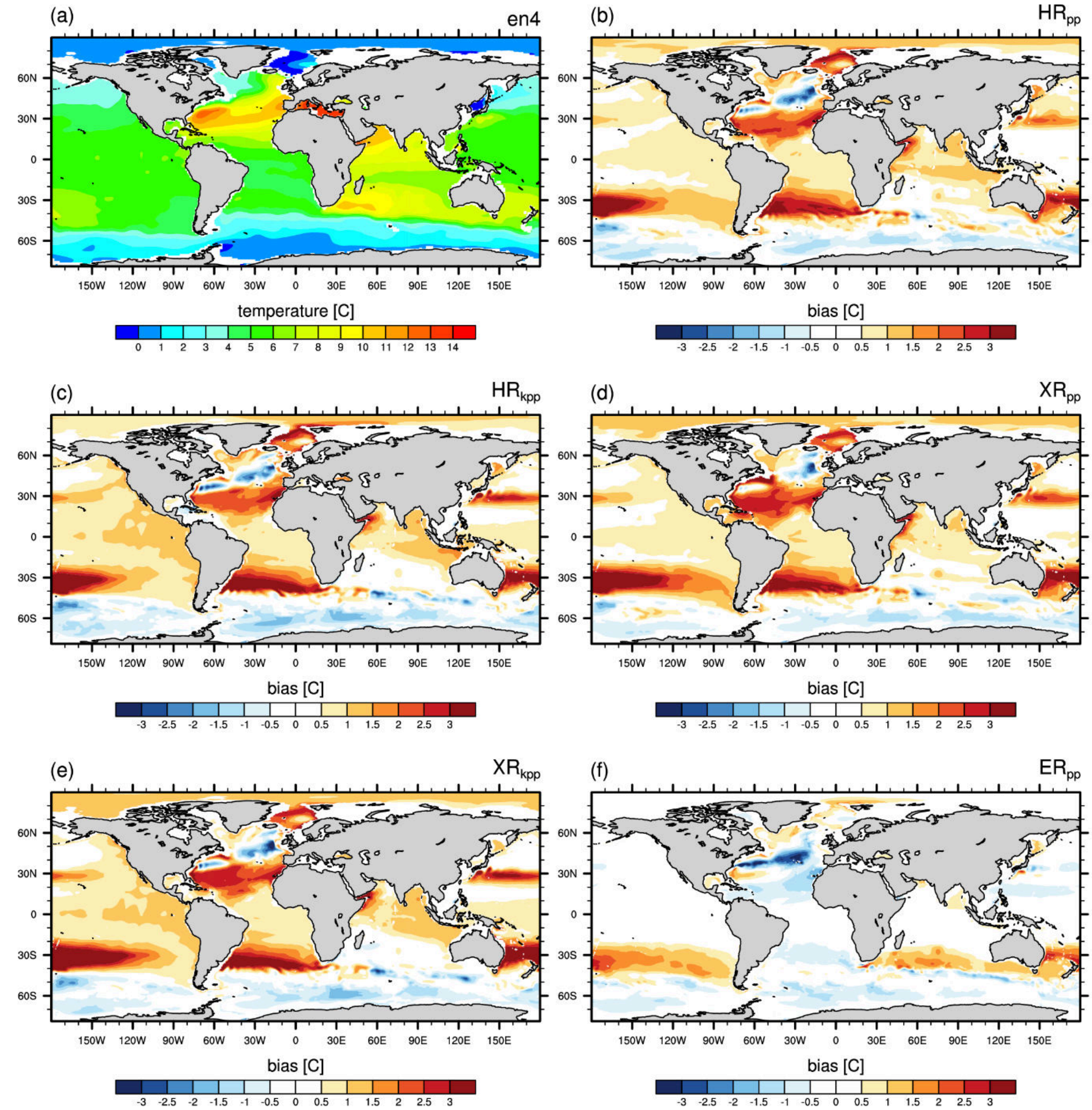

Fig. 13. Sea water potential temperature (°C) at 740m depth from (a) EN4 (averaged over 1945–1955) and differences: MPI-ESM1.2 minus EN4 for (b) HRpp, (c) HRkpp, (d) XRpp, (e) XRkpp, and (f) ERpp.

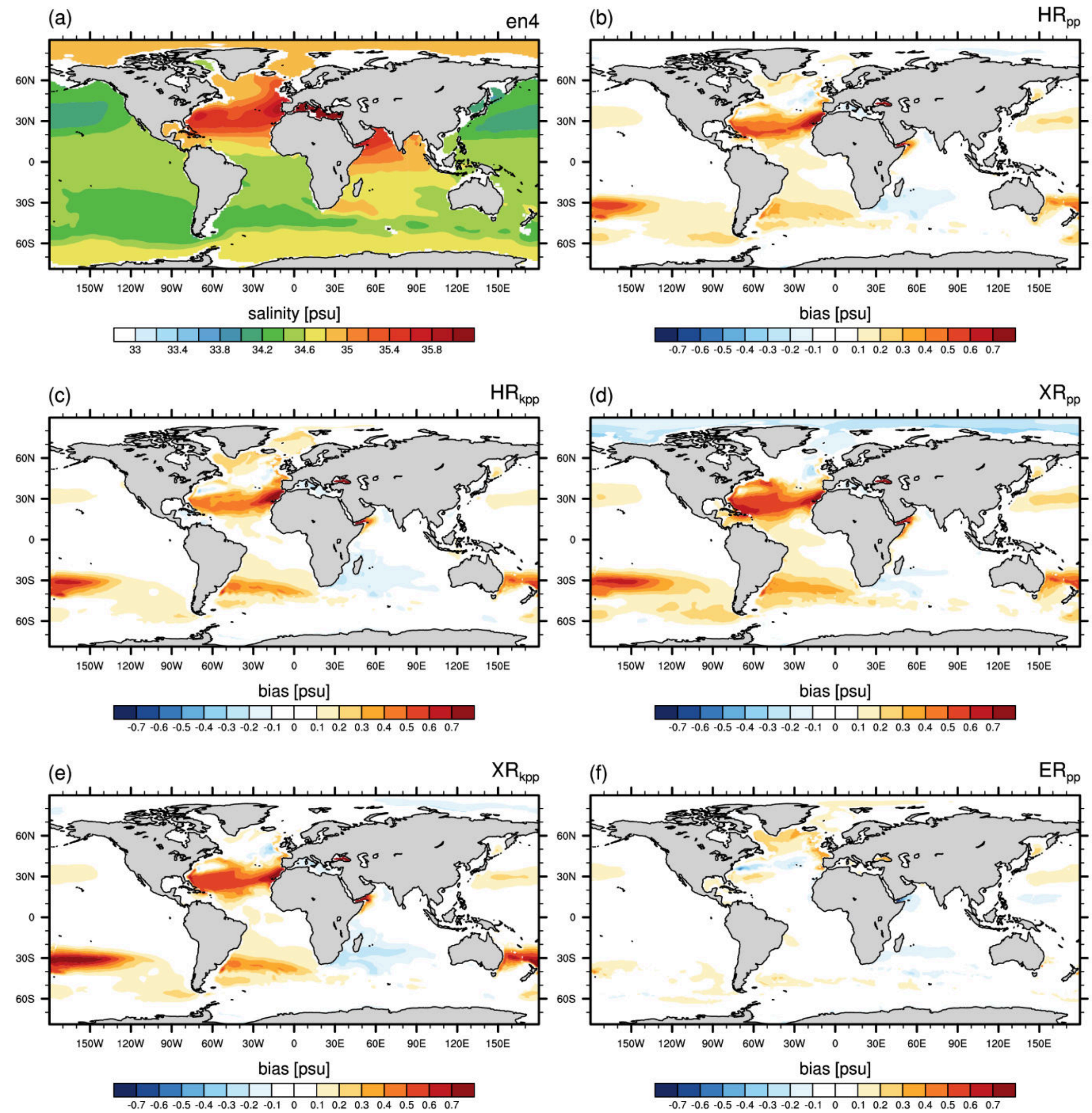

Fig. 14. Sea water salinity (psu) at 740m depth from (a) EN4 (averaged over 1945-1955) and Discussion paper differences: MPI-ESM1.2 minus EN4 for (b) HRpp,(c) HRkpp, (d) XRpp, (e) XRkpp, and (f) ERpp.

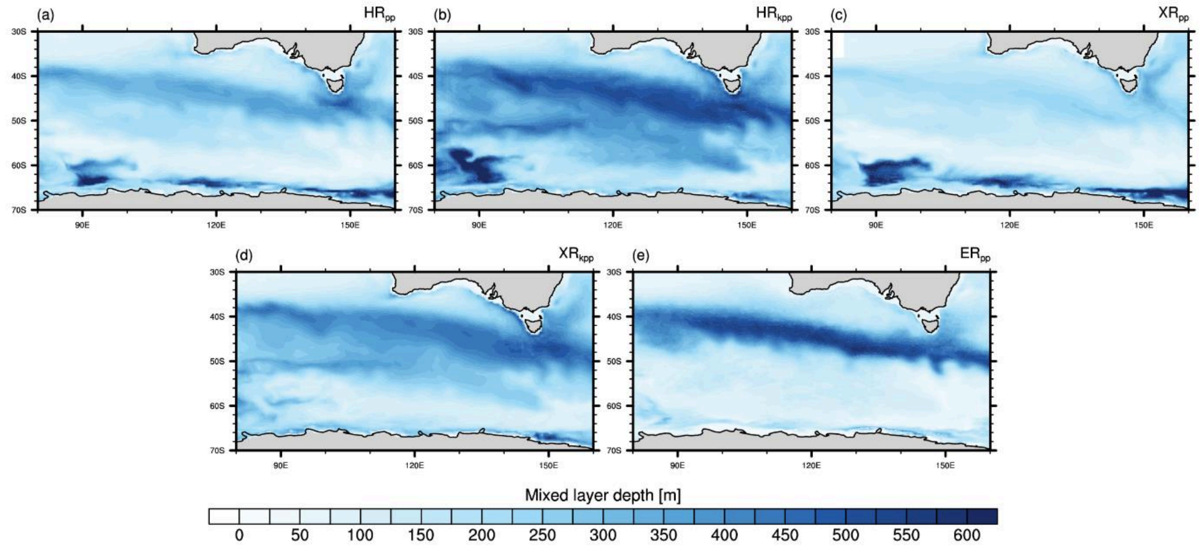

Fig. 15. Time-averaged mixed layer depths (σ_t=0.03 kg m^{-3}) across the Subantarctic Frontal zone in September simulated by (a) HRpp,(b) HRkpp, (c) XRpp, (d) XRkpp, and (e) ERpp.

Max Planck Institute Earth System Model (MPI-ESM1.2) for High-Resolution Model Intercomparison Project (HighResMIP)

Oliver Gutjahr[1], Dian Putrasahan[1], Katja Lohmann[1], Johann H. Jungclaus[1], Jin-Song von Storch[1], Nils Brüggemann[1,2], Helmuth Haak[1], and Achim Stössel[3]

[1]Max Planck Institute for Meteorology, Hamburg, Germany
[2]University of Hamburg, Hamburg, Germany
[3]Department of Oceanography, Texas A&M University, College Station, Texas, USA

Correspondence: O. Gutjahr (oliver.gutjahr@mpimet.mpg.de)

Abstract. As a contribution towards improving the climate mean [..[1]]state of the atmosphere and the ocean in Earth System Models (ESMs), we compare several coupled simulations conducted with the Max Planck Institute for Meteorology Earth System Model (MPI-ESM1.2) following the HighResMIP protocol. Our simulations allow to analyse the separate effects of increasing the horizontal resolution of the ocean ($0.4°$ to $0.1°$) and atmosphere (T127 to T255) submodels, and the effects of substituting the Pacanowski and Philander (PP) vertical ocean mixing scheme with the K-Profile Parameterization (KPP).

The results show clearly distinguishable effects from all three factors. The eddy-resolving ocean removes biases in the ocean interior and in the atmosphere. This leads to [..[2]]the important conclusion that [..[3]]an eddy-resolving ocean has a major impact on the [..[4]]mean state of the ocean and the atmosphere. The T255 atmosphere reduces the surface wind stress and improves ocean mixed layer depths in both hemisphere. The reduced wind forcing[..[5]], in turn, slows the Antarctic Circumpolar Current (ACC) [..[6]]reducing it to observed values. In the North Atlantic, however, [..[7]]the reduced surface wind causes a weakening of the subpolar gyre and thus a slowing down of the Atlantic Meridional Overturning Circulation (AMOC)[..[8]], when the PP scheme is used. The KPP scheme, on the other hand, causes stronger open-ocean convection [..[9]]which spins up the [..[10]]subpolar gyres, ultimately leading to a stronger and stable AMOC, even when coupled to the T255 atmosphere, [..[11]]thus retaining all the positive effects of a higher resolved atmosphere.

[1]removed: states
[2]removed: an
[3]removed: ocean eddies have
[4]removed: large-scale temperature distribution in the atmosphere, and on temperature and salinity distributions in the ocean. The near-surface wind forcing reduces with a
[5]removed: further
[6]removed: and reduces the transport through Drake Passage
[7]removed: it causes a slow
[8]removed: due to a slower subpolar gyre
[9]removed: that
[10]removed: gyres and leads
[11]removed: maintaining

Copyright statement. TEXT

1 Introduction

The evolving computational power allows for ever higher resolutions of earth system models (ESM). High resolution ESMs are able to explicitly resolve processes that are subgrid-scale and parameterized in low-resolution models. Optimally, [..[12]]better resolved processes [..[13]]would improve atmosphere and ocean dynamics and thus reduce biases in the mean state and in the variability of key quantities. In this manuscript[..[14]], we separately increase the horizontal resolution of the [..[15]]atmosphere and ocean submodels and analyse the effects on the mean [..[16]]states. Besides increasing the resolution of the major model subcomponents, new strategies and model developments, such as improved physics, are required for improving ESMs. Therefore, we also analyse the effects of a more sophisticated vertical mixing parameterization in the ocean submodel.

Specifically, this paper describes the adaptation of the Max Planck Institute - Earth System Model (MPI-ESM, Giorgetta et al., 2013) to higher horizontal resolutions and the implementation of improved ocean physics within the PRIMAVERA project (https://www.primavera-h2020.eu/). A key aspect of the project is on improving the simulation of the European climate, which is why we put a focus on the North Atlantic and the Atlantic Meridional Overturning circulation (AMOC). We investigate separately the effects of increasing [..[17]]horizontal resolution of the atmosphere and the ocean, and of exchanging the vertical mixing parameterization in the ocean and sea ice submodel MPIOM (Jungclaus et al., 2013).

All our simulations follow the High Resolution Model Intercomparison Project [..[18]](HighResMIP) protocol (Haarsma et al., 2016) and provide climate simulations with varying horizontal resolutions that are higher than the standard resolution of the Coupled Model Intercomparison Project - Phase 6 (CMIP6; Eyring et al., 2016). An overview of all performed simulations for this study is shown in Tab. 1.

Our reference model is the MPI-ESM1.2-HR (or HR in the remainder of the manuscript) that was recently described by Müller et al. (2018) and contributes to CMIP6. HR is the higher resolution version of the former MPI-ESM1.2-LR (or LR), with [..[19]]1.5 times as high (T127, $\sim 100\,\mathrm{km}$) horizontal resolution for the atmospheric submodel ECHAM6.3 (Hertwig et al., 2015; Mauritsen et al., 2018) and a $0.4\,°(\sim 40\,\mathrm{km})$ ocean on [..[20]]an eddy-permitting tripolar grid (TP04) (Jungclaus et al., 2013) compared to the LR version (T63, $\sim 200\,\mathrm{km}$ atmosphere and $1.5\,°$ ocean grid). How the ocean and atmosphere mean states improve in HR compared to LR [..[21]]was described by Müller et al. (2018). Further reductions of atmospheric

[12] removed: the
[13] removed: improve the
[14] removed: we analyse separately
[15] removed: effects of increasing the horizontal atmospheric and oceanic resolution
[16] removed: state. However, besides
[17] removed: the
[18] removed: (HighResMIP; Haarsma et al., 2016) protocol
[19] removed: a twice
[20] removed: a
[21] removed: were

biases were shown by Hertwig et al. (2015), who used ECHAM6.3 with a T255 ($\sim 50\,\mathrm{km}$) resolution in atmospheric model intercomparison project (AMIP) type experiments.

Building on these improvements, we further use a coupled MPI-ESM1.2 version with the T255 atmosphere and the TP04 ocean grid (MPI-ESM1.2-XR or simply XR) to investigate the effect of an increased atmospheric resolution on the mean state. This XR version was already used by [..[22]]Putrasahan et al. (2019) and (although under a different acronym) by Milinski et al. (2016). Milinski et al. (2016) demonstrated that the sea surface temperature bias in the upwelling regions along the coast of Africa diminished because of a more detailed representation of the coastal winds with the T255 atmosphere. Although biases were reduced with a T255 version of ECHAM6.3, our XR simulation generally produces too weak surface wind speeds, in particular [..[23]]over the North Atlantic and the subpolar gyre [..[24]](Putrasahan et al., 2019).

These weaker near-surface winds caused a slowdown of the Atlantic Meridional Overturning Circulation (AMOC) to about $9\,\mathrm{Sv}$ ($\mathrm{Sv} := 10^6\,\mathrm{m^3\,s^{-1}}$), as documented by [..[25]]Putrasahan et al. (2019). This issue was not only affecting the MPI-ESM1.2, but was also reported by other modelling centres using ECHAM6, although going from T63 to T127 (Sein et al., 2018). Sein et al. (2018) gave a possible explanation for the reduction of mean wind speeds, which they attribute to a higher cyclone activity with the T127 resolution, in particular over the North Atlantic.

The AMOC strength and its stability depend to a large [..[26]]extend on the vertical mixing parameterization (Gent, 2018). To investigate the sensitivity of the AMOC [..[27]]and the mean states, we conducted parallel experiments with HR and XR in which the [..[28]]modified parameterization of Pacanowski and Philander (1981) (PP[..[29]]), which is default in MPI-ESM1.2 (Marsland et al., 2003), was replaced by the more sophisticated K-Profile Parameterization (KPP) scheme of Large et al. (1994). It turned out that the KPP scheme compensates for the underestimated mean winds in the high latitudes and in the tropics in the XR simulation, sustaining a stable AMOC. The reasons for this will be elaborated upon.

Finally, we adopt the $0.1\,^{\circ}(\sim 11\,\mathrm{km})$ tripolar grid (TP6M) of MPIOM that was already used in an eddy-resolving ocean-only simulation forced by NCEP, and in a coupled run with T63 and T255 versions of ECHAM6 – the so-called STORM simulations (von Storch et al., 2012; Stössel et al., 2015, 2018). With this eddy-resolving coupled version (MPI-ESM1.2-ER or ER), we detect noticeable reductions of biases not only in the ocean and near-surface atmosphere, but also in the higher atmosphere. This leads to [..[30]]the important conclusion that [..[31]]an eddy-resolving ocean has a major impact on the large-scale temperature distribution in the atmosphere, consistent with recent findings (Frenger et al., 2013; Ma et al., 2016; Liu et al., 2018). The parallel simulations allow to separately analyse (1) the effects of [..[32]]increased atmospheric resolution

[22]removed: Putrasahan et al. (2018)
[23]removed: above
[24]removed: (Putrasahan et al., 2018)
[25]removed: Putrasahan et al. (2018)
[26]removed: extent
[27]removed: , but also of
[28]removed: traditional
[29]removed: scheme)
[30]removed: an
[31]removed: ocean eddies have
[32]removed: atmosphere and

(HR vs. XR), (2) the effects of increased ocean model resolution [..[33]](HR vs. ER), and (3) the effect of an alternative vertical ocean mixing parameterizations (PP vs. KPP) on the mean climate.

We begin by describing the model configuration and spin-up procedure in section 2. In section 3 we present the results of the atmospheric mean state, [..[34]]including a description of reduced wind stress in XR. In section 4 we show the results of the ocean mean state, including the consequences of the reduced wind stress and how the KPP scheme sustains the AMOC. In section 5 we summarize all results and contrast the effects from increased resolution to improved ocean mixing.

2 Model, spin-up, and experiments

2.1 Model description

The atmospheric submodel of [..[35]]MPI-ESM1.2 is ECHAM6.3 (Mauritsen et al., 2018)[..[36]], which includes the land-surface scheme JSBACH (Stevens et al., 2013; Reick et al., 2013). The ocean and sea ice submodels are combined in MPIOM (Jungclaus et al., 2013; Notz et al., 2013). ECHAM6.3 and MPIOM are coupled via the Ocean-Atmosphere-Sea-Ice coupler version 3 (OASIS3-mct; Valcke, 2013) with a coupling frequency of 1 h. ECHAM6.3 was used with 95 vertical levels at two different spectral resolutions, truncated at T127 (~103 km) in HR and ER and T255 (~51 km) in XR. We did not change any parameter going from HR to XR, except for a reduction of the time step from 200 s (HR) to 90 s (XR) [..[37]]and the horizontal diffusion damping term. Both use the same eddy-permitting ocean with a resolution of 0.4°(~44 km) [..[38]]on a tripolar grid (TP04, Jungclaus et al., 2013) with 40 unevenly spaced vertical levels. The first 20 levels are distributed in the top 750 m. A partial grid cell formulation (Adcroft et al., 1997; Wolff et al., 1997) is used for a more accurate representation of the bottom topography. River runoff is calculated by a horizontal discharge model (Hagemann and Gates, 2003).

In the ER configuration, the ocean component has a nominal resolution of 0.1 ° (~11 km) on a tripolar grid (TP6M) (e.g. von Storch et al., 2012)[..[39]]. The TP grid has quasi-uniform resolution in the [..[40]]Northern hemisphere, but scales with latitute in the Southern hemisphere. We did not change any parameters compared to the TP04 grid as prescribed by the HighResMIP protocol (Haarsma et al., 2016), except that we reduced the time step from 3600 s (TP04) to [..[41]]240 s (TP6M). Table 1 provides an overview of the simulations that we compared in this study. The HR configuration of our reference simulation is exactly the same as in Müller et al. (2018). The XR configuration was used by Hertwig et al. (2015) (denoted as VHR in their study) for AMIP simulations with ECHAM6 and in Milinski et al. (2016) (denoted as HRatm in their study) for

[33] removed: , as well as
[34] removed: and in
[35] removed: MPI-ESM version 1.2
[36] removed: and it
[37] removed: ,
[38] removed: and
[39] removed: , with higher
[40] removed: vicinity of the poles
[41] removed: 300

MPI-ESM runs. The [..[42]]TP6M configuration was already used in stand-alone ocean simulations with 80 vertical levels (von Storch et al., 2012; Stössel et al., 2018), and in fully coupled simulations (e.g. Stössel et al., 2015).

All simulations (except ER) use the thickness diffusivity κ_{GM} of the Gent et al. (1995) (GM) parameterization to account for the diffusion and tracer advection induced by unresolved mesoscale eddies in the ocean. For the TP04 grid, κ_{GM} is constant and chosen to be proportional to the grid spacing. A value of $\kappa_{GM} = 250\,\mathrm{m^2\,s^{-1}}$ is chosen for a 400 km wide grid cell and it reduces linearly with increasing resolution. That is, for the eddy-permitting TP04 grid κ_{GM} is only about 10 % of this value. The lateral eddy diffusivity is parameterized by an isopycnal formulation (Redi, 1982) and is set to $\kappa_{Redi} = 1000\,\mathrm{m^2\,s^{-1}}$ for a 400 km wide grid cell, again reducing linearly with increasing resolution. In ER, κ_{GM} is set to zero, [..[43]]but κ_{Redi} is unchanged (von Storch et al., 2016).

An innovation over previous versions of HR and XR is that we used two different diapycnal mixing schemes (see section 2.2[..[44]]): the PP scheme as default, and the KPP scheme. The [..[45]]diapycnal mixing scheme used in a simulation is indicated by subscripts: $\mathrm{HR_{pp}}$, $\mathrm{HR_{kpp}}$, $\mathrm{XR_{pp}}$, $\mathrm{XR_{kpp}}$, and $\mathrm{ER_{pp}}$. Note that the model was not retuned when the KPP scheme was used, to account for the pure effect of a changed ocean mixed layer scheme. For all our comparisons, $\mathrm{HR_{pp}}$ is our reference simulation.

We follow the HighResMIP protocol (Haarsma et al., 2016) for initialising and forcing our coupled control simulations. The coupled runs used fixed 1950 forcing that consists of greenhouse gases, including ozone and aerosol loadings of the 1950s climatology ($\sim$ 10 year mean). The HR simulations were initialised from an HR control simulation that was nudged to the averaged state of 1950 to 1954 of the UK MetOffice Hadley Centre EN4 observational data set (version 4.2.0; Good et al. (2013)). The XR runs were initialised from the same ocean state, but from an atmospheric state that has been spun up for 10 years from a dry state. ER was initialised from the HR atmospheric state and directly from EN4 (averaged state from 1950-54) for the ocean. We integrated the HR and XR control simulations for 150 years and the ER simulation for 80 years (see Tab 1). We cut off the first 30 years as spin-up and used the following 50 years from the control runs for the analysis.

2.2 Diapycnal mixing

Previous MPI-ESM versions used a modified version of the Richardson-number dependent formulation of Pacanowski and Philander (1981) (PP scheme). The modification of the original PP formulation consists of a parameterization for [..[46]]wind-induced mixing that decays exponentially with depth (Marsland et al., 2003). Convection is parameterized by enhanced eddy diffusivity ($k_v = 0.1\,\mathrm{m^2\,s^{-1}}$). For our simulations[..[47]], we corrected a bug associated with the vertical viscosities, which were only about 50 % of the correct solution from the PP scheme. This error was then also corrected in the HR version described by Müller et al. (2018). The background value for the vertical diffusivity is constant and was set to $1.05 \cdot 10^{-5}\,\mathrm{m^2\,s^{-1}}$ and to

[42] removed: ER
[43] removed: while
[44] removed: for details
[45] removed: used
[46] removed: wind induced
[47] removed: here

$5 \cdot 10^{-5}\,\mathrm{m^2\,s^{-1}}$ for the viscosity. The background values represent the breaking of internal waves, which provide the mechanical energy for diapycnal mixing in the interior of the ocean. The PP scheme is the default option in MPI-ESM1.2 and is thus used in our reference simulation ($\mathrm{HR_{pp}}$).

To improve the diapycnal mixing in MPIOM, we implemented the non-local '[..[48]]K-Profile parameterization' (KPP, Large et al., 1994). The KPP scheme was implemented by adding the Community Vertical Mixing (CVMix) project library (Griffies et al., 2013) to MPIOM. In the KPP scheme, the turbulent [..[49]]transports do not only depend on local gradients of the properties, but also on the overall state of the boundary layer, that is the surface fluxes and the boundary layer depth (Large et al., 1994). The non-local turbulent transport represents how surface properties are redistributed from the surface layer into the boundary layer, for example by buoyant plumes, Langmuir cells, or mesoscale cellular convective elements.

The non-local fluxes are non-zero only for tracers in unstable forcing conditions, i.e. for negative surface buoyancy fluxes. They then directly depend on the net heat and freshwater fluxes crossing the ocean surface multiplied by the local vertical diffusivities, a vertical shape function, and some constants (Griffies et al., 2013). For this non-local fluxes, the same vertical diffusivities are assumed as for the local tracer diffusion. In contrast to the PP scheme, these diffusivities are not limited to a user specified value, but depend on a depth-dependent turbulent vertical velocity scale, on a vertical shape function, and on the mixed layer depth (Griffies et al., 2013).

Below the mixed layer, we use the PP scheme with the same constant background diffusivity and viscosity. The diffusivities are not matched at the base of the mixed layer to avoid potential overshooting of the non-local transport terms, which might produce extrema in the tracer field (Griffies et al., 2013). Under sea ice, we reduce the [..[50]]wind-induced mixing in the PP and in the KPP scheme, so that the surface friction velocity u_* decreases quadratically with increasing sea ice concentration. For simplicity, we neglect that the momentum flux from the atmosphere into the ocean could be even stronger when sea ice is present, because of additional momentum flux at the interface of sea ice and the underlying sea water.

3 Evaluation of the atmospheric mean state

For the evaluation, the MPI-ESM1.2 simulations were averaged over the first 50 model years after the spin-up. We used the ERA-Interim reanalysis data (Dee et al., 2011) averaged from 1979–2005 as reference for the atmospheric mean state, as HR was tuned to this period (Mauritsen et al., 2012).

3.1 Surface quantities

3.1.1 10 m wind speed

The time-mean of the simulated 10 m scalar wind speed agrees well with ERA-Interim for large parts of the world's oceans and over the continents (Fig. 1). Consistently too low wind speeds, however, evolve over the northern parts of America and Europe,

[48]removed: K profile

[49]removed: transport

[50]removed: wind induced

over South America, and over Greenland and Antarctica. Too strong winds are simulated by all [..[51]]model confidurations over the subtropical oceans north and south of the equator. Models with the T127 atmosphere further simulate too strong winds speeds over the Weddell Sea (Fig. 1b,c,f).

[..[52]]Overall, the KPP scheme has only a minor effect on the 10 m wind speed[..[53]]. At the equatorial Pacific, KPP reverses the negative bias to a positive wind speed bias. Further, the negative bias in the Denmark and Fram Strait is reduced because of lower sea ice concentration in this area (see section 4.4).

Increasing the horizontal resolution from T127 to T255 in XR_{pp} (Fig. 1d) introduces a negative wind speed bias over the Antarctic Circumpolar Current (ACC) because of a reduced meridional pressure gradient. The near-surface wind speeds are further too low over the subpolar gyre in the North Atlantic, and over the Nordic Seas. This reduced wind [..[54]]stress over the subpolar gyre causes a slowdown of the AMOC in XR_{pp}, as described in detail by [..[55]]Putrasahan et al. (2019).

By using the KPP scheme in the XR model (XR_{kpp}; Fig. 1e), the wind speed reduces in the same areas as mentioned above, but not as strong as in XR_{pp}. [..[56]]However, the wind speed is still lower over the Nordic Seas and in the Pacific sector of the ACC. [..[57]]

Increasing the horizontal resolution of MPIOM from $0.4°$ to $0.1°$ (ER_{pp}; Fig. 1f) reduces the positive bias over the Indian Ocean, over the Greenland Sea, and over the subtropical Atlantic. Despite these improvements, an eddy-resolving ocean does have only a minor effect on the near-surface wind speed, when coupled to a rather coarse T127 atmospheric resolution.

3.1.2 2 m temperature

In contrast to the near-surface wind speed, the 2 m temperature distribution (Fig. 2) is [..[58]]strongly affected by changing the horizontal resolution of the submodels or by replacing the vertical ocean mixing parameterization. [..[59]]Over the ocean, it closely resembles the bias of the sea surface temperature (section 4.1.1). Again, all models (except XR_{pp}) agree well with ERA-Interim over the continents and over large parts of the world's oceans, in particular over the tropical and subtropical oceans and in the Arctic Ocean.

An area with larger discrepancies across all models is the North Atlantic. Here, all simulations show a cold bias, which is a common error in state-of-the-art ESMs [..[60]](Randall et al., 2007) that is mostly caused by a too zonal North Atlantic Current (NAC) [..[61]](Dengg et al., 1996), or by insufficient northward heat transport by the AMOC (Wang et al., 2014a). Drews

[51] removed: models

[52] removed: Although

[53] removed: , in some areas KPP reduces the biases. For example, HR_{kpp} (Fig. 1c) reduces the positive bias in the subtropical Atlantic and North Pacific

[54] removed: forcing

[55] removed: Putrasahan et al. (2018) and briefly outlined in section 4

[56] removed: This indicates that KPP can sustain a sufficient mixing to prevent a decline of the AMOC albeit a weaker wind forcing (as discussed later).

[57] removed: This reduced wind forcing of the ACC decreases the transport through the Drake passage as discussed later. Other regions are much less unaffected.

[58] removed: stronger

[59] removed: It

[60] removed: (Dengg et al., 1996), which is

[61] removed: (see section 4.1.1)

et al. (2015) demonstrated that correcting the flow field for biases removed the cold bias in the North Atlantic. Another area of cold near-surface air temperature biases is [..[62]]the region around the Antarctic peninsula. In contrast, all models (except XR_{pp}) simulate a consistent warm bias over the Canadian Archipelago, central Africa and central Asia. Although [..[63]]reduced in their magnitudes, all these biases remain in the higher resolution models or when KPP is used.

Our models with the T127 atmosphere (Fig. 2b,c,f) simulate [..[64]]a warm bias over the Weddell Sea, which is caused by too frequent open polynyas (see section 4.5). This warm bias vanishes [..[65]]or partly changes its sign in the western Weddell Sea, when increasing the atmospheric resolution to T255 in the XR models (Fig. 2d,e). This is because the frequency of open-ocean polynyas reduces (see section 4.5), so that the Weddell Sea is more often covered with thicker ice (not shown), causing colder near-surface temperatures. However, a severe cold bias develops over the North Atlantic and the Nordic Seas in XR_{pp}, as mentioned before. As a consequence, the temperatures over Europe decrease as well.

Using the KPP scheme in HR (Fig. 2c) results in warmer 2 m temperatures in the northern hemisphere, so that cold biases reduce, but warm biases become stronger. The reason is a stronger northward heat transport into the North Atlantic (see section 4) and thus a stronger heat release to the atmosphere. In XR_{kpp} (Fig. 2e), the warming caused by the KPP scheme and the cooling caused by the T255 atmosphere compensate, so that the bias pattern in the northern hemisphere is comparable to that of HR_{pp}. The cold bias along the ACC, however, is not affected by KPP and is similar to XR_{pp}.

[..[66]]Compared to $HR_{[..^{67}]pp}$, [..[68]]most of the cold biases vanish in ER_{pp}; in the region of the ACC, this is partly due to resolved eddies. The warm bias in the Weddell Sea, however, is [..[69]]considerably enhanced in the Atlantic sector of the Southern Ocean, because of more frequent open-ocean polynyas in ER_{pp}.

3.2 Vertical structure of zonal wind speed and temperature

3.2.1 Zonal wind speed

Fig. 3 shows the ERA-Interim climatology of the [..[70]]time-averaged zonal-mean wind speed (u-velocity) and the model biases. Overall, the vertical structure of the zonal wind speed is well represented in MPI-ESM1.2. A consistent bias [..[71]]in all simulations are too strong subtropical jets (centred at $\sim 200\,\mathrm{hPa}$). These [..[72]]too strong jets contribute further to higher zonal wind speeds extending into the upper troposphere at 40 to $45\,°\mathrm{S}$ and 40 to $45\,°\mathrm{N}$, as also found by Müller et al. (2018). [..[73]]Furthermore too strong zonal wind speeds are simulated in troposphere in the tropics at roughly $400\,\mathrm{hPa}$.

[62] removed: Antarctica and its peninsula. All
[63] removed: reducing in its
[64] removed: further
[65] removed: , partly changing
[66] removed: Although ER_{pp} (Fig. 2f) produces a similar bias pattern as HR
[68] removed: because of the same T127 atmosphere, it clearly reduces the cold bias over the ACC in the Southern Ocean due to partly
[69] removed: slightly
[70] removed: time-mean
[71] removed: of
[72] removed: enhanced
[73] removed: Another positive bias is simulated in the middle of the tropical troposphere (at $\sim 400\,\mathrm{hPa}$)

All models simulate [..[74]]consistently too low zonal wind speeds over the Southern Ocean at $\sim 60\,^{\circ}\mathrm{S}$ [..[75]]throughout the whole troposphere. [..[76]]The overall bias pattern in $\mathrm{HR_{kpp}}$ (Fig. 3c) [..[77]]is very similar to to $\mathrm{HR_{pp}}$ (Fig. 3b), although the bias in the over the Southern Ocean reduces and increases in the upper troposphere. The T255 atmosphere in the XR models amplifies all biases (Fig. 3d-e). That is, the subtropical jets become stronger and shift equatorwards and the zonal wind speed over the Southern Ocean reduces further.

Important for the ocean is the extension of the negative bias over the Southern Ocean down to the surface [..[78]]in both XR simulations (stronger in $\mathrm{XR_{pp}}$ than in $\mathrm{XR_{kpp}}$), which [..[79]]reduces the zonal wind stress driving the ACC and the upwelling of Circumpolar Deep Water (CDW). However, this wind bias in XR was found not to be the cause of the AMOC collapse (Putrasahan et al., 2019). Note that the near-surface negative bias for the North Atlantic cannot be seen here, as discussed above, because it cancels in the zonal mean. [..[80]]

The bias pattern in $\mathrm{ER_{pp}}$ (Fig. 3f) is similar to $\mathrm{HR_{pp}}$ and $\mathrm{HR_{kpp}}$, which indicates that the ocean resolution does not have a large impact on the mean zonal wind speed[..[81]]. However, both the positive bias in the subtropical jet in the northern hemisphere and the negative bias north of $60\,^{\circ}\mathrm{N}$ are slightly amplified.

3.2.2 Zonal temperature

The [..[82]]cross-sections of the global time-mean zonal-mean temperature (Fig. 4) show cold biases in the upper troposphere (at $\sim 250\,\mathrm{hPa}$) in both hemispheres. In the HR/XR simulations with PP (Fig. 4b,d), the cold bias extends to the surface in both hemispheres (Fig. 4b,d)[..[83]]. In $\mathrm{HR_{kpp}}$, however, this bias disappeared (Fig. 4c[..[84]]), and emerges only weakly in $\mathrm{XR_{kpp}}$ (Fig. 4e).

In $\mathrm{XR_{pp}}$ the surface-extending cold bias becomes larger in the lower troposphere compared to $\mathrm{HR_{pp}}$, because of the [..[85]]weaker AMOC and the freezing of the Labrador and Nordic Seas (see section 4 below). In contrast, the AMOC remains stable in $\mathrm{XR_{kpp}}$ (Fig. 4e), so that no severe cold bias evolves in the lower troposphere of the northern hemisphere. However, the KPP scheme does not affect the cold bias in the southern hemisphere, as already found for the 2 m temperature. A clear improvement can be seen in $\mathrm{ER_{pp}}$ (Fig. 4f), which removes both biases in the lower and middle troposphere in both hemispheres. We conclude that [..[86]]an eddy-resolving ocean resolution plays a major role for the mean-states of the large-scale temperature distribution in the atmosphere. Although the large cold bias above the Antarctic continent is present in all simulations, the

[74] removed: a consistent negative bias
[75] removed: that extends through
[76] removed: Although KPP reduces the bias over the Southern Ocean
[77] removed: and increases slightly the biases in the upper troposphere, the overall pattern
[78] removed: (except in $\mathrm{ER_{pp}}$
[79] removed: directly reduces the wind forcing of the ocean.
[80] removed: On the other hand, the eddy-resolving ocean does not modify
[81] removed: (Fig. 3f)
[82] removed: cross sections of the
[83] removed: , whereas with KPP only in the southern hemisphere
[84] removed: ,
[85] removed: slowing down of the
[86] removed: eddies play

bias is reduced in ER_{pp} by about $2\,°C$. The developing warm bias over the Weddell Sea in ER_{pp} can also be seen in the cross-section at roughly $60\,°S$.

4 Evaluation of the ocean mean state

4.1 Ocean surface temperature and salinity

4.1.1 Sea surface temperature

The sea surface temperature bias of MPI-ESM1.2 with respect to the UK MetOffice EN4 data (version 4.2.0; Good et al. (2013), averaged from 1945–1955) is shown in Fig. 5. We used this period for EN4 since our HR simulations were initialised from a simulation that was nudged to the averaged EN4 state of 1950–54, and we further allow for some variance. The results differ only marginally if another period is chosen (not shown). In general, biases occur in prominent areas and are affected by both changing the model resolution and the [..[87]]vertical ocean mixing scheme.

All simulations (except XR_{pp}) simulate realistic sea surface temperatures in comparison to EN4 (Fig. 5). [..[88]]About 1 to $2\,°C$ colder sea surface temperatures than in EN4 are simulated in the northern hemisphere [..[89]]by HR_{pp} (Fig. 5b). The strongest cold bias of up to $-7\,°C$ occurs in the North Atlantic between $40\,°N$ to $50\,°N$, centred at about $30\,°W$. A similar magnitude was described by Müller et al. (2018) for MPI-ESM1.2-HR. The main explanation for this cold bias, as given in section 3.1.2, is a too zonal NAC (Dengg et al., 1996), causing a too far southward intrusion of fresh and cold Labrador Sea water (Müller et al., 2018) [..[90]]and insufficient northward heat transport by the AMOC (Wang et al., 2014a). Another reason could be too much export of Mediterranean water at about 1000 m depth (Fig. 8), thus leading to a too strong halocline that inhibits vertical mixing.

Too cold sea surface temperatures are further simulated along the ACC (bias of $\sim 2\,°C$). Coastal upwelling areas west of Africa and South America are about 1 to $2\,°C$ too warm in all simulations with the T127 atmosphere (Fig. 5b,c,f), as found by Milinski et al. (2016)

Increasing the atmospheric resolution from T127 to T255, while using the PP scheme (XR_{pp}), causes a severe cold bias in the whole northern hemisphere (Fig. 5d), strongest in the North Atlantic ($-9\,°C$). This cooling was already described by [..[91]]Putrasahan et al. (2019) and is caused by a slowed AMOC due to [..[92]]weak wind stress over the subpolar gyre and [..[93]]weak northward heat and salt transports ([..[94]]Tab. 4, Fig. A1, and section 4.6). Although the reduced wind [..[95]]stress over

[87] removed: diapycnal
[88] removed: Colder sea surface temperatures of about
[89] removed: in
[90] removed: .
[91] removed: Putrasahan et al. (2018)
[92] removed: too
[93] removed: too
[94] removed: see also
[95] removed: forcing

the Southern Ocean (Fig. 1) might also contribute to a weakening of the AMOC (Toggweiler and Samuels, 1995) in XR$_{pp}$, [..[96]]Putrasahan et al. (2019) found no effect of this negative wind bias on the AMOC slow down, and argue that the timescale of the slowing AMOC is much faster than any feedback from the Southern Ocean to the North Atlantic.

On the other hand, the biases in the coastal upwelling areas diminished to some extent, because of the better resolved coastal wind systems. This warm bias reduction in the upwelling areas is consistent with other studies (Putrasahan et al., 2013; Small et al., 2015; Milinski et al., 2016). Furthermore, the Pacific cold-tongue almost disappears, but now the tropical Pacific becomes too warm south of the equator.

The [..[97]]cold bias in the North Atlantic diminishes drastically with the KPP scheme in HR$_{kpp}$ (Fig. 5c), but [..[98]]the warm bias in the Labrador Sea and in the Nordic Seas is enhanced because of an increased heat transport into the North Atlantic and its ambient seas (Fig. A1c). Moreover, a warm bias evolves in the tropical Pacific north and south of the equator. However, the KPP scheme simulates a stable AMOC in XR$_{kpp}$ (Fig. 5e), because of a stronger subpolar gyre (see Tab. 2). The enhanced deep convection and North Atlantic Deep Water (NADW) formation in the Labrador Sea (section 4.5) sustains a strong enough upper cell of the AMOC (section 4.6) and thus a sufficient northward transport of heat and salt (see [..[99]]Tab. 4 and Fig. A1c-d). This surplus in heat and salt transports, compared to XR$_{pp}$, prevents the Labrador Sea from freezing over. This finding is an important result and provides a solution to the declining AMOC strength for MPI-ESM1.2-XR. In addition, enhanced upwelling in the Southern Ocean further strengthens the northern cell of the AMOC (Marshall et al., 2017), although it is not the main reason in our model.

[..[100]]The cold bias along the ACC is clearly reduced in ER$_{pp}$ (Fig. 5f), because of resolving eddies that flatten and shift the outcropping isopycnals southwards. [..[101]]Furthermore, the cold biases in the North Atlantic, in the North Pacific, and in the Mediterranean Sea [..[102]]are reduced. The warm biases in the upwelling regions, however, remain because of the coarse T127 atmosphere.

4.1.2 Sea surface salinity

As with sea surface temperature, the sea surface salinity is well simulated [..[103]]by MPI-ESM1.2 for most parts of the ocean with respect to EN4 (Fig. 6). However, in some areas we find larger discrepancies. In the North Atlantic, the surface waters are too fresh where we already found a cold bias. This [..[104]]fresh bias is again caused by the too zonal NAC and the entrainment of fresher water masses from the Labrador Current. Although all models produce this bias, [..[105]]it is most pronounced in

[96]removed: Putrasahan et al. (2018)
[97]removed: KPP scheme reduces the
[98]removed: enhances a
[99]removed: also
[100]removed: ER$_{pp}$ clearly reduces the
[101]removed: It further reduces the cold bias
[102]removed: . The
[103]removed: with
[104]removed: freshwater
[105]removed: its magnitude differs with respect to HR$_{pp}$(

XR_{pp}, likely due to a too stable stratification in association with excessive export of salty water from the Mediterranean (compare with Fig. [..[106]]8d and Fig. A6d)

[..[107]]

The fresh bias in the North Atlantic (Fig. 6c) [..[108]]diminishes with using the KPP scheme or the eddy-resolving ocean[..[109]]. In both cases a stronger northward salt transport [..[110]]

is simulated in the Atlantic (Fig. A1d). In case of ER_{pp}, the Gulf Stream separation is better represented, which further reduces the bias in the North Atlantic (Fig. 6f). The resolved eddies further remove the [..[111]]fresh bias along the ACC. The water masses in the Mediterranean Sea become more saline, which removes the [..[112]]fresh bias that the HR and XR models produce.

Increasing the atmospheric resolution from T127 to T255 enhances the [..[113]]fresh bias in XR_{pp} (Fig. 6d) because of the above described AMOC slow down, with the consequence that less salt is transported by the Gulf Stream and the NAC into the North Atlantic (Fig. A1c-d). In XR_{kpp} (Fig. 6e), both effects work in opposite directions and almost balance each other, so that the bias is similar to that in HR_{pp}.

Another bias present in all simulations is a too saline near-surface Arctic Ocean, originating from the Siberian coast that extends across the Transpolar Drift, but also into the Canadian basin. These too saline waters indicate too little freshwater input from the Siberian rivers, in particularly from the Lena river (Laptev Sea). Another effect that enhances this error could be too little barotropic tidal mixing along the Arctic shelves and thus too [..[114]]little horizontal spreading of the river waters (Wang et al., 2014b).

Finally, a strong [..[115]]fresh bias is simulated in the western tropical Pacific. The KPP scheme [..[116]]does not ameliorate this problem as the surface waters become severely fresher in both XR simulations [..[117]](Fig. 6d-e). In general, all models simulate too little precipitation or too much evaporation for most parts of the globe (Fig. A2). In the western Pacific, the XR models even simulate slightly less precipitation (Fig. A2d-e), so that we suspect that the supply of salty waters from the east [..[118]]is reduced in XR thus enhancing the fresh bias.

[106] removed: 6a) by either increasing the model resolution or by replacing the vertical mixing scheme in the ocean.

[107] removed: Both the KPP scheme

[108] removed: and

[109] removed: reduce the freshwater bias in the North Atlantic, because of

[110] removed: by the NAC and because more saline waters are exported from the Labrador Sea along the Deep Western Boundary Current.

[111] removed: freshwater

[112] removed: freshwater

[113] removed: freshwater

[114] removed: less

[115] removed: freshwater

[116] removed: seems not to modify this bias, but

[117] removed: . Since there is no obvious difference in precipitation or evaporation (not shown),

[118] removed: reduces in XR . Although still too fresh , ER_{pp} reduces this bias.

4.2 Ocean interior

Figure 7 shows the time-mean zonal-mean temperature bias of the MPI-ESM1.2 simulations to EN4 for the Atlantic and the Arctic Ocean. The bias of the HR and XR simulations are very similar and show a maximum warm bias at roughly 40° S, continuing to 30° N at depths of the AAIW (about 800 to 1000 m). These biases are thought to be caused by erroneous interior circulation, tracer advection and mixing due to unrepresented eddy-induced tracer transports (Griffies et al., 2009; Jungclaus et al., 2013).

The warm bias at 40° S is related to [..[119]]enhanced advection of warm and salty waters from the Indian Ocean [..[120]](Fig. A5 and Fig. A6), because the resolution is still too low to represent the Agulhas Current system (Jungclaus et al., 2013), with its retroflection and intermittent eddy shedding that transfers heat and salt into the Atlantic. [..[121]]The retroflection is not well present in HR/XR [..[122]]with the TP04 grid, so that a constant Agulhas leakage transports [..[123]]too warm and too salty water into the South Atlantic (Fig. A7). Neither the KPP scheme (Fig. 7c) nor the T255 atmosphere (Fig. 7d,e) reduces this warm bias. [..[124]]On the contrary, with the KPP scheme, the inflow becomes stronger so that more heat and salt is exchanged (Fig. A1a-b and Fig. A7b,d). The warm bias and the high salinity bias (Fig. 8) vanish only with the eddy-resolving ocean grid (TP6M) in ER_{pp} (Fig. 7f), [..[125]]which is also clearly visible at 740 m depth (Fig. A5 and Fig. A6), because less warm and salty water from the Agulhas Current flow into the South Atlantic (Fig. A7e). This improvement was also reported by von Storch et al. (2016) for ocean-only simulations. There are two reasons for this warm bias reduction in ER_{pp}: (1) the Agulhas Return Current, Agulhas Retroflection and the Agulhas leakage are now better resolved, producing a more realistic circulation and water mass transfer from the Indian Ocean into the South Atlantic, as seen in other similar studies (McClean et al., 2011; Putrasahan et al., 2016; Cheng et al., 2018); and (2) the eddy-induced cooling and freshening of the intermediate ocean (von Storch et al., 2016) further reduces the warm bias.

The warm bias in Fig. 7a-e stretches northward at the depth of the Antarctic Intermediate Water (AAIW) and shows another maximum at 30° N that is related to the spreading of Mediterranean waters. The HR and XR models use the same TP04 ocean grid and simulate both the observed net volume transport through the Strait of Gibraltar (net inflow of about 0.04 Sv; see Tab. 3). In the TP04 grid, the strait is about 54 km wide with a sill depth of about 230 m. The outflowing Mediterranean water is too warm and too saline in all HR and XR simulations compared to EN4 (see Fig. A5 and Fig. A6), which explains the warm and saline bias (Fig. 8a-e). [..[126]]The Mediterranean water is slightly more saline in HR_{kpp} than in HR_{pp}, so that the water spreading northward along the European continental shelf becomes also more saline and contributes to saltier Northeastern Atlantic Deep Water. This enhanced flow of saline water into the subpolar gyre explains the reduced salinity bias at 40 to 50° N at a depth

[119] removed: too much

[120] removed: (Jungclaus et al., 2013)

[121] removed: In the

[122] removed: configurations

[123] removed: warm and salty water, instead

[124] removed: It reduces

[125] removed: as

[126] removed: In HR_{kpp}, the

of 1000-1500 m (Fig. 8c). The main spreading pathway in all HR and XR models, however, is to the southwest into the open Atlantic.

As with the warm biases, the salinity biases [..[127]]disappear in ER_{pp} (Fig. 7f and Fig. 8f). A fresher water mass at intermediate depth reflects a much more realistic representation of the AAIW (Fig. [..[128]]8 and in detail in Fig. A8) and of the outflow of Mediterranean water. The latter is less saline and about 2 to 3 °C colder ([..[129]]also shown at a depth of 740 m; Fig. [..[130]]A5f and Fig. [..[131]]A6f), reducing the warm and saline bias at 30 °N. The reason for this major improvement is the better resolved bathymetry of the Strait of Gibraltar, which is about 24 km wide in the TP6M grid. Although the salinity maximum of the overflow water is about 100 m shallower than in EN4 (not shown), ER_{pp} produces more realistic properties of upper and intermediate depth water masses.

[..[132]]Although the Gulf Stream separates earlier from the American coast in ER_{pp} (not shown), its flow path is still too zonal, such that the cold bias in the North Atlantic [..[133]]at around 50 °N (Fig. 7) is not removed. This indicates that an eddy-resolving ocean alone does not solve the cold-bias issue in the North Atlantic. In fact, Fig. A5f suggests that the cold bias is substantially larger in ER_{pp} than in any of the other simulations.

The too warm and saline subpolar gyre causes a warm and saline bias in the deep convection areas of the Labrador and Irminger Seas, centred around 60 °N (Fig. 7, Fig. 8, and Fig. A5). The bias [..[134]]is larger in HR_{kpp} because of the increased transport of heat and salt from the [..[135]]subtropical gyre into the subpolar gyre. The bias [..[136]]is reduced in the XR models because of the weaker subpolar gyre and the reduced salt transport by the gyre. However, from Fig. 8d, we see that the reduced salinity is the main factor causing the reduced convection in XR_{pp} (also supported by Fig. A1d), as described by [..[137]]Putrasahan et al. (2019). Another contribution is too warm [..[138]]overflow waters from the Nordic Seas, an issue that was also present in coarser MPI-ESM versions (Jungclaus et al., 2013). [..[139]]This warm bias of the overflow waters is mostly unaffected in ER_{pp}.

The Atlantic water entering the Arctic Ocean (0 °C potential temperature bounds in Fig. 7a) is too warm and its layer is too thick in all HR and XR simulations (Fig. 7b-e), causing a warm bias within the Atlantic layer between 200 m to 1000 m. This is a common error in ocean general circulation models (Ilicak et al., 2016), which is thought to be caused by spurious numerical mixing of the advection operator (Holloway et al., 2007). Zhang and Steele (2007) further found a direct impact of

---

[127] removed: reduce

[128] removed: A3

[129] removed: not shown), reducing the warm and saline bias at 30 °N (

[130] removed: 7

[131] removed: 8f)

[132] removed: The too zonal NAC causes a cold and fresh bias between 40 to 50 °N in the upper ocean (above 1000 m depth) in all simulations (Fig. 7 and Fig. 8).

[133] removed: improves only marginally.

[134] removed: increases

[135] removed: Subtropical Gyre

[136] removed: reduces

[137] removed: Putrasahan et al. (2018)

[138] removed: and saline

[139] removed: The bias

the vertical mixing strength [..[140]]on the circulation of the Atlantic Water into the Arctic Ocean. Reducing the vertical mixing in the European Basin reduces the diffusion of the Atlantic Water and results in a thinner layer. By comparing the vertical mixing across all our simulations (Fig. [..[141]]A3) we see that ER_{pp} simulates less vertical mixing in the Arctic Ocean at the depth of the Atlantic Water layer (as well as in the deeper layers of the Arctic Ocean and Atlantic), thereby readily removing the warm bias in the Atlantic Water layer. At 740 m depth, XR_{pp} shows an even fresher Atlantic water layer throughout the Arctic Ocean and the GIN Sea (Fig. A6). Combined with the high salinity bias at the surface (Fig. 6d) in the Arctic Ocean, this implies a weakening of the Arctic halocline, also reflected by strong vertical mixing in the upper layers of the Arctic Ocean (Fig. A3c).

Further, less vertical mixing in the Fram Strait can reduce the inflow of Atlantic Water into the Arctic Ocean (Zhang and Steele, 2007) and thus reduce the warm bias as [..[142]]in ER_{pp}. In fact, Zhang and Steele (2007) recommend to reduce the background diffusivity to $1 \cdot 10^{-6}\,\mathrm{m^2\,s^{-1}}$ and viscosity to $1 \cdot 10^{-5}\,\mathrm{m^2\,s^{-1}}$. The background value for diffusivity is thus an order of magnitude lower than in our configuration. Sein et al. (2018) used an even lower background diffusivity in the Arctic Ocean of about $1 \cdot 10^{-6}\,\mathrm{m^2\,s^{-1}}$ in FESOM that is two orders of magnitude lower than in the default version 1.4 (Wang et al., 2014b). However, our results show that an eddy-resolving resolution [..[143]]in the Arctic Ocean removes the warm and saline bias in the Atlantic Water layer, without changing any background values for vertical mixing. [..[144]]The benefit of a very high-resolution [..[145]]for the Arctic Ocean was recently [..[146]]demonstrated by Wang et al. (2018), who used a background diffusivity of $1 \cdot 10^{-5}\,\mathrm{m^2\,s^{-1}}$, which is close to what we chose. [..[147]]

4.3 Ocean circulation

To evaluate the large-scale ocean circulation, we compared barotropic volume transport stream functions of selected regions, transports through straits, and the AMOC. Overall we find three effects: (1) increasing the atmospheric resolution to T255 reduces the gyre strengths, (2) the KPP scheme enhances the strength of all gyres, and (3) the effect of an eddy-resolving ocean is bi-directional.

The simulated subpolar gyre strengths in the North Atlantic range from 31.0 to $40.6\,\mathrm{Sv}$ and are all within the observational range of 26.0 to $40.0\,\mathrm{Sv}$ (Tab. 2). HR_{kpp} simulates a [..[148]]stronger subpolar gyre ($+6\,\mathrm{Sv}$) than the reference simulation HR_{pp}. Both XR_{pp} and XR_{kpp} show [..[149]]weaker gyres compared to their respective HR counterpart, whereas ER_{pp} simulates a slight increase of the gyre strength.

[140] removed: onto
[141] removed: A1
[142] removed: ER_{pp} does
[143] removed: the
[144] removed: That
[145] removed: is necessary
[146] removed: shown by Wang et al. (2018)as well
[147] removed: In contrast, for example Sein et al. (2018) chose to reduce the background value by one order of magnitude.
[148] removed: slightly
[149] removed: a clear drop of the gyre strength with a T255 atmosphere, as described by Putrasahan et al. (2018). In contrast, increasing the ocean resolution to eddy-resolving (ER_{pp}) does not affect the subpolar gyre strengthnoticeably.

The volume transport of the [..[150]]subtropical gyre in the North Atlantic, however, reacts more [..[151]]sensitively to the chosen vertical ocean mixing scheme and [..[152]]to resolving of ocean eddies. Compared to the reference of $48.2\,\mathrm{Sv}$ (HR_{pp}), the gyre strength [..[153]]decreases slightly to $44.0\,\mathrm{Sv}$ with a higher atmospheric resolution (XR_{pp}). By using the KPP scheme, however, the gyre strength increases to $64.9\,\mathrm{Sv}$ (HR_{kpp}) and remains similarly high with a T255 atmosphere (XR_{kpp}). ER_{pp} produces a gyre strength as strong as with the KPP scheme. [..[154]]With that, the strength of the North Atlantic subtropical gyre of the KPP and ER simulations slightly exceeds the bound of the observed range, while that of the PP simulations hovers around the other end of the observed range. In the case of HR_{kpp} and XR_{kpp} [..[155]]the too strong volume transport of the subtropical gyre might further contribute to the positive salinity bias in the [..[156]]subpolar gyre at a depth of 500 to 1000 m (Fig. 8 and Fig. A6). As for the strength of the subtropical gyre of the North Pacific, the relative differences among the simulations are similar, except that ER_{pp} [..[157]]reveals a markedly reduced strength relative to the KPP simulations. Furthermore, all simulations produce a considerably stronger North Pacific gyre than what has been derived from observations

Tab. 3 summarizes the transports through important passages. The net volume transport through the Bering Strait is of the same magnitude (0.6 to $0.7\,\mathrm{Sv}$) for HR_{pp}, HR_{kpp} and XR_{kpp}, which is on the lower side of the observations (0.7 to $1.1\,\mathrm{Sv}$). The transport is even lower ($0.5\,\mathrm{Sv}$) in XR_{pp}, which indicates a low exchange [..[158]]between the Arctic and the Pacific Ocean. Increasing the ocean resolution leads instead to a higher transport of $0.9\,\mathrm{Sv}$ in ER_{pp}. As with the improved outflow of Mediterranean Water through Strait of Gibraltar in ER_{pp}, this improvement is due to a better resolved Bering Strait.

The simulated net transport through Fram Strait [..[159]]is in the range of the observations ($-1.75 \pm 5.01\,\mathrm{Sv}$), which show a strong interannual variability (Fieg et al., 2010). A possible explanation for [..[160]]the somewhat lower transport with KPP is given by Zhang and Steele (2007). They found that strong vertical mixing, as with the KPP scheme in our HR and XR simulations, deepens the Atlantic Water layer, but simultaneously weakens the inflow [..[161]]of Atlantic Water and the outflow [..[162]]of Arctic Water. [..[163]]

In our KPP simulations, the outflow becomes weaker compared to the PP simulations, whereas the inflow is of similar magnitude, so that the net transport is lower. However, in comparison to the HR and XR simulations, the net transport in ER_{pp} is [..[164]]only half on average. In agreement with Fieg et al. (2010), the West Spitsbergen Current (WSC) is better

[150] removed: Subtropical Gyre
[151] removed: sensitive
[152] removed: the eddy-resolving resolution
[153] removed: only slightly reduces
[154] removed: However, compared to observations (46.0 to $61.0\,\mathrm{Sv}$), ER_{pp} and the simulations with KPP simulate slightly stronger transport
[155] removed: this might explain
[156] removed: North Atlantic.Similar findings results for the Subtropical Gyre in the Pacific,
[157] removed: reduces the gyre strength .
[158] removed: of the Arctic Ocean
[159] removed: , however, is too low in all simulations and reduces further with either an eddy-resolving grid or the KPP scheme
[160] removed: this reduced
[161] removed: strength
[162] removed: strength
[163] removed: However, the transport by
[164] removed: even lower. The reason for this has to be further investigated

resolved in the eddy-resolving ER_{pp}. The WSC, and thus the inflow of Atlantic Water into the Arctic Ocean, is much stronger in ER_{pp}, as is its return circulation north of 80 °N. This intensified WSC and its recirculation cause a reduction of the net volume transport through Fram Strait. Considering the high uncertainty of the net transport from observations, all simulations give realistic estimates but the most realistic simulation with respect to the temperature and salinity structure and to the circulation is ER_{pp} (not shown).

The overflows through Denmark Strait and across the Iceland-Scotland ridge are important deep water connections for the Arctic and the Atlantic. [..[165]]All simulations produce realistic overflow [..[166]]volumes with respect to observations, [..[167]]which are on average slightly higher in the eddy-resolving [..[168]]simulation (ER_{pp})[..[169]], but still within the standard deviation of the coarser simulations. The higher transport in HR_{kpp} [..[170]]versus HR_{pp} is caused by enhanced deep convection in the Nordic Seas, particularly in the Greenland Sea (Fig. 10).

In all HR and XR simulations, the volume transport of the Florida Current is only about half the observed value of roughly 32 Sv (Tab. 3). Although the transport increases with the KPP scheme, only ER_{pp} [..[171]]simulates a considerably (about 10 Sv) stronger transport, amounting to about 25 Sv. [..[172]]We found similar results for the Indonesian throughflow, which is important for climate because it connects the Pacific with the Indian Ocean and closes the upper warm branch of the MOC. Again KPP enhances the transports slightly, but only ER_{pp} simulates a transport strength that is similar to observed values.

The Mozambique channel is an example where both a T255 atmosphere and KPP show a reduction in the transports. In ER_{pp}, however, the transport is about twice as high as in the other simulations and more realistic with respect to recent observations of 16.7 ± 8.9 Sv (Ridderinkhof et al., 2010). The ability to resolve eddies, particularly the Mozambique eddies along with a better resolved southward advection [..[173]]through the Mozambique Channel[..[174]], contributes to the more realistic transport of about 14 Sv in ER_{pp} (Putrasahan et al., 2016; Ridderinkhof et al., 2010).

The observed baroclinic transport through the Drake Passage was [..[175]]commonly estimated at roughly 140 Sv. However, [..[176]]a new estimate reveals a much higher transport volume of about 173.3 ± 10.7 Sv, [..[177]]when adding the barotropic transport [..[178]](Donohue et al., 2016). With regard to this [..[179]]estimate, the models are within or close to the observed

[165] removed: Although all

[166] removed: values

[167] removed: we found systematic effects of either increasing the model resolution or using KPP. Both, increased model resolution and the KPP scheme increase the strength of overflows. In particular

[168] removed: ocean

[169] removed: produces more overflow waters. In the case of HR

[170] removed: , this higher transport

[171] removed: strengthens the transport considerably to

[172] removed: This indicates that the eddy-resolving ocean has a clear impact on this current.

[173] removed: throughout

[174] removed: likey

[175] removed: usually stated as

[176] removed: recently

[177] removed: if

[178] removed: is added

[179] removed: estimation

[..[180]]range. However, compared to the reference simulation HR$_{pp}$ (161.1 Sv) the transport [..[181]]weakens to about 150.0 Sv in XR$_{pp}$, and from 191.9 Sv in HR$_{kpp}$ to 170.3 Sv in XR$_{kpp}$. In ER$_{pp}$ the transport is lower than in all other [..[182]]simulations (about 141 Sv). These results confirm that a higher atmospheric or ocean resolution reduces the transport in the Drake Passage, [..[183]]consistent to what has been found Stössel et al. (2015). In contrast, the transport through Drake passage is enhanced when using the KPP scheme[..[184]], probably because of enhanced deep convection in the Weddell Sea (Fig. 11) that steepens the isopycnals across the ACC and thus increases the geostrophic flow (Stössel et al., 2015; Naughten et al., 2018) (see section 4.5.2). This may be an indication of the parameterized eddy effect of flattening the isopycnals being too low in the KPP simulations with the chosen GM coefficient.

4.4 Sea ice

4.4.1 Arctic Ocean

The spatial distribution of sea ice thickness [..[185]](Fig. 9) agrees well with the PIOMAS reanalysis [..[186]](averaged from 1979–2005) (Zhang and Rothrock, 2003; Schweiger et al., 2011) and is comparable to the MPI-ESM1.2-HR simulation described by Müller et al. (2018). The sea ice extent is in good agreement with the observations from the EUMETSAT OSI SAF (OSI-409-a; v1.2) product (averaged from 1979–2005) (EUMETSAT Ocean and Sea Ice Satellite Application, 2015), except for XR$_{pp}$ in which the Labrador Sea freezes over. In general, the maximum ice thickness (multi-year ice) in March is [..[187]]found along the north coast of Greenland and of the Canadian Archipelago[..[188]], and reaches about 5 m in PIOMAS but only 3 m in HR$_{pp}$. The ice [..[189]]is slightly thicker in this area in the simulations with HR[..[190]]$_{kpp}$[..[191]]. In the Iceland Sea, HR$_{kpp}$ simulates less sea ice, which is in better agreement with the observations in that the ice cover does not reach as far south as Iceland as in [..[192]]HR[..[193]]$_{pp}$ (Fig. 9b). The enhanced northward heat transport into the Nordic Seas in HR$_{kpp}$ results in warmer sea surface temperatures there, leading to a northward shift of the winter ice edge. Further, a stronger recirculating branch of the West Spitsbergen Current in the Fram Strait (not shown) in HR$_{kpp}$ pushes the East Greenland Current westwards to the east coast of Greenland, [..[194]]thereby becoming narrower and faster, so that sea ice is constrained to a narrower band along the coast. [..[195]]In XR$_{kpp}$, however, the sea surface temperature is colder than in HR$_{kpp}$, so that the sea ice reaches

[180] removed: estimation
[181] removed: reduces
[182] removed: models with 140.9 Sv
[183] removed: as described by Stössel et al. (2015), while
[184] removed: enhances the transport
[185] removed: distribution
[186] removed: (Zhang and Rothrock, 2003; Schweiger et al., 2011) (not shown)
[187] removed: generally
[188] removed: (Fig. 9)
[189] removed: cover in HR
[191] removed: reaches far south to Iceland
[192] removed: the Denmark Strait, as described by Müller et al. (2018), but remains close to Greenland's coast in HR
[194] removed: which narrows and becomes
[195] removed: The sea ice thickness reduces also in the Eurasian Basin by about 0.25 m to 0.5 m in HR$_{kpp}$, while

Iceland as in the reference simulation. Compared to HR_{pp}, the sea ice thickness of HR_{kpp} is slightly lower in the Eurasian Basin, although it becomes thicker in the Canadian Basin[..[196]]

. XR_{pp} (Fig. 9c) simulates [..[197]]more, although thin, sea ice in the Labrador Sea because of the above described fresher and colder North Atlantic and the resulting freeze-over[..[198]]. The sea ice cover in the Iceland Sea reaches even further south than in the reference simulation HR_{pp}. In contrast, in XR_{kpp} (Fig. 9d) [..[199]]the ice thickness and extent in the Labrador Sea is similar to that in HR_{pp}. However, due to colder sea surface temperatures in the Denmark and Fram Strait [..[200]]than in HR_{kpp}, a southern tongue of sea ice extends to Iceland as in HR_{pp}. Further, in contrast to HR_{kpp} [..[201]]the recirculating branch of the West Spitsbergen Current does not become [..[202]]stronger in the XR simulations (not shown).

In addition, the near-surface circulation in the Arctic Ocean changes with a T255 atmosphere from a more anticyclonic circulation in the Makarov and Canadian Basin in HR, to a more cyclonic circulation in XR (not shown). A cyclonic circulation enhances the export of cold Arctic Water via the East Greenland Current, causing colder sea surface temperatures in the Nordic Seas. [..[203]]The XR simulations and ER_{pp} [..[204]]produce thinner winter ice in the Canada Basin[..[205]], which may be related to the changed circulation, but has to be further investigated. ER_{pp} [..[206]]produces in general less sea ice volume in the Arctic Ocean than the HR/XR simulations.

The extent of the Arctic summer ice cover in September is less and thus more realistic in the XR than in the HR [..[207]]simulations (not shown), in particular over the Siberian shelves, which is probably caused by the better resolved T255 atmosphere. KPP again simulates thinner ice in the Canada basin (about $-0.5\,\mathrm{m}$).

4.4.2 Southern Ocean

The spatial distribution of austral winter (September) sea ice thickness [..[208]]in the Southern Ocean of HR_{pp} (not shown) is similar to the MPI-ESM1.2-HR simulations described by Müller et al. (2018). The ER and both HR simulations produce an overabundance of open-ocean polynyas in the Weddell Sea (see section 4.5.2). HR_{kpp} simulates less and thinner ice in the Weddell Sea than HR_{pp}, but otherwise the spatial distribution of sea ice in the Southern Ocean is very similar.

Both XR simulations, but more so XR_{pp}, produce thicker sea ice than the other simulations, in particular in the Weddell Sea and close to Antarctica's coasts. The thicker ice in the Weddell Sea emerges in concert with a reduced number of polynyas, so that the warm bias seen in Fig. 2 vanishes. This less frequent occurrence of Weddell Sea polynyas is probably related to a

[196] removed: by the same amount.

[197] removed: much moresea ice reaching the north coasts of Iceland

[198] removed: of the Labrador Sea . Instead,

[199] removed: simulates thicker sea ice

[200] removed: because of colder sea surface temperatures. In

[201] removed: ,

[202] removed: not stronger in XR_{kpp} (and XR_{pp}).

[203] removed: Both XR models

[204] removed: simulate

[205] removed: as well. For both XR it can be explained by an enhanced ice export due to the more cyclonic circulationmentioned above. For ER

[206] removed: , however, it needs to be investigated.

[207] removed: models

[208] removed: distribution

reduced meridional pressure gradient across the Weddell Sea and the ACC (not shown), which in turn reduces the near-surface wind speed [..[209]]bias (as seen in Fig. 1)[..[210]]. However, a more detailed investigation is required to explain circulation differences between the T127 and the T255 atmospheres over the Weddell Sea. In austral summer, [..[211]]both XR models produce thicker ice in the Weddell Sea [..[212]](not shown)[..[213]], so that the ocean is insulated from the cold atmosphere above, resulting in less convective mixing.

4.5 Mixed layer depth and diapycnal mixing

4.5.1 Northern hemisphere

[..[214]]Fig. 10 shows the average mixed layer depths in March for the northern [..[215]]North Atlantic. We diagnosed the mixed layer depth as the depth where the density deviates from the surface density by $\sigma_t = 0.01\,\mathrm{kg\,m^{-3}}$. This diagnostic was computed from monthly means.

In the reference simulation $\mathrm{HR_{pp}}$ (Fig. 10a), [..[216]]March-mean depths of up to $1500\,\mathrm{m}$ are simulated in the Labrador Sea, and up to $600\,\mathrm{m}$ south of Cape Farewell, in the Irminger Sea, and in the Nordic Seas. As discussed before, in $\mathrm{XR_{pp}}$ (Fig. 10c) the deep convection [..[217]]in the Labrador Sea [..[218]]ceases within the first two decades of the simulation. This collapse of deep convection (together with that in the Nordic Seas[..[219]]) leads to a slowing down of the AMOC (Tab. 4) [..[220]](Putrasahan et al., 2019).

The KPP scheme in $\mathrm{HR_{kpp}}$ (Fig. 10b) causes much deeper mixed layers in the Labrador Sea and [..[221]]in the Greenland Sea. In particular the [..[222]]mixed layer depths in the Labrador and Irminger Sea and south of Greenland (north of $50\,^\circ\mathrm{N}$) [..[223]]become deeper compared to all other [..[224]]simulations. These deeper mixed layers with the KPP scheme result on one hand from the convection parameterization (i.e. the non-local fluxes) and on the other hand from a stronger and more cyclonic subpolar gyre (Tab. 2) that domes the isopycnals in the gyre centres (not shown), which preconditions the water column for convection.

[209] removed: forcing
[210] removed: for the polynya
[211] removed: the sea ice extends further into
[212] removed: in both XR simulations
[213] removed: .
[214] removed: The average surface
[215] removed: hemisphere are shown in Fig. 10
[216] removed: average
[217] removed: ceases
[218] removed: and
[219] removed: , leading
[220] removed: .
[221] removed: mixed layers depths of about $1000\,\mathrm{m}$
[222] removed: convection area
[223] removed: becomes
[224] removed: models

As mentioned in section 2.2, the non-local fluxes in the KPP scheme [..[225]]have the same vertical diffusivities as for the local gradient transports. These diffusivities are not limited to a user-defined maximum value during convective forcing conditions, so that much larger diffusivities can act to redistribute temperature and salinity [..[226]]throughout the ocean water column, causing it to overturn faster and to produce deeper mixed layers [..[227]]with the KPP than [..[228]]with the PP scheme.

On the other hand, XR_{kpp} (Fig. 10d) simulates shallower mixed layers compared with HR_{kpp}. These shallower mixed layers result from the reduced wind stress of the T255 atmosphere by means of two processes: (1) [..[229]]less positive wind stress curl spins down the subpolar gyre, so that the slower cyclonic circulation reduces the isopycnal doming and the horizontal salt advection to the gyre centres (Tab. 4), leading to a more stratified surface layer; and (2) lower near-surface wind speeds reduce the turbulent air-sea fluxes via the bulk formula and the surface friction velocity (u_*). Lesser heat fluxes in turn reduce directly the non-local fluxes of the KPP scheme in convection areas, and lower u_* reduces the turbulent vertical velocity scales, which results in lower vertical diffusivities and viscosities.

Based on these results, increasing the atmospheric resolution reduces the mixed layer depths over the North Atlantic and the Nordic Seas, whereas KPP deepens them. By combining both, the T255 atmosphere and the KPP scheme, the above effects compensate each other (XR_{kpp}; Fig. 10d). In contrast to XR_{pp}, where the convection ceases in the Labrador and GIN [..[230]]seas, the combination of T255 and KPP (XR_{kpp}) produces more realistic mixed layers depths even with reduced wind [..[231]]stress.

Overall, the KPP scheme [..[232]]modifies the large-scale circulation by simulating a stronger subpolar gyre, which in turn provides favourable conditions for deep convection in the Labrador Sea, Irminger Sea, and Nordic Seas. For this reason, HR_{kpp} [..[233]]simulates enhanced deep convection compared with HR_{pp}[..[234]], in particular in the Labrador and GIN Seas. In the Irminger Sea, mixed layer depths of about 400 to 500 m [..[235]]are simulated by both HR_{kpp} and XR_{kpp}, which is consistent with retrievals from observations (e.g. Pickart et al., 2003; Våge et al., 2008, 2011). [..[236]]However, even the T255 atmosphere is too coarse to fully simulate Greenland tip jets [..[237]](e.g. Martin and Moore, 2007; DuVivier and Cassano, 2016; Gutjahr and Heinemann, 2018), which have a considerable impact on triggering deep convection in the Irminger Sea due to strong associated turbulent heat and momomentum fluxes driving the Irminger Gyre, so that the mixed layer depth may be underestimated in winters with high tip jet activity.

[225] removed: use
[226] removed: , causing the water column
[227] removed: in
[228] removed: in
[229] removed: lower wind stress
[230] removed: Seas
[231] removed: forcing
[232] removed: influences
[233] removed: and XR_{kpp} simulate
[234] removed: and thus mixed layers deeper of about 500 to 600
[235] removed: in the Irminger Gyre
[236] removed: The deeper mixed layers in the Irminger Sea in XR_{kpp} are probably linked to better resolved
[237] removed: , although a T255 is still too coarse to resolve them sufficiently (Gutjahr and Heinemann, 2018).

[..[238]]

The mixed layer depths in the Labrador Sea are nevertheless too deep (excluding XR_{pp}). A possible explanation is the neglect of tidal mixing in MPI-ESM1.2. As shown [..[239]]by Müller et al. (2010), tidal mixing improves the recirculation of the Labrador Current. By [..[240]]entraining more freshwater into the surface layer of the Labrador Sea, it becomes more stratified which in turn reduces deep convection. Another shortcoming is probably insufficient eddy activity in the Labrador Sea so that too little freshwater is transported from the West Greenland Current into the interior of the Labrador Sea (e.g. Eden and Böning, 2002; Kawasaki and Hasumi, 2014).

In ER_{pp} the mixed layer depths are to a large extent similar to our reference simulation HR_{pp}. However, in ER_{pp} the convection centre in the Labrador Sea is confined to a more southeastern area with deeper mixed layers, in particular south of Cape Farewell. The deeper mixed [..[241]]layers might be related to a stronger doming of isopycnals because of an enhanced cyclonic circulation [..[242]]or recirculating Irminger Current [..[243]](Pickart et al., 2003; Våge et al., 2011). Another reason could be enhanced advection of Labrador Sea water from the Labrador into the Irminger Basin that preconditions the water south of Cape Farewell for convection. However, the processes that lead to deep convection in the Irminger Sea are complex, and it is still not fully understood how eddies affect the preconditioning/triggering of convection and where their main formation area is (Fan et al., 2013; DuVivier and Cassano, 2016).

4.5.2 Southern hemisphere

In the Southern Ocean, we define the mixed layer depth as the depth where the density deviates by [..[244]]$\sigma_t = 0.03\,\mathrm{kg\,m^{-3}}$ from the surface. MPI-ESM1.2 simulates very deep winter mixed layers in the Weddell and Ross Sea (Fig. 11). In the Weddell Sea, the convection reaches down into the deep ocean, which is a known problem in many state-of-the-art ESMs (Sallée et al., 2013; Kjellsson et al., 2015; Heuzé et al., 2015; Naughten et al., 2018). Spurious open-ocean deep convection leads to semi-permanent Weddell Sea polynyas, as warm Circumpolar Deep Water is continuously brought to the surface, causing sea ice to melt so that the ocean becomes exposed to the cold atmosphere.

Possible explanations for this widespread bias are: insufficient freshwater input (Kjellsson et al., 2015), in particular glacial melt water (e.g. Stössel et al., 2015), and insufficient wind mixing in summer (Timmermann and Beckmann, 2004). Reduced wind mixing allows salt from brine rejection to accumulate in the winter water layer and eventually to erode the stratification. In both cases, salinity increases in the winter [..[245]]upper layer until the weakly stratified water column overturns (Naughten et al., 2018).

[238] removed: Except for XR_{pp}, the maximum
[239] removed: in
[240] removed: dragging
[241] removed: layer depths
[242] removed: (or a
[243] removed:) (Pickart et al., 2003; Våge et al., 2011)and to
[244] removed: $0.03\,\mathrm{kg\,m^{-3}}$ from the density at the
[245] removed: water

The diagnosed mixed layer depth, however, is very sensitive to the chosen density threshold because of the very weakly stratified water column. We decided to apply a commonly used threshold for the Southern Ocean of $\sigma_t = 0.03\,\mathrm{kg\,m^{-3}}$[..[246]], but note, however, that if a lower threshold of $\sigma_t = 0.01\,\mathrm{kg\,m^{-3}}$ is chosen, the mixed layer depth rarely exceeds 300 m, because of a shallow stratified surface layer.

Based on two simulations with the GFDL-ESM with different resolutions of their ocean component (0.25° and 0.1°), Dufour et al. (2017) found that deep convection in the Weddell Sea does not necessarily lead to open-ocean polynyas. They argue that excessive vertical mixing in the lower-resolution ocean component hinders the build-up of a heat reservoir at depth that is necessary for Weddell Sea polynyas to occur intermittently as expected under pre-industrial conditions (e.g. de Lavergne et al., 2014; Gordon, 2014). They further argue that the more realistic representation in the higher-resolution simulation stems from (1) the fact that mesoscale eddies tend to flatten isopycnals thereby increasing the stratification, and (2) the more detailed bathymetry which allows for a better simulation of dense-water overflows.

Based on forced MPIOM and coupled MPI-ESM simulations with varying resolution, Stössel et al. (2015) found that the [..[247]]Southern Ocean winter [..[248]]sea ice and water properties [..[249]]of a 0.1° (TP6M) ocean [..[250]]simulation improved considerably upon switching from a forced to a coupled [..[251]]mode of operation, largely due to an associated increase in surface freshwater flux. These findings are consistent with our $\mathrm{ER_{pp}}$ simulation (Fig. 11e), where the mixed layer depth in the central Weddell Sea [..[252]]is overall reduced in comparison with $\mathrm{HR_{pp}}$ (Fig. 11a). At the same time, the area of deep mixed layers shifts to the eastern part of the Weddell Sea, close to the Maud Rise plateau, where $\mathrm{ER_{pp}}$ still simulates very deep mixed layers in September. This, in turn, could be a result of the better resolved bathymetry in this region. Kurtakoti et al. (2018) explained how Maud Rise polynyas formed in a high-resolution (0.1° ocean component) ESM simulation[..[253]], while none formed in a low-resolution simulation with the same model. A decisive reason for this was the steeper and better resolved bathymetry of and around Maud Rise that allowed for sufficiently strong Taylor columns to form.

[..[254]]For the larger Weddell Sea polynyas, de Lavergne et al. (2014) and Gordon (2014) argue that such should only emerge under pre-industrial conditions. Even though de Lavergne et al. (2014) praise the low-resolution MPI-ESM for belonging to the class of convecting models, Kurtakoti et al. (2018) explain that large-scale Weddell Sea polynyas should only occur intermittently under pre-industrial conditions and only by growing out from Maud Rise polynyas, which themselves should only occur at high model resolution (0.1°). Since the greenhouse gas forcing of the experiments presented here [..[255]]are fixed at the 1950 level, one would expect the Southern Ocean of the model to already have adjusted to the present-day situation when no Weddell Sea polynyas are expected to occur (due to the southward shift of the precipitation rich westerlies). Strong

[246] removed: . Note however
[247] removed: surface freshwater flux improves because of better represented
[248] removed: sea-ice
[249] removed: with
[250] removed: component, and by
[251] removed: simulation
[252] removed: reduces
[253] removed: while none
[254] removed: As for
[255] removed: being

convection and large Weddell Sea polynyas, as implied by the perpetual large regions of excessively deep mixed layers (Fig. 11), should thus be viewed as an unrealistic behaviour.

As suggested by Timmermann and Beckmann (2004), the vertical mixing scheme affects the sensitivity of spurious deep convection in the Weddell Sea. According to Kjellsson et al. (2015) and Timmermann and Beckmann (2004), sufficient vertical mixing is required in the top 100 m of the mixed layer in the Weddell Sea to prevent polynya formation. [..[256]]In our simulations, the wind induced mixing decreases quadratically with an [..[257]]increase in sea ice cover[..[258]], which may lead to deficient mixing under sea ice[..[259]], thus partly explaining the deep convection in the Weddell Sea[..[260]]. Although the KPP scheme reduces the mixed layer depths in the Ross Sea, it enhances deep convection in the central (HR_{kpp}) and [..[261]]eastern part of the Weddell Sea (XR_{kpp}). This enhanced deep convection [..[262]]contributes to the enhanced ACC strength [..[263]](Tab. 3), as it causes a steepening of the isopycnals across the ACC and thus an increased geostrophic flow (Jungclaus et al., 2013; Stössel et al., 2015; Naughten et al., 2018). This is another indication that the eddy activity is too low in the KPP simulations, so that isopycnals remain too steep and the water too weakly stratified.

Besides the resolution of the ocean component and the choice of the vertical ocean mixing scheme, a higher resolution of the atmosphere component has also a distinct effect on the simulated winter mixed layer depth (Fig. 11c versus 11a and Fig. 11d versus 11b), which is related to the reduced meridional pressure gradient (not shown) over the Weddell Sea. Stössel et al. (2015) found an improvement of the high-latitude Southern Ocean water-mass properties and winter [..[264]]sea ice cover in a simulation, where the high-resolution (TP6M) MPIOM was coupled to a T255 atmosphere (ECHAM6) compared to a coupled simulation with a TP6M ocean and T63 atmosphere. In terms of the ocean mixed layer depth, our results support these earlier findings, as also indicated by the reduction of the ACC to more realistic values (Tab. 3).

In all our model simulations shown here, [..[265]]sea ice salinity has a constant value of $5\,\mathrm{g\,kg^{-1}}$. As explained in Stössel et al. (2015), Vancoppenolle et al. (2009) and Hunke et al. (2011) argue for a [..[266]]sea ice salinity of about $8\,\mathrm{g\,kg^{-1}}$ for first-year ice, i.e. the kind of sea ice mostly found around Antarctica. Such a higher value would reduce the amount of brine release during ice formation, [..[267]]thus favoring a more stable upper-ocean water column in fall and winter. Another issue is the ice export from the coast: if too weak, it will strengthen open-ocean convection at the expense of near-boundary convection (e.g. Stössel et al., 2015; Haumann et al., 2016).

---

[256] removed: However, we chose to reduce

[257] removed: increased

[258] removed: (PP and KPP scheme) in MPI-ESM1.2, which might result in too less

[259] removed: and thus might also partly explain

[260] removed: in our simulations. We neglect here that wind induced mixing could increase with increasing sea ice concentration (and could be even larger than for open-ocean conditions), when the momentum flux from the atmosphere to the ocean will be taken over by the ice-ocean stress

[261] removed: in the

[262] removed: contribute

[263] removed: in the Drake Passage

[264] removed: sea-ice

[265] removed: sea-ice

[266] removed: sea-ice

[267] removed: and thus provide for

Another modelling challenge is the mixed layer depth in the Subantarctic Frontal zone equatorwards of the ACC (Rintoul and Trull, 2001). This is an important area for heat and CO_2 uptake and for the formation of the Subantarctic Mode Water. State-of-the-art ocean models simulate very shallow mixed layers between 40 to $60\,°S$ in comparison to Argo float observations (DuVivier et al., 2018). This discrepancy is in particular large in September, when the Argo floats show mixed layer depths of about 400 m (see Fig.2 in DuVivier et al. (2018)), even reaching depths of 700 m (Holte et al., 2017).

The main reason is that the ocean boundary layer in the models is not penetrating deep enough into the stratified subsurface ocean, where a high salinity maximum layer is observed between 150 to 200 m depth that originates from the Agulhas retroflection. This layer is modified in a complex way by Ekman pumping/suction. This subsurface salinity maximum builds up over spring and early summer and is mixed out in September. It is expected that the mixed layer depths increase by either increasing the horizontal resolution or by improving the vertical mixing parameterizations (DuVivier et al., 2018) allowing deeper penetrations of the ocean boundary layer into the subsurface salinity core.

Our reference simulation (HR_{pp}) simulates mixed layer depths of only about 200 to 300 m (Fig. A9a). Deeper mixed layers are simulated by either using the KPP scheme (HR_{kpp}; Fig. A9c) or by increasing the ocean resolution (ER_{pp}; Fig. A9e). Deeper mixed layers with an eddy-resolving ocean of $0.1°$ were also found in other eddy-resolving ocean models (Lee et al., 2011; Small et al., 2014; Li and Lee, 2017). However, the reason for improved mixed layer depth with high resolution is still unclear, and may be due to changes in circulation, local stratification or indirectly due to mixing (DuVivier et al., 2018). As already suspected by DuVivier et al. (2018), the nonlocal transport terms of the KPP scheme seem to favour deeper penetrations of the boundary layer into the salinity maximum layer, although this seems to happen in too wide a latitude band.

In ER_{pp}, the deep mixed layers are sharply confined to the observed latitudinal band between 40 to $60\,°S$. However, they appear to be too deep compared to the Argo float retrievals, for reasons that need to be further investigated. Nevertheless, the simulation of deeper mixed layers seems to be more realistic, which gives fidelity to our models with either an eddy-resolving ocean or using KPP.

4.6 Atlantic meridional overturning circulation

The large-scale global meridional overturning circulation (MOC) is an important carrier of heat and freshwater in the climate system. The Atlantic MOC (AMOC) is considered to be the strongest part of the MOC (Trenberth and Caron, 2001). The North Atlantic contributes about $25\,\%$ of the total poleward heat flux (ocean plus atmosphere) (Srokosz and Bryden, 2015; Lozier et al., 2017). The meridional transport of heat and salt follows the zonally integrated volume transport that, when facing west, emerges a clockwise rotating NADW cell and a counterclockwise rotating Antarctic Bottom Water (AABW) cell.

Fig. 12 shows the associated meridional overturning volume transport stream function, or AMOC, of all 5 simulations [..[268]]and Tab. 4 shows the time-mean AMOC strength at $26\,°N$ at $1000\,m$ depth, as well as the heat and salt transports across $50\,°N$. The time-mean of the AMOC is about $14.9\,Sv$ in HR_{pp} and comparable to the $16\,Sv$ of the MPI-ESM1.2-HR described

[268] removed: , while

by Müller et al. (2018). It is slightly lower than the observed mean value (± one standard deviation) of $17 \pm 4.4\,\mathrm{Sv}$ (Apr 2004 to Feb 2017) from the RAPID array (McCarthy et al., 2015; Smeed et al., 2017). $\mathrm{HR_{kpp}}$ simulates a stronger AMOC of $18.9\,\mathrm{Sv}$, which is the largest value of all our simulations. A possible explanation for this is given below. The volume transport of the overflow waters across the Greenland-Scotland ridge are also slightly higher with the KPP scheme (Tab. 3). After the overflow waters descend along the continental slopes and mix with ambient water masses, they contribute to a stronger NADW cell (Dickson and Brown, 1994) in the KPP simulations.

Figure 12f shows vertical profiles of the AMOC at $26.5\,°\mathrm{N}$ in comparison to the RAPID data. All simulations (except $\mathrm{XR_{pp}}$) produce transports close to the observations. The volume transport of $\mathrm{HR_{kpp}}$, however, is on the stronger side of the observations, whereas the transport of the other simulations are on the lower side of the observations. All models show a too strong southward transport of NADW below 2000 m, which suggests a too strong Deep Western Boundary Current.

The reduced wind stress from ECHAM6.3 at T255 results in the above mentioned slowdown of the AMOC in $\mathrm{XR_{pp}}$. In this simulation, the NADW cell reaches a maximum volume transport of only about $11.0\,\mathrm{Sv}$, which is slightly higher than the $9.0\,\mathrm{Sv}$ reported by [..[269]]Putrasahan et al. (2019). This discrepancy is because we analyze an earlier period of the same $\mathrm{XR_{pp}}$ simulation when the AMOC is still drifting to lower values. An important finding [..[270]]is that $\mathrm{XR_{kpp}}$ [..[271]]simulates a stable AMOC ($14.6\,\mathrm{Sv}$[..[272]]), despite the weak wind stress with the T255 atmosphere. In terms of volume transport, going to an eddy resolving ocean resolution ($\mathrm{ER_{pp}}$) does not increase the strength of the NADW [..[273]]cell. This finding is opposite to what Hewitt et al. (2016) and Storkey et al. (2018) found.

However, [..[274]]the bottom (AABW) cell becomes stronger (Fig. 12e), which [..[275]]may be due to similar effects as described by Sein et al. (2018), who hypothesize that eddy-induced transport acts to flatten the outcropping isopycnals in the Southern Ocean. So eddies counteract a wind-induced steepening of isopycnals, while at the same time, a stronger vertical gradient between the AABW and the warmer ambient ocean is maintained. The flatter isopycnals reduce the vertical mixing because of a more stratified water column, as indicated by the reduced mixed layer depths in the Weddell Sea in ER (Fig. 11e). Reduced convection maintains denser AABW, seen by sharper gradients of temperature and salinity in ER (Fig. [..[276]]A4e) and it theoretically helps to build up a deep heat reservoir (Dufour et al., 2017) that is required for intermittent Weddell Sea polynyas. However, in our ER simulation, Weddell Sea polynyas still form too frequently. On the other hand, better resolved bathymetry [..[277]]is important for the [..[278]]formation of AABW over the continental shelves, which is partly resolved in ER.

We define the depth of the NADW cell as the depth where the volume transport crosses the zero line in Fig. 12f. The observed annual mean depth (± one standard deviation) of the NADW cell (Tab. 4) from the RAPID data is about $4379 \pm 279\,\mathrm{m}$ at

[269]removed: Putrasahan et al. (2018)
[270]removed: of this study
[271]removed: , featuring reduced surface winds, results in a similarly strong AMOC of
[272]removed: as in $\mathrm{HR_{pp}}$ and $\mathrm{ER_{pp}}$
[273]removed:)
[274]removed: its
[275]removed: might be because of
[276]removed: A3
[277]removed: might also be
[278]removed: AABW formation

26.5 °N. All our simulations reveal shallower NADW cells of around 3000 m, but with a noticeable tendency to become deeper with the KPP scheme. A stronger AMOC deepens the NADW cell (Marshall et al., 2017), because more NADW is formed by overturning. This is consistent with the mixed layers [..[279]]being deeper in the KPP simulations, and with the increased overflow water from the GIN seas (Tab. 3).

In XR_{pp} the NADW cell is shallower (2665 m), consistent with a much weaker NADW cell. ER_{pp} simulates a slightly deeper (2941 m) NADW cell than HR_{pp}, probably because of increased overflow water from the GIN seas (Tab. 3), but still not as deep as in the simulations with the KPP scheme. The higher volume transport [..[280]]by the AMOC in the simulations with KPP yields a slightly enhanced heat transport and a considerably higher salt transport across 50 °N (Tab. 4, Fig. A1). This larger salt input into the subpolar North Atlantic with KPP is a main reason why the overturning becomes stronger, and in particular why XR_{kpp} maintains a stable AMOC, even [..[281]]with reduced wind stress.

The stronger deep convection in the northern North Atlantic (Labrador and Irminger Sea) and in the Nordic Seas enhance the local NADW formation that deepens the NADW cell. Note, however, that open-ocean deep convection is not directly associated with a net vertical mass transport [..[282]](Marotzke and Scott, 1999; Katsman et al., 2018) and thus the location of convective mixing and of strongest downward mass transfer need not coincide.

The surplus of NADW water has to be replaced by water masses from the NAC, leading to larger volume and salt transports of this current. Once the upper cell in the Atlantic becomes stronger, a positive feedback sets in. A stronger NAC strengthens the cyclonic circulation of the subpolar gyre (Tab. 2) and the separation of water masses in the gyre centres (Labrador/Irminger Sea) from the ambient water masses. This separation of water masses in the gyre centres enhances deep convection because of (1) increased isopycnal doming that leads to a weaker stratification of the water column and to a shallower thermocline, and (2) because of reduced mixing with ambient water, so that the water masses in the gyre centre are exposed longer to the overlaying cold atmosphere, leading to [..[283]]increased heat loss. Both effects reduce the surface stratification [..[284]]and its resistance to erosion, favouring deep convection that again strengthens the overturning cell. In addition, increased salt input densifies the upper water masses of the northern North Atlantic and the Nordic Seas, so that convection is enhanced.

As a result of the enhanced AMOC, the adiabatic upwelling branch of the MOC south of the ACC has to become stronger too (Fig. [..[285]]A4). Since [..[286]]we use the same background diffusivities below the mixed layer [..[287]]in KPP as with PP, no significant differences in diapycnal diffusion occur in the Pacific (not shown). That is, the only return pathway that might be modified by KPP is via wind-driven adiabatic upwelling in the Southern Ocean (Marshall and Speer, 2012). Indeed, the upwelling in the Pacific sector of the Southern Ocean increases with KPP (Fig. A4). An increase in upwelling in the Southern Ocean further strengthens the northern cell (Marshall et al., 2017). This feedback is however acting on longer time

[279] removed: beeing
[280] removed: of the AMOC with the KPP scheme
[281] removed: under reduced wind forcing
[282] removed: (Marotzke and Scott, 1999)
[283] removed: an
[284] removed: that could be easily eroded, which favours deep convection and
[285] removed: A2
[286] removed: KPP uses
[287] removed: as with the PPscheme, no significantly different diapycnal diffusion occurs

scales than the slowdown of the AMOC in our model. Therefore, the Southern Ocean is not the main factor in sustaining a stable AMOC in XR_{kpp}.

5 Summary

We compared control simulations of various MPI-ESM1.2 configurations following the HighResMIP protocol and investigated separately the resolution effects of the atmosphere and ocean model configurations and the effects of an alternative diapycnal ocean mixing scheme on the mean [..[288]]state of the atmosphere and ocean.

5.1 Eddy-resolving ocean

An eddy-resolving ocean reduces biases in the ocean mean-state and it has a major impact on the large-scale temperature distribution in the atmosphere. [..[289]]Cold temperature biases in the Southern Hemisphere, and to a lesser extent in the Northern Hemisphere, are reduced. The latter bias could not be removed by just increasing the atmospheric resolution. In the ocean, warm and saline [..[290]]biases in the Southern Atlantic were removed, because of the better representation of the Agulhas Current system (Putrasahan et al., 2015; Cheng et al., 2016) and because of eddy-induced upward transport of fresh and cold water masses, as described in von Storch et al. (2016). In general, swifter and narrower boundary currents are simulated in all basins with an eddy-resolving resolution. In the North Atlantic, the warm and saline bias was removed because of a better simulation of the water properties of the outflowing Mediterranean Water. An eddy-resolving ocean improves the separation of the Gulf Stream, although the NAC remained still too zonal in our simulation. Furthermore, the warm bias of the Atlantic Layer in the Arctic Ocean was removed, probably because of reduced numerical mixing due to the higher resolution, which confirms the results of Wang et al. (2018). [..[291]]In addition, the deep-convection centre shifted to the southeast in the Labrador Sea, and to the east in the Weddell Sea. An eddy-resolving resolution was also found to improve the mixed layer depths in the Subantarctic Frontal zone in the Indian, Australian and Pacific sectors of the Southern Ocean.

5.2 A T255 resolution for the atmosphere

[..[292]]The T255 atmosphere [..[293]]reduced mainly the wind stress over the ocean in both hemispheres, in particular in the Labrador Sea and in the Weddell Sea. In the [..[294]]latter, a reduced meridional pressure gradient in the atmosphere reduces the ACC transport [..[295]]to realistic values, as also reported by Stössel et al. (2015)[..[296]]. With the eddy-resolving

[288]removed: states

[289]removed: In the atmosphere, the cold biases above the Northern hemisphere were removed, but in particular the cold bias above the ACC

[290]removed: bias

[291]removed: Finally

[292]removed: A main improvement with a

[293]removed: are reduced mixed layer depths

[294]removed: Weddell Sea,

[295]removed: reduces

[296]removed: , because of a reduced meridional pressure gradient in the atmosphere across the ACC. Further the reduced pressure gradient above the Weddell Sea reduces the wind forcing of the Weddell Sea polynya. As with an

ocean (ER_{pp}), the centre of deep convection in the Weddell Sea shifts to the east, to the vicinity of the Maud Rise Plateau. In the northern hemisphere, [..[297]]however, the T255 atmosphere reduces the near-surface wind speeds over the subpolar gyre[..[298]], so that the subpolar gyre slows down and because of less cyclonic movement and less salt advection into the gyre centres, the deep convection [..[299]]diminishes (KPP scheme) or [..[300]]vanishes (PP scheme)[..[301]], as described by [..[302]]Putrasahan et al. (2019). In contrast to the near-surface, the jet streams[..[303]], however, are stronger in the T255 atmosphere.

5.3 Effects of the KPP scheme

The main effects of the KPP scheme are stronger deep convection in both hemispheres, [..[304]]reflected by deeper mixed layers. Under convective forcing the non-local fluxes of the KPP scheme produce much higher diffusivities compared [..[305]]to the enhanced diffusivity parameterization that we use for the PP scheme. This stronger deep convection with the KPP scheme produces more [..[306]]NADW locally in the convection centres (Labrador, Irminger, and GIN Seas) which in turn strengthens the AMOC. When coupled with the T255 atmosphere, the AMOC remains stable with the KPP scheme because of this enhanced overturning, which produces sufficient NADW to maintain a strong enough upper cell. Another effect [..[307]]that produces deeper mixed layers is a stronger subpolar gyre that domes the isopycnals and helps to precondition the water column for convection. This is also true for the Weddell Gyre with the same effect. We further found deeper mixed layers in the Subantarctic Frontal zones, which are important for the uptake of heat and CO_2. The stronger AMOC transports more salt and heat into the North Atlantic, so that the cold bias in the northern hemisphere is removed[..[308]].

Code and data availability. The MPI-ESM1.2 model code is made available under a version of the MPI-M Software License Agreement (http://www.mpimet.mpg.de/en/science/models/license; branch *mpiesm-1.2.01-cvmix* for the KPP simulations and *mpiesm-1.2.01-primavera_PP* for the PP simulations). Primary data and scripts used in the analysis, and other supplementary information that may be useful in reproducing the author's work, are archived by the Max Planck Institute for Meteorology and can be obtained by contacting publications@mpimet.mpg.de.

[297] removed: a
[298] removed: . With a reduced wind forcing,
[299] removed: reduces
[300] removed: completely ceases
[301] removed: with a slowdown of the AMOC
[302] removed: Putrasahan et al. (2018)
[303] removed: became stronger with a
[304] removed: as seen by the mixed layer depths
[305] removed: with
[306] removed: local NADW
[307] removed: of producing deeper mixed layer
[308] removed: (except in the upper troposphere)

Author contributions. JJ and JS designed the experiments and DP and KL set up the model configurations and performed the simulations. OG, NB and HH have implemented the new mixing parameterizations in MPIOM. OG prepared the manuscript with contributions from all co-authors.

Competing interests. The authors declare that they have no conflict of interest.

Acknowledgements. We thank the German Computing Centre (DKRZ) for providing the computing resources. This research was funded by the EU Horizon 2020 project PRIMAVERA (grant number 641727). This paper is a contribution to the project S2 (Improved parameterisations and numerics in climate models) of the Collaborative Research Centre TRR 181 "Energy Transfer in Atmosphere and Ocean" funded by the Deutsche Forschungsgemeinschaft (DFG, German Research Foundation) - project number 274762653. JJ acknowledges support by the German BMBF RACE-II project (FKZ 03F0729D). AS acknowledges support through a Max-Planck-Society research stipend. We thank Jürgen Kröger for proofreading the manuscript. The OSI SAF data of EUMETSAT were made available from http://osisaf.met.no. Finally, we thank two anonymous reviewers for their constructive and helpful comments.

References

Adcroft, A. J., Hill, C., and Marshall, J.: Representation of Topography by Shaved Cells in a Height Coordinate Ocean Model, Mon. Weather Rev., 125, 2293–2315, https://doi.org/10.1175/1520-0493(1997)125<2293:ROTBSC>2.0.CO;2, 1997.

Bacon, S.: Circulation and Fluxes in the North Atlantic between Greenland and Ireland, J. Phys. Oceanogr., 27, 1420–1435, https://doi.org/10.1175/1520-0485(1997)027<1420:CAFITN>2.0.CO;2, 1997.

Bersch, M.: On the circulation of the northeastern North Atlantic, Deep-Sea Res. Pt. I, 42, 1583–1607, https://doi.org/10.1016/0967-0637(95)00071-D, 1995.

Bryden, H. L., Candela, J., and Kinder, T. H.: Exchange through the Strait of Gibraltar, Prog. Oceanog., 33, 201–248, https://doi.org/10.1016/0079-6611(94)90028-0, 1994.

Cheng, Y., Putrasahan, D., Beal, L., and Kirtman, B.: Quantifying Agulhas Leakage in a High-Resolution Climate Model, J. Climate, 29, 6881–6892, https://doi.org/10.1175/JCLI-D-15-0568.1, 2016.

Cheng, Y., Beal, L. M., Kirtman, B. P., and Putrasahan, D.: Interannual Agulhas Leakage Variability and its Regional Climate Imprints, J. Climate, 31, 10 105–10 121, https://doi.org/10.1175/JCLI-D-17-0647.1, 2018.

Clark, R. A.: Transport through the Cape Farewell-Flemish Cap section, Rapp. P. V. Reun. Cons. Int. Explor. Mer., 185, 120–130, 1984.

Cunningham, S. A., Alderson, S. G., King, B. A., and Brandon, M. A.: Transport and variability of the Antarctic circumpolar current in Drake Passage, J. Geophys. Res., 108 (C5), 8084, https://doi.org/10.1029/2001JC001147, 2003.

de Lavergne, C., Palter, J. B., Galbraith, E. D., Bernardello, R., and Marinov, I.: Cessation of deep convection in the open Southern Ocean under anthropogenic climate change, Climate Change, 4, 278–282, https://doi.org/10.1038/nclimate2132, 2014.

Dee, D. P., Uppala, S. M., Simmons, A. J., Berrisford, P., Poli, P., Kobayashi, S., Andrae, U., Balmaseda, M. A., Balsamo, G., Bauer, P., Bechtold, P., Beljaars, A. C. M., van de Berg, L., Bidlot, J., Bormann, N., Delsol, C., Dragani, R., Fuentes, M., Geer, A. J., Haimberger, L., Healy, S. B., Hersbach, H., Hólm, E. V., Isaksen, L., Kåberg, P., Köhler, M., Matricardi, M., McNally, A. P., Monge-Sanz, B. M., Morcrette, J.-J., Park, B.-K., Peubey, C., de Rosnay, P., Tavolato, C., Thépaut, J.-N., and Vitart, F.: The ERA-Interim reanalysis: configuration and performance of the data assimilation system, Q. J. R. Meteorol. Soc., 137, 553–597, https://doi.org/10.1002/qj.828, 2011.

Dengg, J. A., Beckmann, A., and Gerdes, R.: The Warmwatersphere of the North Atlantic Ocean, chap. The Gulf Stream separation problem, pp. 253–290, Gebr. Bornträger, Berlin, 1996.

Dickson, R. R. and Brown, J.: The production of North Atlantic Deep Water: Sources, rates, and pathways, J. Geophys. Res., 99, 12 319–12 341, https://doi.org/10.1029/94JC00530, 1994.

DiMarco, S. F., Chapman, P., Nowlin Jr., W. D., Hacker, P., Donohue, K., Luther, M., Johnson, G. C., and Toole, J.: Volume transport and property distribution of the Mozambique Channel, Deep-Sea Res. II, 49, 1481–1511, https://doi.org/10.1016/S0967-0645(01)00159-X, 2002.

Donohue, K. A., Tracey, K. L., Watts, D. R., Chidichimo, M. P., and Chereskin, T. K.: Mean Antarctic Circumpolar Current transport measured in Drake Passage, Geophys. Res. Lett., 43, 11 760–11 767, https://doi.org/10.1002/2016GL070319, 2016.

Drews, A., Greatbatch, R. J., Ding, H., Latif, M., and Park, W.: The use of a flow field correction technique for alleviating the North Atlantic cold bias with application to the Kiel Climate Model, Ocean Dyn., 65(8), 1079–1093, https://doi.org/10.1007/s10236-015-0853-7, 2015.

Dufour, C. O., Morrison, A. K., Griffies, S. M., Frenger, I., Zanowski, H., and Winton, M.: Preconditioning of the Weddell Sea Polynya by the Ocean Mesoscale and Dense Water Overflows, J. Climate, 30, 7719–7737, https://doi.org/10.1175/JCLI-D-16-0586.1, 2017.

DuVivier, A. K. and Cassano, J. J.: Comparison of wintertime mesoscale winds over the ocean around southeastern Greenland in WRF and ERA-Interim, Clim. Dynam., 46, 2197–2211, https://doi.org/10.1007/s00382-015-2697-8, 2016.

DuVivier, A. K., Large, W. G., and Small, R. J.: Argo observations of the deep mixing band in the Southern Ocean: A salinity modeling challenge., J. Geophys. Res. Oceans, 123, 7599–7617, https://doi.org/10.1029/2018JC014275, 2018.

Eden, C. and Böning, C.: Sources of Eddy Kinetic Energy in the Labrador Sea, J. Phys. Oceanogr., 32, 3346–3363, https://doi.org/10.1175/1520-0485(2002)032<3346:SOEKEI>2.0.CO;2, 2002.

EUMETSAT Ocean and Sea Ice Satellite Application: Global sea ice concentration reprocessing dataset 1978-2015 (v1.2, 2015), [Online], http://osisaf.met.no, Norwegian and Danish Meteorological Institutes, 2015.

Eyring, V., Bony, S., Meehl, G. A., Senior, C. A., Stevens, B., Stouffer, R. J., and Taylor, K. E.: Overview of the Coupled Model Intercomparison Project Phase 6 (CMIP6) experimental design and organization, Geoscientific Model Development, 9, 1937–1958, https://doi.org/10.5194/gmd-9-1937-2016, 2016.

Fan, X., Send, U., Testor, P., Karstensen, J., and Lherminier, P.: Observations of Irminger Sea Anticyclonic Eddies, J. Phys. Oceanogr., 43, 805–823, https://doi.org/10.1175/JPO-D-11-0155.1, 2013.

Fieg, K., Gerdes, R., Fahrbach, E., Beszczynska-Möller, A., and Schauer, U.: Simulation of oceanic volume transports through Fram Strait 1995–2005, Ocean Dyn., 60, 491–502, https://doi.org/10.1007/s10236-010-0263-9, 2010.

Frenger, I., Gruber, R., Knutti, R., and Münnich, M.: Imprint of Southern Ocean eddies on winds, clouds and rainfall, Nat. Geosci., 6, 608–612, https://doi.org/10.1038/ngeo1863, 2013.

Gent, P. R.: A commentary on the Atlantic meridional overturning circulation stability in climate models, Ocean Model., 122, 57–66, https://doi.org/10.1016/j.ocemod.2017.12.006, 2018.

Gent, P. R., Willebrand, J., McDougall, T. J., and McWilliams, J. C.: Parameterizing Eddy-Induced Tracer Transports in Ocean Circulation Models, J. Phys. Oceanogr., 25, 463–474, https://doi.org/10.1175/1520-0485(1995)025<0463:PEITTI>2.0.CO;2, 1995.

Giorgetta, M. A., Jungclaus, J., Reick, C. H., Legutke, S., Bader, J., Böttinger, M., Brovkin, V., Crueger, T., Esch, M., Fieg, K., Glushak, K., Gayler, V., Haak, H., Hollweg, H.-D., Ilyina, T., Kinne, S., Kornblueh, L., Matei, D., Mauritsen, T., Mikolajewicz, U., Mueller, W., Notz, D., Pithan, F., Raddatz, T., Rast, S., Redler, R., Roeckner, E., Schmidt, H., Schnur, R., Segschneider, J., Six, K. D., Stockhause, M., Timmreck, C., Wegner, J., Widmann, H., Wieners, K.-H., Claussen, M., Marotzke, J., and Stevens, B.: Climate and carbon cycle changes from 1850 to 2100 in MPI-ESM simulations for the Coupled Model Intercomparison Project phase 5, J. Adv. Model. Earth Syst., 5, 572–597, https://doi.org/10.1002/jame.20038, 2013.

Good, S. A., Martin, M. J., and Rayner, N. A.: EN4: quality controlled ocean temperature and salinity profiles and monthly objective analyses with uncertainty estimates, J. Geophys. Res., 118, 6704–6716, https://doi.org/10.1002/2013JC009067, 2013.

Gordon, A. L.: Southern Ocean polynya, Nature Clim. Change, 4, 249–250, https://doi.org/10.1038/nclimate2179, 2014.

Gordon, A. L., Sprinthall, J., Van Aken, H. M., Susanto, D., Wijffels, S., Molcard, R., Field, A., Pranowo, W., and Wirasantosa, S.: The Indonesian throughflow during 2004–2006 as observed by the INSTANT program, Dyn. Atmos. Oceans, 50, 115–128, https://doi.org/10.1016/j.dynatnoce.2009.12.002., 2010.

Griffies, S. M., Levy, M., Adcroft, A. J., Danabasoglu, R., Hallberg, R. W., Jacobsen, D., Large, W., and Ringler, T. D.: Theory and numerics of the Community Ocean Vertical Mixing (CVMix) Project, Tech. rep., https://github.com/CVMix/CVMix-description, 2013.

Griffies, S. M. et al.: Coordinated ocean-ice reference experiments (COREs), Ocean Model., 26, 1–46, https://doi.org/10.1016/j.ocemod.2008.08.007, 2009.

Gutjahr, O. and Heinemann, G.: A model-based comparison of extreme winds in the Arctic and around Greenland, Int. J. Climatol., 38, 5272–5292, https://doi.org/10.1002/joc.5729, 2018.

Haarsma, R. J., Roberts, M. J., Vidale, P. L., Senior, C. A., Bellucci, A., Bao, Q., Chang, P., Corti, S., Fučkar, N. S., Guemas, V., von Hardenberg, J., Hazeleger, W., Kodama, C., Koenigk, T., Leung, L. R., Lu, J., Luo, J.-J., Mao, J., Mizielinski, M. S., Mizuta, R., Nobre, P., Satoh, M., Scoccimarro, E., Semmler, T., Small, J., and von Storch, J.-S.: High Resolution Model Intercomparison Project (HighResMIP v1.0) for CMIP6, Geosci. Model Dev., 9, 4185–4208, https://doi.org/10.5194/gmd-9-4185-2016, 2016.

Hagemann, S. and Gates, L. D.: Improving a subgrid runoff parameterization scheme for climae models by the use of a high resolution data derived from satellite observations, Climate Dyn., 21, 349–359, https://doi.org/10.1007/s00382-003-0349-x, 2003.

Hansen, B., Østerhus, S., Turrell, W. R., Jónsson, S., Valdimarsson, H., Hátún, H., and Olsen, S. M.: The Inflow of Atlantic Water, Heat, and Salt to the Nordic Seas Across the Greenland–Scotland Ridge, pp. 15–43, Springer Netherlands, Dordrecht, https://doi.org/10.1007/978-1-4020-6774-7_2, 2008.

Haumann, F. A., Gruber, N., Münnich, M., Frenger, I., and Kern, S.: Sea-ice transport driving Southern Ocean salinity and its recent trends, Nature, 537(7618), 89–92, https://doi.org/10.1038/nature19101, 2016.

Hertwig, E., von Storch, J.-S., Handorf, D., Dethloff, K., Fast, I., and Krismer, T.: Effect of horizontal resolution on ECHAM6-AMIP performance, Clim. Dyn., 45, 185–211, https://doi.org/10.1007/s00382-014-2396-x, 2015.

Heuzé, C., Ridley, J. K., Calvert, D., Stevens, D. P., and Heywood, K. J.: Increasing vertical mixing to reduce Southern Ocean deep convection in NEMO3.4, Geoscientific Model Development, 8, 3119–3130, https://doi.org/10.5194/gmd-8-3119-2015, 2015.

Hewitt, H. T., Roberts, M. J., Hyder, P., Graham, T., Rae, J., Belcher, S. E., et al.: The impact of resolving the Rossby radius at mid-latitudes in the ocean: Results from a high-resolution version of the Met Office GC2 coupled model, Geosci. Model Dev., 9, 3655–3670, https://doi.org/10.5194/gmd-9-3655-2016, 2016.

Holliday, N. P., Bacon, S., Allen, J., and McDonagh, E. L.: Circulation and transport in the western boundary currents at Cape Farewell, Greenland., J. Phys. Oceanogr., 39 (8), 1854–1870, https://doi.org/10.1175/2009JPO4160.1, 2009.

Holloway, G., Dupont, F., Golubeva, E., Haekkinen, S., Hunke, E., Jin, M., Karcher, M., Kauker, F., Maltrud, M., Maqueda, M. A. M., Maslowski, W., Platov, G., Stark, D., Steele, M., Suzuki, T., Wang, J., and Zhang, J.: Water properties and circulation in Arctic Ocean models, Geophys. Res. Oceans, 112, C04S03, https://doi.org/10.1029/2006JC003642, 2007.

Holte, J., Talley, L. D., Gilson, J., and Roemmich, D.: An Argo mixed layer climatology and database, Geophys. Res. Lett., 44, 5618–5626, https://doi.org/10.1002/2017GL073426, 2017.

Hunke, E. C., Notz, D., Turnker, A. K., and Vancoppenolle, M.: The multiphase physics of sea ice: a review for model developers, Cryosphere, 27, 3784–3801, https://doi.org/10.5194/tc-5-989-2011, 2011.

Ilicak, M., Drange, H., Wang, Q., et al.: An assessment of the Arctic Ocean in a suite of interannual CORE-II simulations. Part III: Hydrography and fluxes, Ocean Model., 100, 141–161, https://doi.org/10.1016/j.ocemod.2016.02.004, 2016.

Imawaki, S., Uchida, H., Ichikawa, H., Fukasawa, M., Umatani, S., and ASUKA Group: Satellite altimeter monitoring the Kuroshio Transport south of Japan, Geophys. Res. Lett., 28, 17–20, https://doi.org/10.1029/2000GL011796, 2001.

Jochumsen, K., Quadfasel, D., Valdimarsson, H., and Jónsson, S.: Variability of the Denmark Strait overflow: Moored time series from 1996–2011, J. Geophys. Res., 117, C12 003, https://doi.org/10.1029/2012JC008244, 2012.

Jochumsen, K., Moritz, M., Nunes, N., Quadfasel, D., Larsen, K. M. H., Hansen, B., Valdimarsson, H., and Jonsson, S.: Revised transport estimates of the Denmark Strait overflow, J. Geophys. Res., 122, 3434–3450, 2017.

Johns, W., Shay, T., Bane, J., and Watts, D.: Gulf Stream structure, transport, and recirculation near 68 ° W, J. Geophys. Res., 100, 817–838, https://doi.org/10.1029/94JC02497, 1995.

Jungclaus, J. H., Fischer, N., Haak, H., Lohmann, K., Marotzke, J., Matei, D., Mikolajewicz, U., Notz, D., and von Storch, J. S.: Characteristics of the ocean simulations in the Max Planck Institute Ocean Model (MPIOM), the ocean component of the MPI-Earth system model, J. Adv. Model. Earth Syst., 5, 422–446, https://doi.org/10.1002/jae.20023, 2013.

Kanzow, T. and Zenk, W.: Structure and transport of the Iceland Scotland Overflow plume along the Reykjanes Ridge in the Iceland Basin, Deep-Sea Res. Pt. I, 86, 82–93, https://doi.org/10.1016/j.dsr.2013.11.003, 2014.

Kanzow, T., Cunningham, S. A., Johns, W. E., Hirschi, J. J.-M., Marotzke, J., Baringer, M. O., Meinen, C. S., Chidichimo, M. P., Atkinson, C., Beal, L. M., Bryden, H. L., and Collins, J.: Seasonal variability of the Atlantic meridional overturning circulation at 26.5 ° N, J. Climate, 23, 5678–5698, https://doi.org/10.1175/2010JCLI3389.1, 2010.

Katsman, C. A., Drijfhout, S. S., Dijkstra, H. A., and Spall, M. A.: Sinking of Dense North Atlantic Waters in a Global Ocean Model: Location and Controls, J. Geophys Res. Oceans, 123, 3563–3576, https://doi.org/10.1029/2017JC013329, 2018.

Kawasaki, T. and Hasumi, H.: Effect of freshwater from the West Greenland Current on the winter deep convection in the Labrador Sea, Ocean Modell., 75, 51–64, https://doi.org/10.1016/j.ocemod.2014.01.003, 2014.

Kjellsson, J., Holland, P. R., Marshall, G. J., Mathiot, P., Aksenov, Y., Coward, A. C., Bacon, S., Megann, A. P., and Ridley, J.: Model sensitivity of the Weddell and Ross seas, Antarctica, to vertical mixing and freshwater forcing, Ocean Modelling, 94, 141–152, https://doi.org/10.1016/j.ocemod.2015.08.003, 2015.

Kurtakoti, P., Veneziani, M., Stössel, A., and Weijer, W.: Preconditioning and Formation of Maud Rise Polynyas in a High-Resolution Earth System Model, J. Climate, https://doi.org/10.1175/JCLI-D-18-0392.1, 2018.

Large, W. G., McWilliams, J. C., and Doney, S. C.: Oceanic vertical mixing: A review and a model with a nonlocal boundary layer parameterization, Rev. Geophys., 21, 363–403, https://doi.org/10.1029/94RG01872, 1994.

Lee, M.-M., Nurser, A. J. G., Stevens, I., and Salée, J.-B.: Subduction over the Southern Indian Ocean in a high-resolution atmosphere-ocean coupled model., J. Clim., 24, 3830–3849, https://doi.org/10.1175/2011JCLI3888.1, 2011.

Lherminier, P., Mercier, H., Gourcuff, C., Alvarez, M., Bacon, S., and Kermabon, C.: Transports across the 2002 Greenland-Portugal Ovide section and comparison with 1997, J. Geophys. Res., 112, C07 003, https://doi.org/10.1029/2006JC003716, 2007.

Li, Q. and Lee, S.: A mechanism of mixed-layer formation in the Indo-western Pacific Southern Ocean: Preconditioning by an eddydriven jet-scale overturning circulation, J. Phys. Oceanogr., 47, 2775–2772, https://doi.org/10.1175/JPO-D-17-0006.1, 2017.

Liu, X., Chang, P., Kurian, J., Saravan, R., and Lin, X.: Satellite-Observed Precipitation Response to Ocean Mesoscale Eddies, J. Climate, 31, 6879–6895, https://doi.org/10.1175/JCLI-D-17-0668.1, 2018.

Lozier, M. S. et al.: Overturning in the Subpolar North Atlantic Program: A new international ocean observing system, Bull. Am. Meteorol. Soc., 98, 43–63, https://doi.org/10.1175/BAMS-D-16-0057.1, 2017.

Ma, X., Jing, Z., Chang, P., Liu, X., Montuoro, R., Small, J. R., Bryan, F. O., Greatbatch, R. J., Brandt, P., Wu, D., Lin, X., and Wu, L.: Western boundary currents regulated by the interaction between ocean eddies and the atmosphere, Nature, 535, 533–537, https://doi.org/10.1038/nature18640, 2016.

Marotzke, J. and Scott, J. R.: Convective Mixing and the Thermohaline Circulation, J. Phys. Oceanogr., 29, 2962–2970, https://doi.org/10.1175/1520-0485(1999)029<2962:CMATTC>2.0.CO;2, 1999.

Marshall, J. and Speer, K.: Closure of the meridional overturning circulation through Southern Ocean upwelling, Nat. Geosci., 5 (3), 171–180, https://doi.org/10.1038/ngeo1391, 2012.

Marshall, J., Scott, J. R., Romanou, A., Kelley, M., and Leboissetier, A.: The dependence of the ocean's MOC on mesoscale eddy diffusivities: A model study, Ocean Model., 111, 1–8, 2017.

Marsland, S. J., Haak, H., Jungclaus, J. H., Latif, M., and Röske, F.: The Max Planck Institute global ocean/sea ice model with orthogonal curvilinear coordinates, Ocean Model., 5, 91–127, 2003.

Martin, R. and Moore, G. W. K.: Air-sea interaction associated with a Greenland reverse tip jet, Geophys. Res. Lett., 34, L24 802, https://doi.org/10.1029/2007GL031093, 2007.

Mauritsen, T., Stevens, B., Roeckner, E., Crueger, T., Esch, M., Giorgetta, M., Haak, H., Jungclaus, J. H., Klocke, D., Matei, D., Mikolajewicz, U., Notz, D., Pincus, R., Schmidt, H., and Tomassini, L.: Tuning the climate of a global model, J. Adv. Model. Earth Syst., 4(3), M00A01, https://doi.org/10.1029/2012MS000154, 2012.

Mauritsen, T. et al.: Developments in the MPI-M Earth System Model version 1.2 (MPI-ESM1.2) and its response to increasing $CO2$, J. Adv. Model. Earth Syst., https://doi.org/10.1029/2018MS001400, 2018.

McCarthy, G. D., Smeed, D. A., Johns, W. E., Frajka-Williams, E., Moat, B. I., Rayner, D., Baringer, M. O., Meinen, C. S., Collins, J., and Bryden, H. L.: Measuring the Atlantic Meridional Circulation at 26°N, Prog. in Ocean., 130, 91–111, https://doi.org/10.1016/j.pocean.2014.10.006, 2015.

McClean, J. L., Bader, D. C., Bryan, F. O., Maltrud, M. E., Dennis, J. M., Mirin, A. A., Jones, P. W., Kim, Y. Y., Ivanova, D. P., Vertenstein, M., Boyle, J. S., Jacob, R. L., Norton, N., Craig, A., and Worley, P. H.: A prototype two-decade fully-coupled fine-resolution CCSM simulation, Ocean Model., 39, 10–30, https://doi.org/10.1016/j.ocemod.2011.02.011, 2011.

McDonagh, E. L., King, B. A., Bryden, H. L., Courtois, P., Szuts, Z., Baringer, M., Cunningham, S. A., Atkinson, C., and McCarthy, G.: Continuous estimate of Atlantic Oceanic freshwater flux at $26.5\,^\circ$ N, J. Climate, 28, 8888–8906, https://doi.org/10.1175/JCLI-D-14-00519.1, 2015.

Meredith, M. P., Woodworth, P. L., Chereskin, T. K., Marshall, D. P., Allison, L. C., Bigg, G. R., Donohue, K., Heywood, K. J., Hughes, C. W., Hibbert, A., Hogg, A. M., Johnson, H. L., Loïc, J., King, B. A., Leach, H., Lenn, Y.-D., Morales Maqueda, M. A., Munday, D. R., Naveira Garabato, A. C., Provost, C., Sallée, J.-B., and Sprintall, J.: Sustained monitoring of the Southern Ocean at Drake Passage: Past achievements and future priorities, Rev. Geophys., 49, RG4005, https://doi.org/10.1029/2010RG000348, 2011.

Milinski, S., Bader, J., Haak, H., Siongco, A. C., and Jungclaus, J. H.: High atmospheric horizontal resolution eliminates the wind-driven coastal warm bias in the southeastern tropical Atlantic, Geophys. Res. Lett., 43, 10 455–10 462, https://doi.org/10.1002/2016GL070530, 2016GL070530, 2016.

Müller, M., Haak, H., Jungclaus, J. H., Sündermann, J., and Thomas, M.: The effect of ocean tides on a climate model simulation, Ocean Model., 35, 304–313, 2010.

Müller, W. A., Jungclaus, J. H., Mauritsen, T., Baehr, J., Bittner, M., Budich, R., Bunzel, F., Esch, M., Ghosh, R., Haak, H., Ilyina, T., Kleine, T., Kornblueh, L., Li, H., Modali, K., Notz, D., Pohlmann, H., Roeckner, E., Stemmler, I., Tian, F., and Marotzke, J.: A higher-resolution version of the Max Planck Institute Earth System Model (MPI-ESM 1.2-HR), J. Adv. Model. Earth Syst., 10, 1383–1413, https://doi.org/10.1029/2017MS001217, 2018.

Naughten, K., Meissner, K. J., Galton-Fenzi, B. K., England, M. H., Timmermann, R., Hellmer, H. H., Hattermann, T., and Debernard, J. B.: Intercomparison of Antarctic ice-shelf, ocean, and sea-ice interactions simulated by MetROMS-iceshelf and FESOM 1.4, Geosci. Model. Dev., 11, 1257–1292, https://doi.org/10.5194/gmd-11-1257-2018, 2018.

Notz, D., Haumann, F. A., Haak, H., Jungclaus, J. H., and Marotzke, J.: Arctic sea-ice evolution as modeled by Max Planck Institute for Meteorology's Earth system model, J. Adv. Model. Earth Syst., 5, 173–194, https://doi.org/10.1002/jame.20016, 2013.

Nowlin Jr., W. D. and Klinck, J. M.: The physics of the Antarctic Circumpolar Current, Rev. Geophys., 24(3), 469–491, https://doi.org/10.1029/RG024i003p00469, 1986.

Pacanowski, R. C. and Philander, S. G. H.: Parameterization of Vertical Mixing in Numerical Models of Tropical Oceans, J. Phys. Oceanogr., 11, 1443–1451, https://doi.org/10.1175/1520-0485(1981)011<1443:POVMIN>2.0.CO;2, 1981.

Pickart, R. S., Spall, M. A., Ribergaard, M. H., Moore, G. W. K., and Milliff, R. F.: Deep convection in the Irminger Sea forced by the Greenland tip jet, Nature, 424, 152–156, https://doi.org/10.1038/nature01729, 2003.

Putrasahan, D., Kirtman, B. P., and Beal, L. M.: Modulation of SST Interannual Variability in the Agulhas Leakage Region Associated with ENSO, J. Climate, 29, 7089–7102, https://doi.org/10.1175/JCLI-D-15-0172.1, 2016.

Putrasahan, D. A., Miller, A. J., and Seo, H.: Regional coupled ocean–atmosphere downscaling in the Southeast Pacific: impacts on upwelling, mesoscale air–sea fluxes, and ocean eddies, Ocean Dyn., 63, 463–488, https://doi.org/10.1007/s10236-013-0608-2, 2013.

Putrasahan, D. A., Beal, L. M., Kirtman, B. P., and Cheng, Y.: A new Eulerian method to estimate “spicy” Agulhas leakage in climate models, J. Climate, 42, 4532–4539, https://doi.org/10.1002/2015GL064482, 2015.

Putrasahan, D. A., Lohmann, K., von Storch, J. S., Jungclaus, J. H., Haak, H., and Gutjahr, O.: Surface flux drivers for the slowdown of the Atlantic Meridional Overturning Circulation in a high-resolution global coupled climate model, J. Adv. Model. Earth Syst., in preparation, 2018.

Putrasahan, D. A., Lohmann, K., von Storch, J. S., Jungclaus, J. H., Haak, H., and Gutjahr, O.: Surface flux drivers for the slowdown of the Atlantic Meridional Overturning Circulation in a high-resolution global coupled climate model, J. Adv. Model. Earth Syst., 11, https://doi.org/10.1029/2018MS001447, 2019.

Randall, D. A., Wood, R. A., Bony, S., Colman, R., Fichefet, T., Fyfe, J., Kattsov, V., Pitman, A., Shukla, J., Srinivasan, J., Stouffer, R. J., Sumi, A., and Taylor, K. E.: Climate Change 2007: The Physical Science Basis. Contribution of Workung Group I to the Fourth Assessment Report of the Intergovernmental Panel on Climate Change, chap. Climate Models and Their Evaluation, Cambridge University Press, Cambrigdge, United Kingdom and New York, NY, USA, 2007.

Redi, M. H.: Oceanic Isopycnal Mixing by Coordinate Rotation, Journal of Physical Oceanography, 12, 1154–1158, https://doi.org/10.1175/1520-0485(1982)012<1154:OIMBCR>2.0.CO;2, 1982.

Reick, C., Raddatz, T., Brovkin, V., and Gayler, V.: Representatoin of natural and anthropogenic land cover changes in MPI-ESM, J. Adv. Model. Earth Syst., 5, 459–482, https://doi.org/10.1002/jame.20022, 2013.

Ridderinkhof, H., van der Werf, P. M., Ullgren, J. E., van Aken, H. M., van Leeuwen, P. J., and de Ruijter, P. M.: Seasonal and interannual variability in the Mozambique Channel from moored current observations, J. Geophys. Res., 115, C06 010, https://doi.org/10.1029/2009JC005619, 2010.

Rintoul, S. R. and Trull, T. W.: Seasonal evolution of the mixed layer in the Subantarctic zone south of Australia, J. Geophys Res., 106(C12), 31 447–31 462, https://doi.org/10.1029/2000JC000329, 2001.

Rossby, T. and Flagg, C.: Direct measurement of volume flux in the Faroe-Shetland Channel and over the Iceland-Faroe Ridge, Geophys. Res. Lett., 39, L07 602, https://doi.org/10.1029/2012GL051269, 2012.

Sallée, J.-B., Shuckburgh, E., Bruneau, N., Meijers, A. J. S., Bracegirdle, T. J., and Wang, Z.: Assessment of Southern Ocean mixed-layer depths in CMIP5 models: Historical bias and forcing response, J. Geophys. Res. Oceans, 118, 1845–1862, https://doi.org/10.1002/jgrc.20157, 2013.

Schweiger, A., Lindsay, R., Zhang, J., Steele, M., Stern, H., and Kwok, R.: Uncertainty in modelled Arctic sea ice volume, J. Geophys. Res. Oceans, 116, D06, https://doi.org/10.1029/2011JC007084, 2011.

Sein, D. V., Koldunov, N. V., Danilov, S., Sidorenko, D., Wekerle, C., Cabos, W., Rackow, T., Scholz, P., Semmler, T., Wang, Q., and Jung, T.: The relative influence of atmospheric and oceanic model resolution on the circulation of the North Atlantic Ocean in a coupled climate model, J. Adv. Model. Earth Syst., 10, 2026–2041, https://doi.org/10.1029/2018MS001327, 2018.

Small, R. J., Bacmeister, J., Bailey, D., Baker, A., Bishop, S., and Bryan, F.: A new synoptic scale resolving global climate simulation using the Community Earth System Model, J. Adv. Model. Earth Syst., 6, 1065–1094, https://doi.org/10.1002/2014MS000363, 2014.

Small, R. J., Curchitser, E., Hedstrom, K., Kauffmann, B., and Large, W. G.: The Benguela Upwelling System: Quantifying the Sensitivity to Resolution and Coastal Wind Representation in a Global Climate Model, J. Climate, 28, 9409–9432, https://doi.org/10.1175/JCLI-D-15-0192.1, 2015.

Smeed, D., McCarthy, G., Rayner, D., Moat, B. I., Johns, W. E., Baringer, M. O., and Meinen, C. S.: Atlantic meridional overturning circulation observed by the RAPID-MOCHA-WBTS (RAPID-Meridional Overturning Circulation and Heatflux Array-Western Boundary Time Series) array at 26N from 2004 to 2017. British Oceanographic Data Centre - Natural Environment Research Council, UK, https://doi.org/10.5285/5acfd143-1104-7b58-e053-6c86abc0d94b, 2017.

Soto-Navarro, J., Criado-Aldeanueva, F., García-Lafuente, J., and Sánchez-Román, A.: Estimation of the Atlantic inflow through the Strait of Gibraltar from climatological and in situ data, J. Geophys. Res., 115, C10 023, https://doi.org/10.1029/2010JC006302, 2010.

Srokosz, M. A. and Bryden, H. L.: Observing the Atlantic Meridional Overturning Circulation yields a decade of inevitable surprises, Science, 348(6241), 1255 575, https://doi.org/10.1126/science.1255575, 2015.

Stevens, B., Giorgetta, M., Esch, M., Mauritsen, T., Crueger, T., Rast, S., Salzmann, M., Schmidt, H., Bader, J., Block, K., Brokopf, R., Fast, I., Kinne, S., Kornblueh, L., Lohmann, U., Pincus, R., Reichler, T., and Roeckner, E.: Atmospheric component of the MPI-M Earth System Model: ECHAM6, J. Adv. Model. Earth Syst., 5, 146–172, https://doi.org/10.1002/jame.20015, 2013.

Storkey, D., Blaker, A. T., Mathiot, P., Megann, A., Aksenov, Y., Blockley, E. W., et al.: UK Global Ocean GO6 and GO7: A traceable hierarchy of model resolutions, Geosci. Model Dev, 11, 3187–3213, https://doi.org/10.5194/gmd.11-3187-2018, 2018.

Stössel, A., Notz, D., Haumann, F. A., Haak, H., Jungclaus, J., and Mikolajewicz, U.: Controlling high-latitude Southern Ocean convection in climate models, Ocean Model., 86, 58–75, https://doi.org/10.1016/j.ocemod.2014.11.008, 2015.

Stössel, A., von Storch, J., Notz, D., Haak, H., and Gerdes, R.: High-frequency and meso-scale winter sea-ice variability in the Southern Oscillation in a high resolution global ocean model, Ocean Dyn., https://doi.org/10.1007/s10236-018-1135-y, 2018.

Timmermann, R. and Beckmann, A.: Parameterization of vertical mixing in the Weddell Sea, Ocean Model., 6, 83–100, https://doi.org/10.1016/S1463-5003(02)00061-6, 2004.

Toggweiler, J. R. and Samuels, B.: Effect of Drake Passage on the global thermohaline circulation, Deep-Sea Res. I, 42, 477–500, https://doi.org/10.1016/0967-0637(95)00012-U, 1995.

Trenberth, K. E. and Caron, J. M.: Estimates of merional atmosphere and ocean heat transports, J. Climate, 14, 3433–3443, https://doi.org/10.1175/1520-0442(2001)014<3433:EOMAAO>2.0.CO;2, 2001.

Våge, K., Pickart, R. S., Moore, G. W. K., and Ribergaard, M. H.: Winter Mixed Layer Development in the Central Irminger Sea: The Effect of Strong, Intermittent Wind Events, J. Phys. Oceanogr., 38, 541–565, https://doi.org/10.1175/2007JPO3678.1, 2008.

Våge, K., Pickart, R., Sarafanov, A., Knutsen, Ø., Mercier, H., Lherminier, P., van Aken, H. M., Meincke, J., Quadfasel, D., and Bacon, S.: The Irminger Gyre: circulation, convection, and interannual veriability, Deep-Sea Res. I, 58, 590–614, https://doi.org/10.1016/j.dsr.2011.03001, 2011.

Valcke, S.: The OASIS3 coupler: a European climate modelling community software, Geosci. Model. Dev., 6, 373–388, https://doi.org/10.5194/gmd-6-373-2013, 2013.

Vancoppenolle, M., Fichefet, T., and Goosse, H.: Simulating the mass balance and salinity of Arctic and Antarctic sea ice. 2: Importance of sea ice salinity variations, Ocean. Modell., 27, 54–69, https://doi.org/10.1016/j.ocemod.2008.11.003, 2009.

von Storch, J.-S., Eden, C., Fast, I., Haak, H., Hernández-Deckers, D., Maier-Reimer, E., Marotzke, J., and Stammer, D.: An Estimate of the Lorenz Energy Cycle for the World Ocean Based on the STORM/NCEP Simulation, J. Phys. Oceanogr., 42, 2185–2205, https://doi.org/10.1175/JPO-D-12-079.1, 2012.

von Storch, J. S., Haak, H., Hertwig, E., and Fast, I.: Vertical heat and salt fluxes due to resolved and parameterized meso-scale Eddies, Ocean Model., 108, 1–19, https://doi.org/10.1016/j.ocemod.2016.10.001, 2016.

Wang, C., Zhang, L., Lee, S. K., Wu, L., and Mechoso, C. R.: A global perspective on CMIP5 climate model biases, Nat. Clim. Change, 4(3), 201–205, https://doi.org/10.1038/nclimate2118, 2014a.

Wang, Q., Danilov, S., Sidorenko, D., Timmermann, R., Wekerle, C., Wang, X., Jung, T., and Schröter, J.: The Finite Element Sea Ice-Ocean Model FESOM v.1.4: formulation of an ocean general circulation model, Geosci. Model. Dev., 7, 663–693, https://doi.org/10.5194/gmd-7-663-2014, 2014b.

Wang, Q., Wekerle, C., Danilov, S., Wang, X., and Jung, T.: A 4.5 km resolution Arctic Ocean simulation with the global multi-resolution model FESOM1.4, Geosci. Model Dev., 11, 1229–1255, https://doi.org/10.5194/gmd-11-1229-2018, 2018.

Wolff, J. O., Maier-Reimer, E., and Legutke, S.: The Hamburg Ocean Primitive Equation Model HOPE, Tech. Rep. 13, German Climate Computer Center (DKRZ), 1997.

Woodgate, R., Weingartner, T., and Lindsa, R.: Observed increases in Bering Strait oceanic fluxes from the Pacific to the Arctic from 2001 to 2011 and their impacts on the Arctic Ocean water column, Geophys. Res. Lett., 39, L24 603, https://doi.org/10.1029/2012GL054092, 2012.

Woodgate, R. A., Aagard, K., and Weingartner, T. J.: Interannual changes in the Bering Strait fluxes of volume, heat, and freshwater between 1991 and 2004, Geophys. Res. Lett., 33, L15 609, https://doi.org/10.1029/2006GL02693., 2006.

Zhang, J. and Rothrock, D. A.: Modeling Global Sea Ice with a Thickness and Enthalpy Distribution Model in Generalized Curvilinear Coordinates, Mon. Weather Rev., 131, 845–861, https://doi.org/10.1175/1520-0493(2003)131<0845:MGSIWA>2.0.CO;2, 2003.

Zhang, J. and Steele, M.: Effect of vertical mixing on the Atlantic Water layer circulation in the Arctic Ocean, Geophys. Res. Oceans, 112, C04S04, https://doi.org/10.1029/2006JC003732, 2007.

Table 1. Overview of MPI-ESM1.2 control simulations used within this study and their horizontal resolutions. The number of vertical levels are 95 in the atmosphere and 40 in the ocean, respectively. In brackets, the nominal horizontal resolution in a Gaussian grid (approximated at the equator) is given. All models use 30 years of spin-up and are analysed for the subsequent 50 years.

Name	Atmosphere resolution	Ocean resolution	[..[309]]Ocean mixing scheme	Description
HR	T127 (0.93° or ~103 km)	TP04 (0.4° or ~44 km)	PP, KPP	reference, ocean mixing sensitivity
XR	T255 (0.46° or ~51 km)	TP04 (0.4° or ~44 km)	PP, KPP	increased atmospheric resolution, ocean mixing ser
ER	T127 (0.93° or ~103 km)	TP6M (0.1° or ~11 km)	PP	increased ocean resolution

Table 2. Maximum values of barotropic stream function (gyre strengths) in Sverdrup ($\mathrm{Sv} := 10^6\,\mathrm{m}^3\,\mathrm{s}^{-1}$) simulated by MPI-ESM1.2 and from observations.

Region	HR_{pp}	HR_{kpp}	XR_{pp}	XR_{kpp}	ER_{pp}	Obs.	Reference
Subpolar gyre (North Atlantic)	34.6	40.6	31.0	32.1	36.6	26.0 to 40.0	Clark (1984); Bersch (1995); Bacon (1997); Lherminier et al. (2007); Holliday et al. (2009)
Subtropical gyre (North Atlantic)	48.2	64.9	44.0	63.9	62.8	46.0 to 61.0	Johns et al. (1995)
Subtropical gyre (North Pacific)	84.1	116.3	73.6	95.5	80.7	42.0±2.5	Imawaki et al. (2001)

Table 3. Simulated (mean ± one standard deviation) and observed net volume transports ($\mathrm{Sv} := 10^6\,\mathrm{m}^3\,\mathrm{s}^{-1}$) across sections (postive means northward).

Section	HR_{pp}	HR_{kpp}	XR_{pp}	XR_{kpp}	ER_{pp}	Obs.
Bering Strait	0.7 ± 0.1	0.7 ± 0.1	0.5 ± 0.1	0.6 ± 0.1	0.9 ± 0.1	0.8 [0.7 to 1.1]
Fram Strait	[..[310]]-2.5 ± 0.6	[..[311]]-1.9 ± 0.4	[..[312]]-2.5 ± 0.6	[..[313]]-1.9 ± 0.5	[..[314]]-1.0 ± 0.4	[..[315]]-1.75 ± [..[316]]5.01
Denmark Strait	[..[318]]-3.9 ± 0.6	[..[319]]-4.2 ± 0.7	[..[320]]-4.1 ± 0.6	[..[321]]-3.9 ± 0.7	[..[322]]-4.6 ± 0.4	[..[323]]-4.6
						[..[324]]-3.4 ± 1.4
						[..[325]]-3.2 ± 0.5
Iceland – Scotland	4.0 ± 0.8	5.0 ± 1.0	4.2 ± 0.8	4.4 ± 1.0	5.5 ± 0.6	4.8
						4.6 ± 0.25
						3.8 ± 0.6
Florida Current	14.6 ± 0.7	15.5 ± 0.7	12.4 ± 0.6	14.1 ± 0.6	24.7 ± 0.8	31.7
						31.6 ± 2.7
Strait of Gibraltar	0.04 ± 0.01	0.04 ± 0.01	0.04 ± 0.01	0.04 ± 0.01	0.05 ± 0.01	0.038 ± 0.007
						0.041
Indonesian Throughflow	8.5 ± 0.8	9.5 ± 0.9	8.0 ± 0.5	8.5 ± 0.8	13.0 ± 0.8	11.6 to 15.7
Mozambique Channel	8.8 ± 1.7	6.5 ± 2.0	8.0 ± 1.3	5.3 ± 1.9	13.6 ± 1.2	5.0 to 26.0
						16.7 ± 8.9
Drake Passage	161.7 ± 3.0	191.9 ± 2.6	150.1 ± 4.1	170.2 ± 3.0	140.9 ± 3.0	134.0 ± 14.0
						137.0 ± 8.0
						136.7 ± 6.9
						173.3 ± 10.7

Table 4. Time-mean AMOC volume transports ($\pm$ one standard deviation of annual means) at $26\,^{\circ}\mathrm{N}$ in $1000\,\mathrm{m}$ depth simulated by MPI-ESM1.2 and the depth of the North Atlantic Deep Water (NADW) cell at $26.5\,^{\circ}\mathrm{N}$ (defined where the stream function crosses zero). The observed annual mean ($\pm$ on standard deviation) NADW cell depth from the RAPID-MOCHA-WBTS array (Smeed et al., 2017) is $4379 \pm 279\,\mathrm{m}$. Further, the time-mean ($\pm$ one standard deviation of annual means) heat and salt transports across $50\,^{\circ}\mathrm{N}$ are shown (positive means northward transport).

Property	HR_{pp}	HR_{kpp}	XR_{pp}	XR_{kpp}	ER_{pp}
AMOC volume (Sv)	14.9 ± 3.5	18.9 ± 4.0	11.0 ± 3.8	14.6 ± 3.9	14.9 ± 3.6
NADW cell depth (m)	2865 ± 270	3176 ± 334	2665 ± 287	2979 ± 489	2941 ± 265
Atl. heat transport across $50\,^{\circ}\mathrm{N}$ (PW)	0.60 ± 0.04	0.63 ± 0.06	0.42 ± 0.06	0.52 ± 0.05	0.57 ± 0.03
Atl. salt transport across $50\,^{\circ}\mathrm{N}$ ($10^6\,\mathrm{kg\,s^{-1}}$)	0.28 ± 1.89	0.64 ± 2.18	-1.04 ± 2.54	0.4 ± 2.11	-0.22 ± 1.27

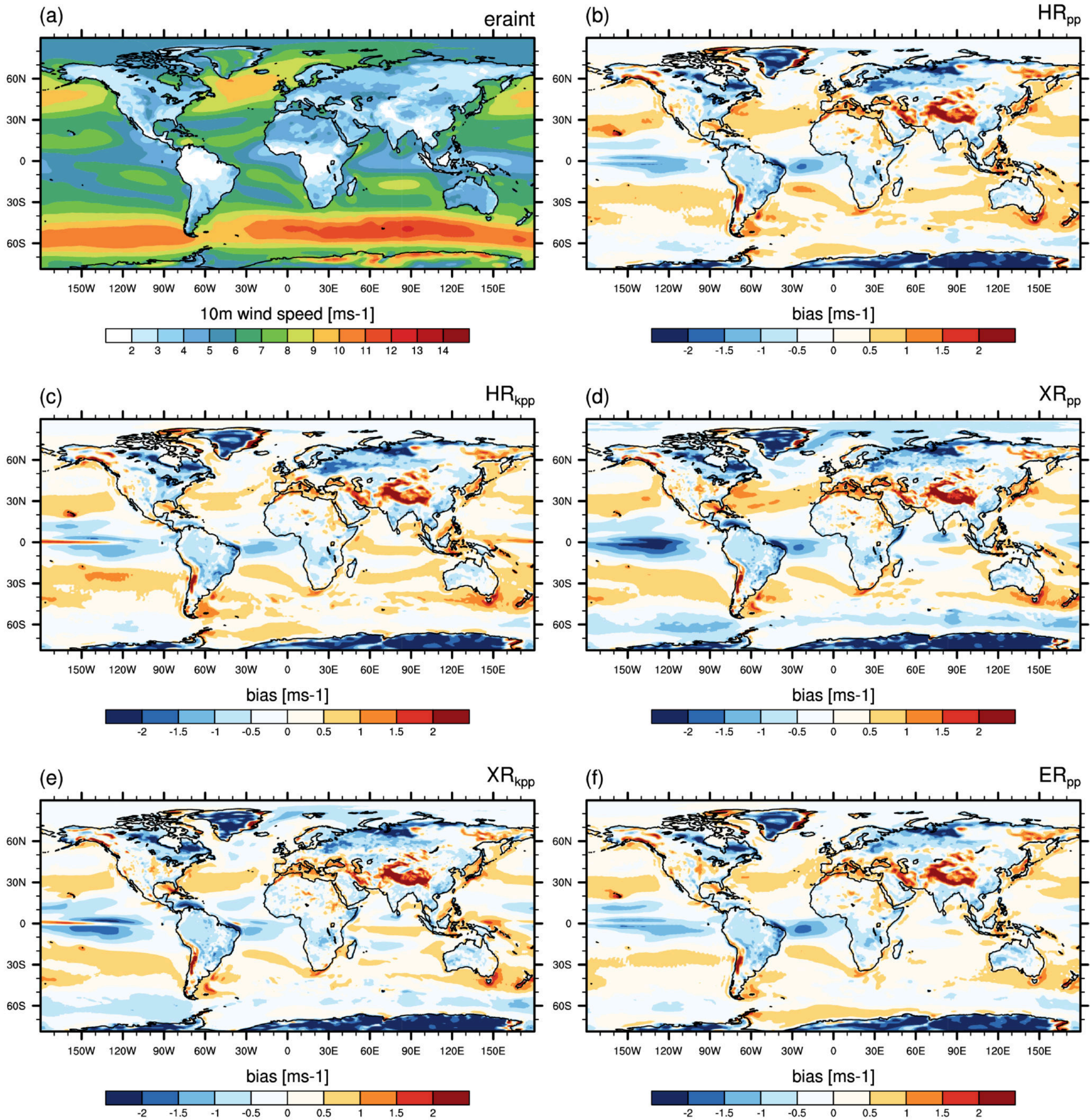

Figure 1. Annual mean 10 m wind speed from (a) ERA-Interim (1979–2005) and the bias of: (b) HR_{pp}, (c) HR_{kpp}, (d) XR_{pp}, (e) XR_{kpp}, and (f) ER_{pp}.

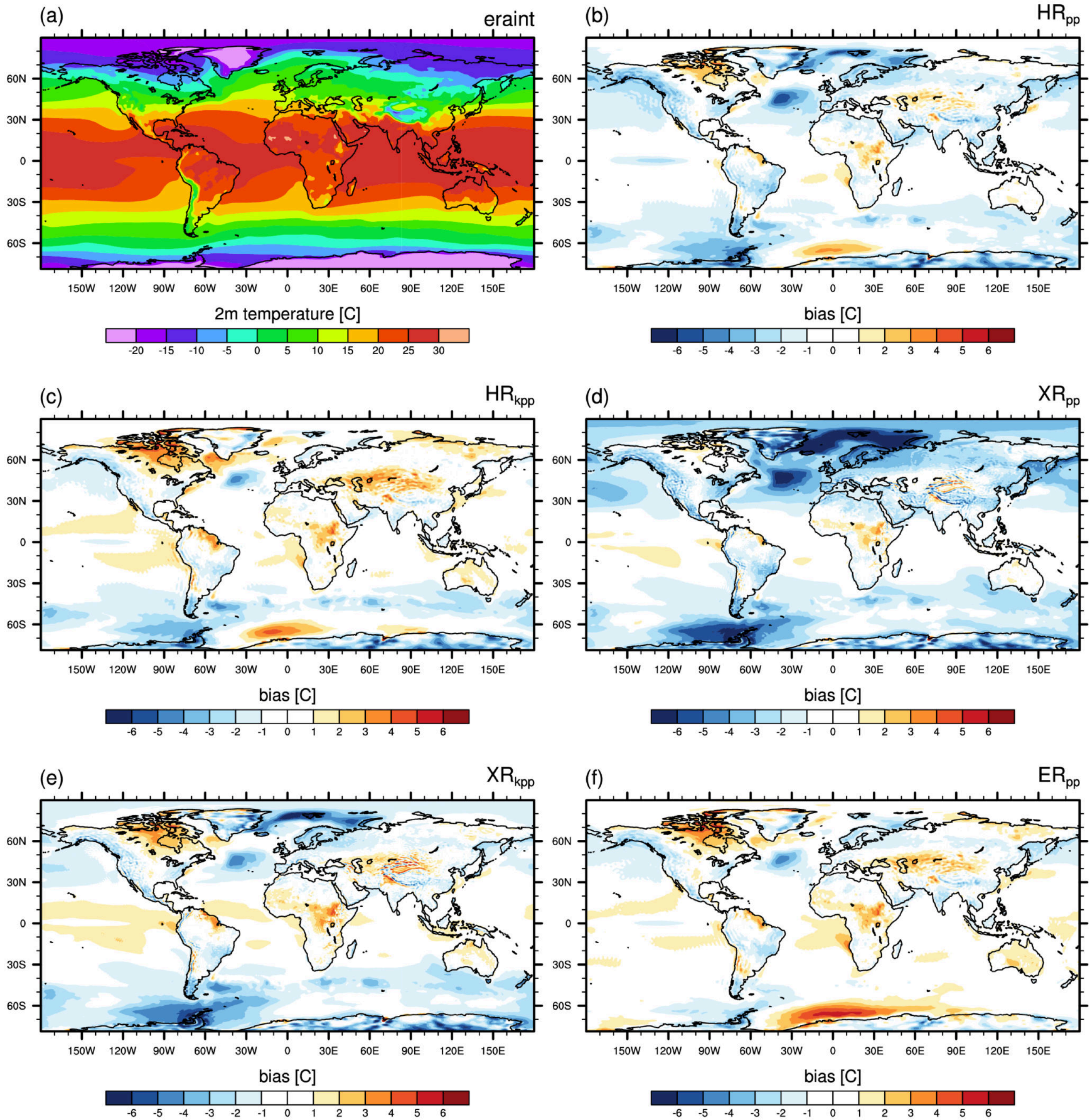

Figure 2. Annual mean 2 m temperature from (a) ERA-Interim (1979–2005) and the bias of: (b) HR_{pp}, (c) HR_{kpp}, (d) XR_{pp}, (e) XR_{kpp}, and (f) ER_{pp}.

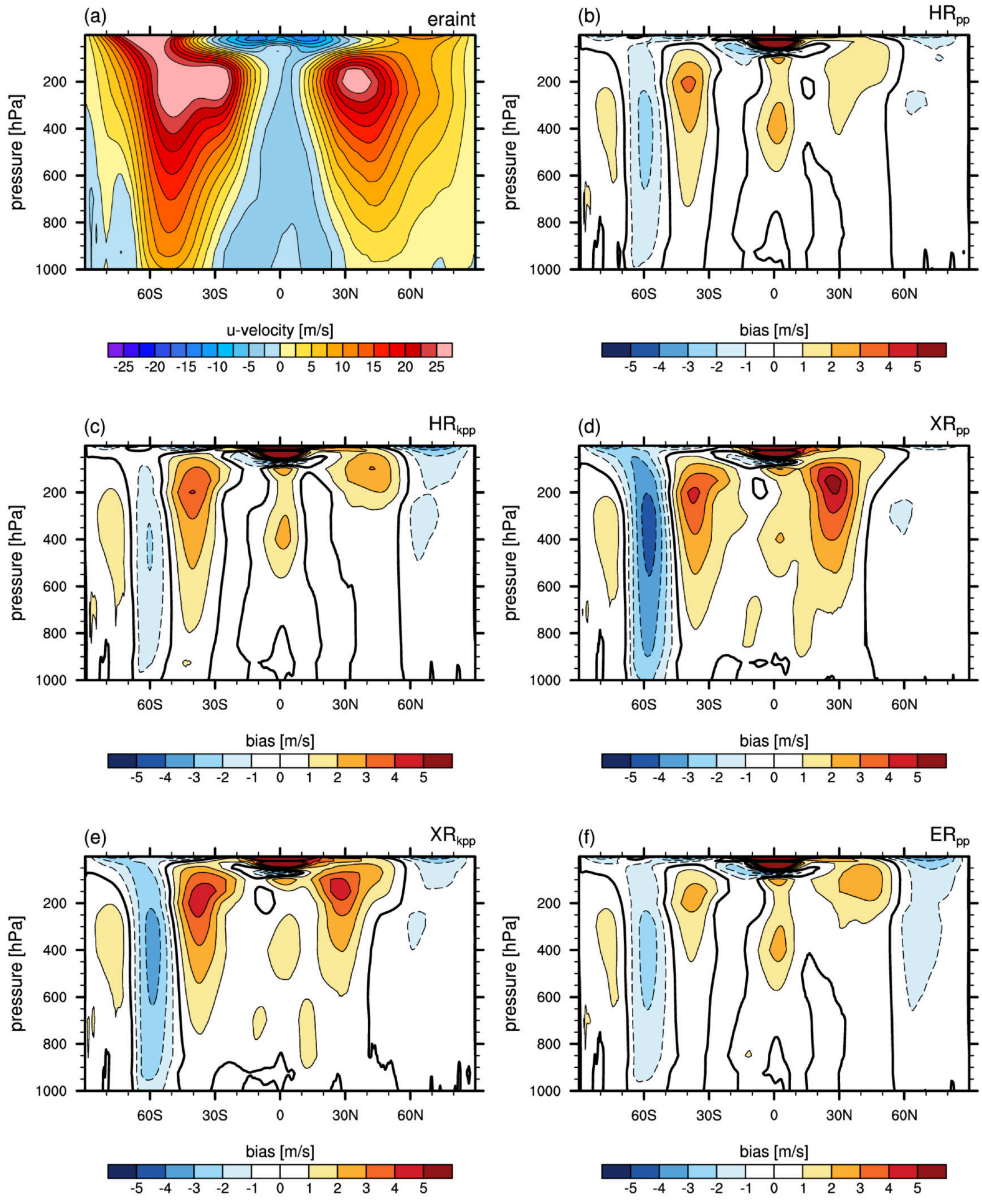

Figure 3. Global zonally-averaged u-velocity from (a) ERA-Interim (1979–2005) and the bias (MPI-ESM1.2 minus ERA-Interim) of: (b) HR_{pp}, (c) HR_{kpp}, (d) XR_{pp}, (e) XR_{kpp}, and (f) ER_{pp}. The zero contour line is shown as a thick solid line; negative (positive) contours are dashed (solid).

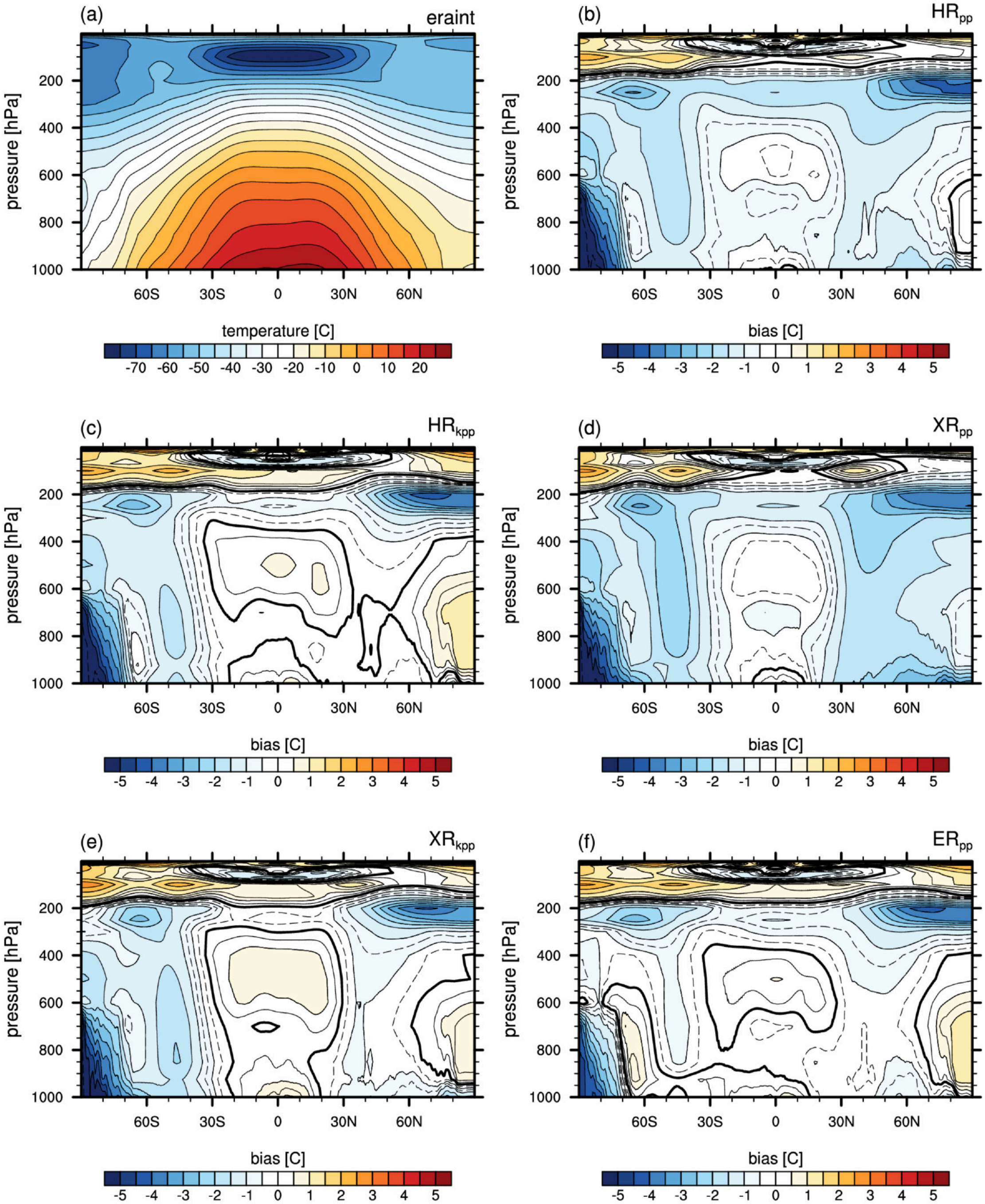

Figure 4. Global zonally-averaged temperature from (a) ERA-Interim (1979–2005) and the bias (MPI-ESM1.2 minus ERA-Interim) of (b) HR_{pp}, (c) HR_{kpp}, (d) XR_{pp}, (e) XR_{kpp}, and (f) ER_{pp}. The contour lines in b-f span ± 0.75 with an interval of 0.5K, and of 1.0K outside that range. The zero contour line is shown as a thick solid line; negative (positive) contours are dashed (solid).

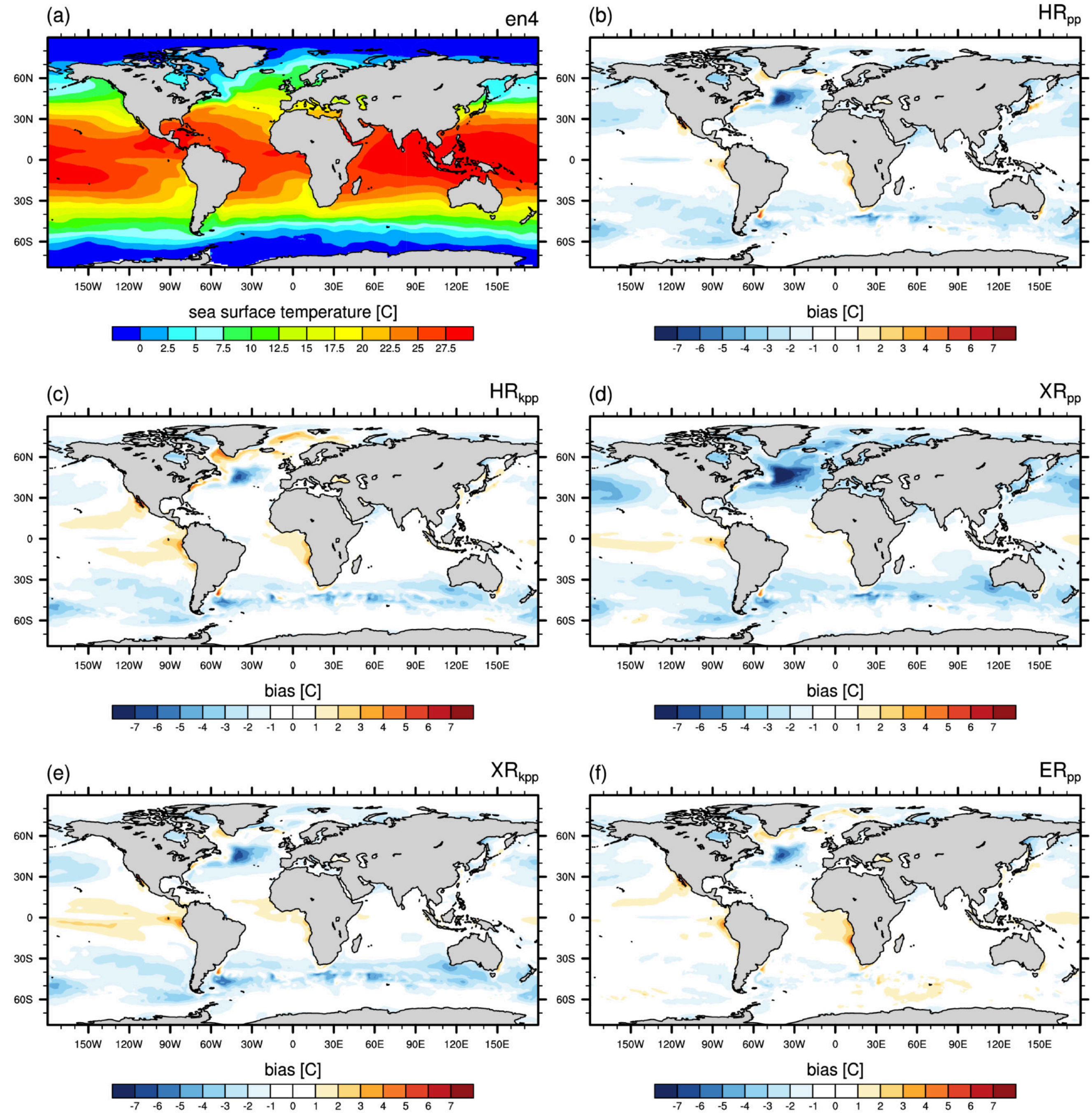

Figure 5. Sea surface temperature (°C) from (a) EN4 (averaged over 1945–1955) and differences: MPI-ESM1.2 minus EN4 for (b) HR_{pp},(c) HR_{kpp}, (d) XR_{pp}, [..[326]](e) XR_{kpp}, and (f) ER_{pp}.

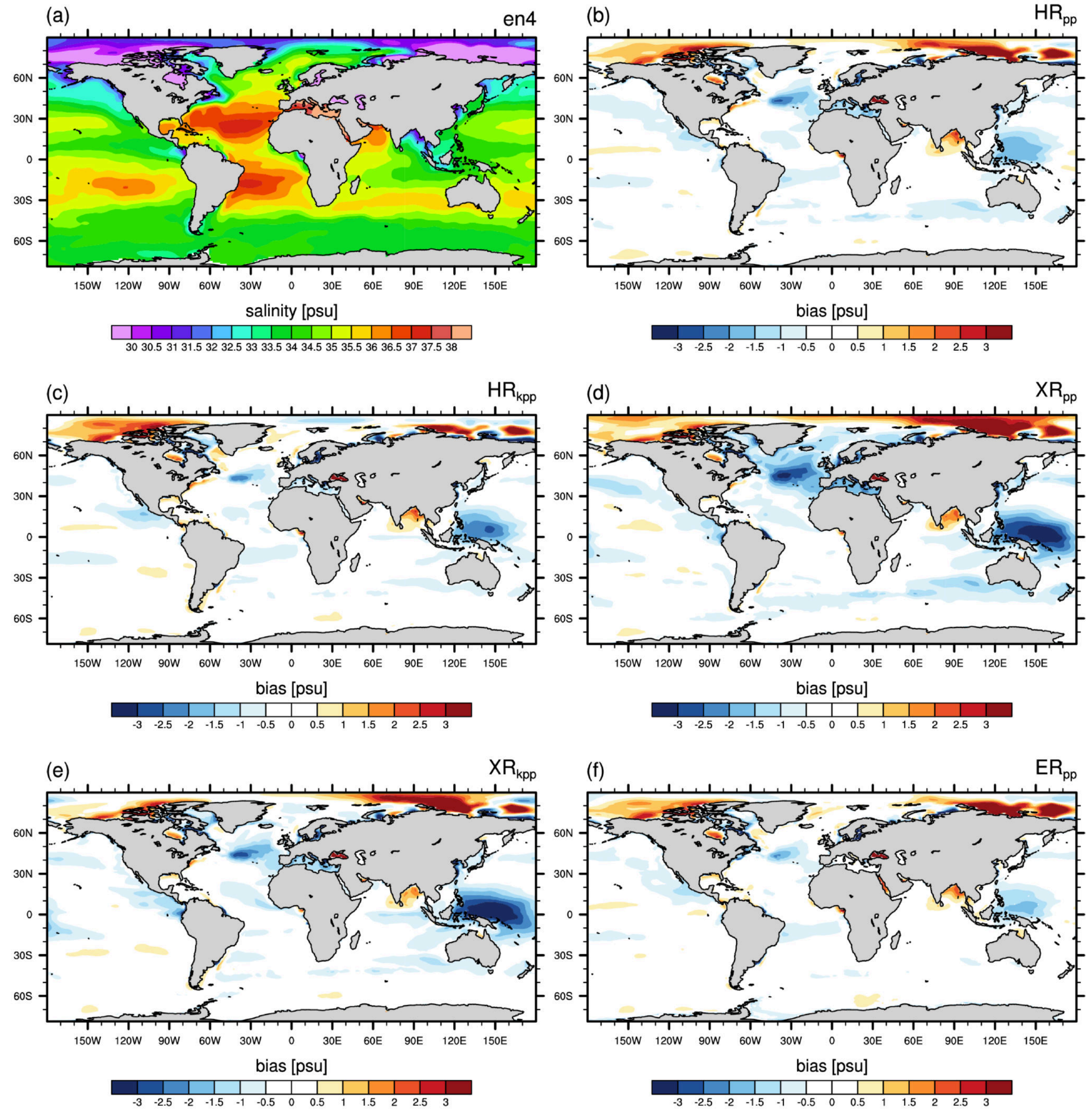

Figure 6. Sea surface salinity (psu) from (a) EN4 (averaged over 1945–1955) and for the differences: MPI-ESM1.2 minus EN4 for (b) HR$_{pp}$,(c) HR$_{kpp}$, (d) XR$_{pp}$, [..[327]](e) XR$_{kpp}$, and (f) ER$_{pp}$.

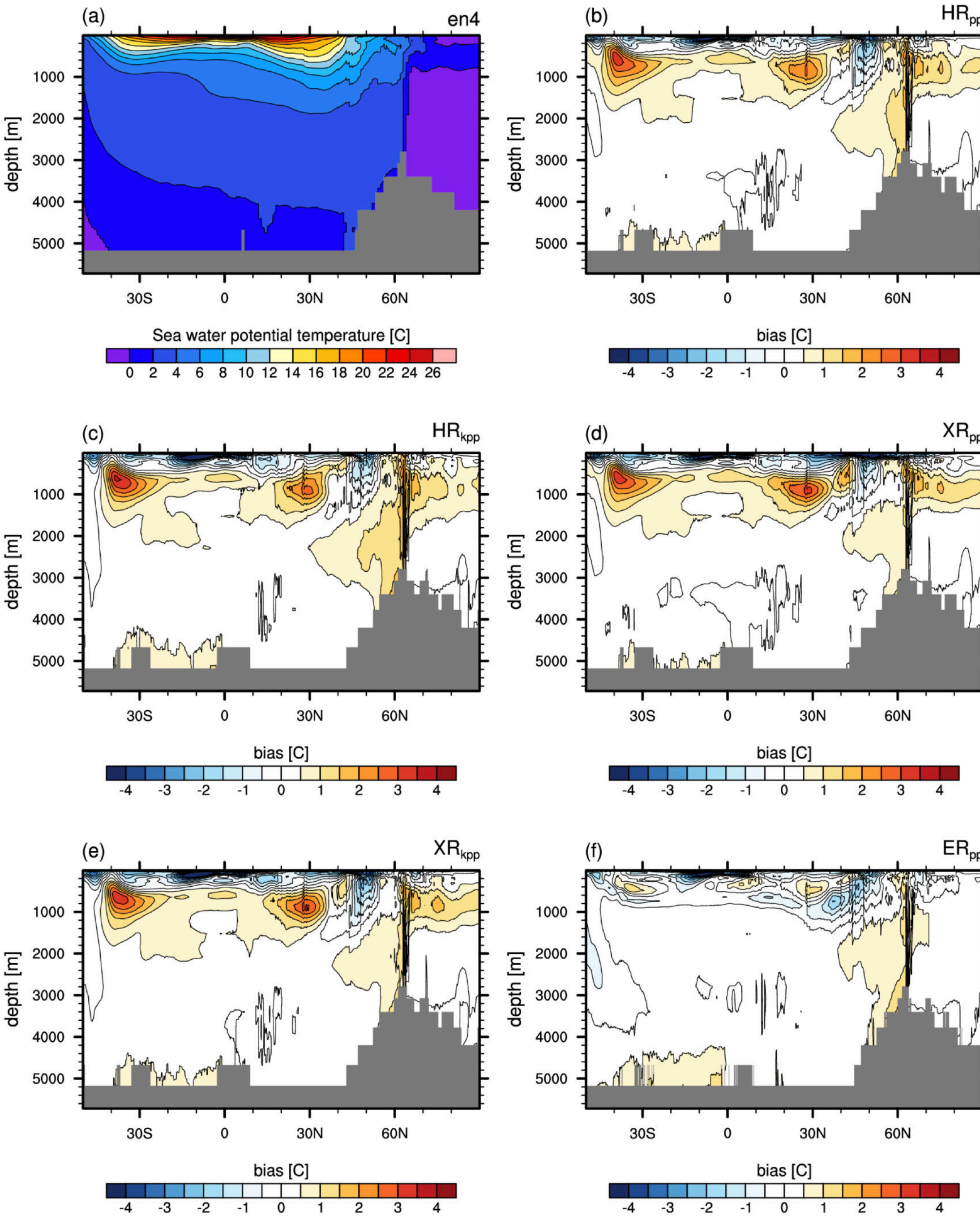

Figure 7. Zonal mean temperature transect through the Atlantic basin and the Arctic Ocean of (a) EN4 (averaged over 1945–1955) and the bias (MPI-ESM1.2 minus EN4) of (b) HR_{pp}, (c) HR_{kpp}, (d) XR_{pp}, (e) XR_{kpp}, and (f) ER_{pp}. Contour levels (b-f) begin with $\pm 0.5\,^{\circ}$C.

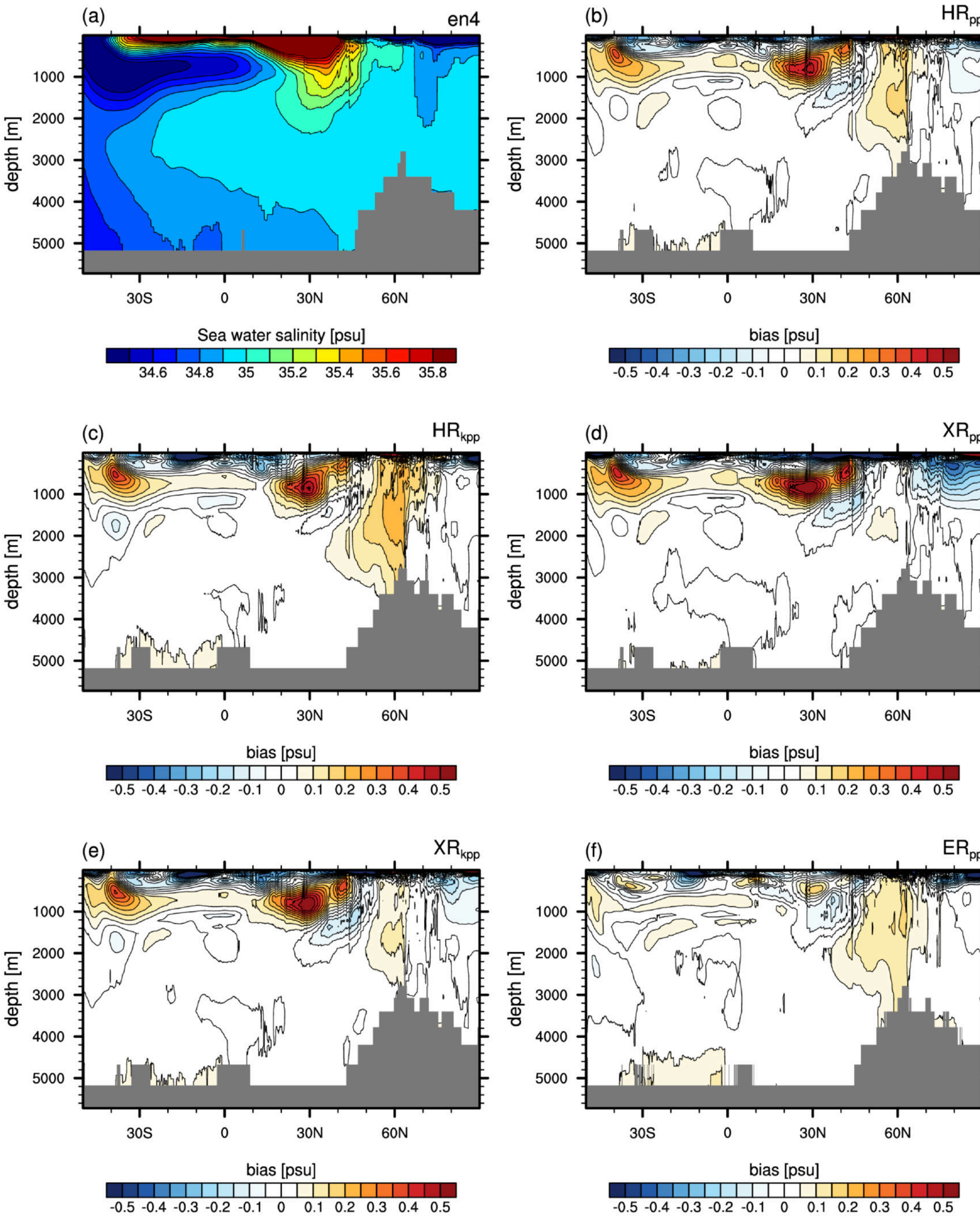

Figure 8. Zonal mean salinity transect through the Atlantic basin and the Arctic Ocean of (a) EN4 (averaged over 1945–1955) and the bias (MPI-ESM1.2 minus EN4) (b) HR_{kpp}, (c) XR_{pp}, and (d) XR_{kpp}, (e) XR_{kpp}, and (f) ER_{pp}. Contour levels (b-f) begin with ± 0.05 psu.

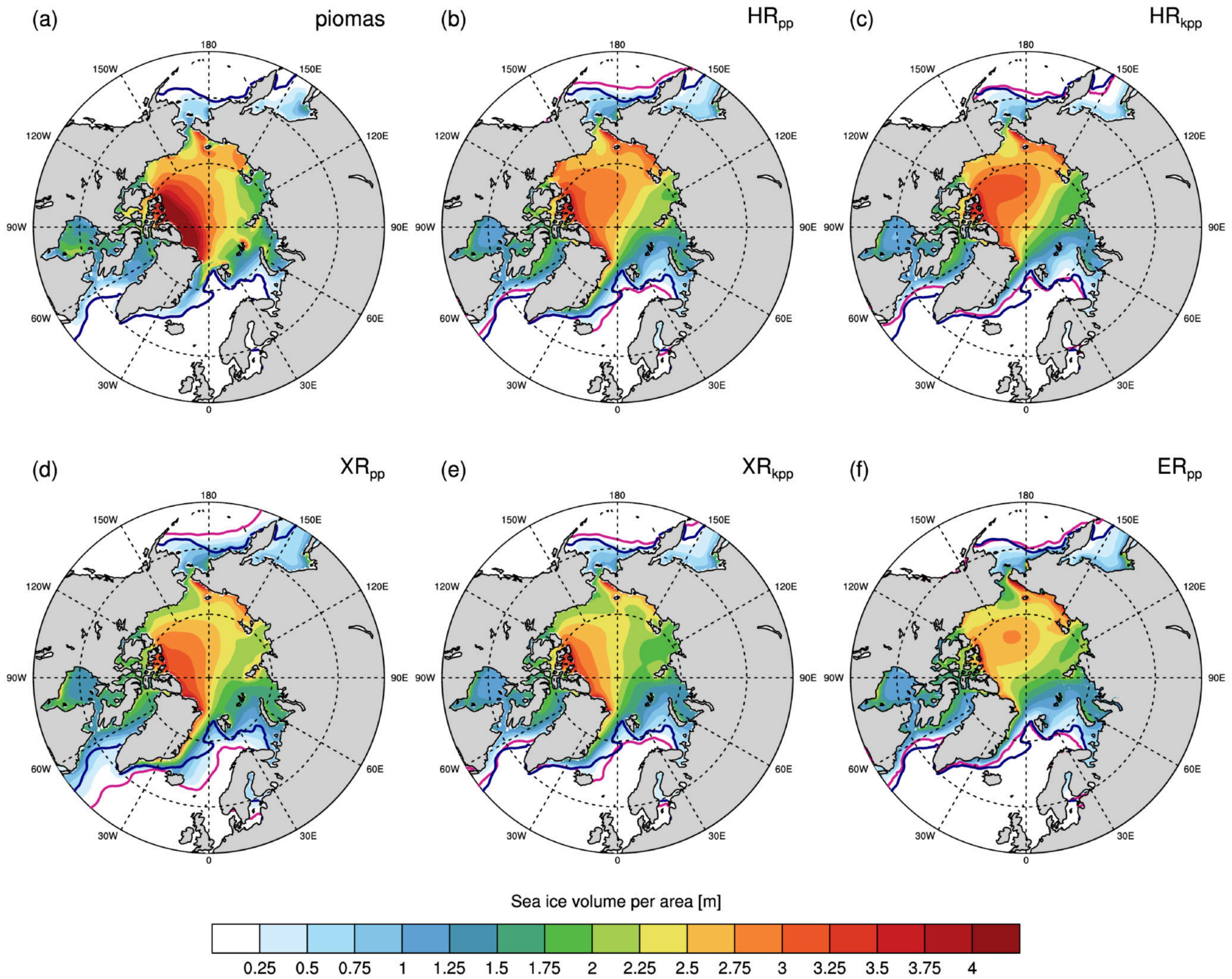

Figure 9. Time-averaged Arctic sea ice [..[328]]thickness in March for (a) PIOMAS reanalysis (Zhang and Rothrock, 2003), (b) HR_{pp}, ([..[329]]c) HR_{kpp}, ([..[330]]d) XR_{pp}, ([..[331]]e) XR_{kpp}, and ([..[332]]f) ER_{pp}. Simulations include their 15 % sea ice concentration contour in magenta and all figures the EUMETSAT OSI SAF observed ice edge (15% contour) in dark blue (averaged March 1979–2005).

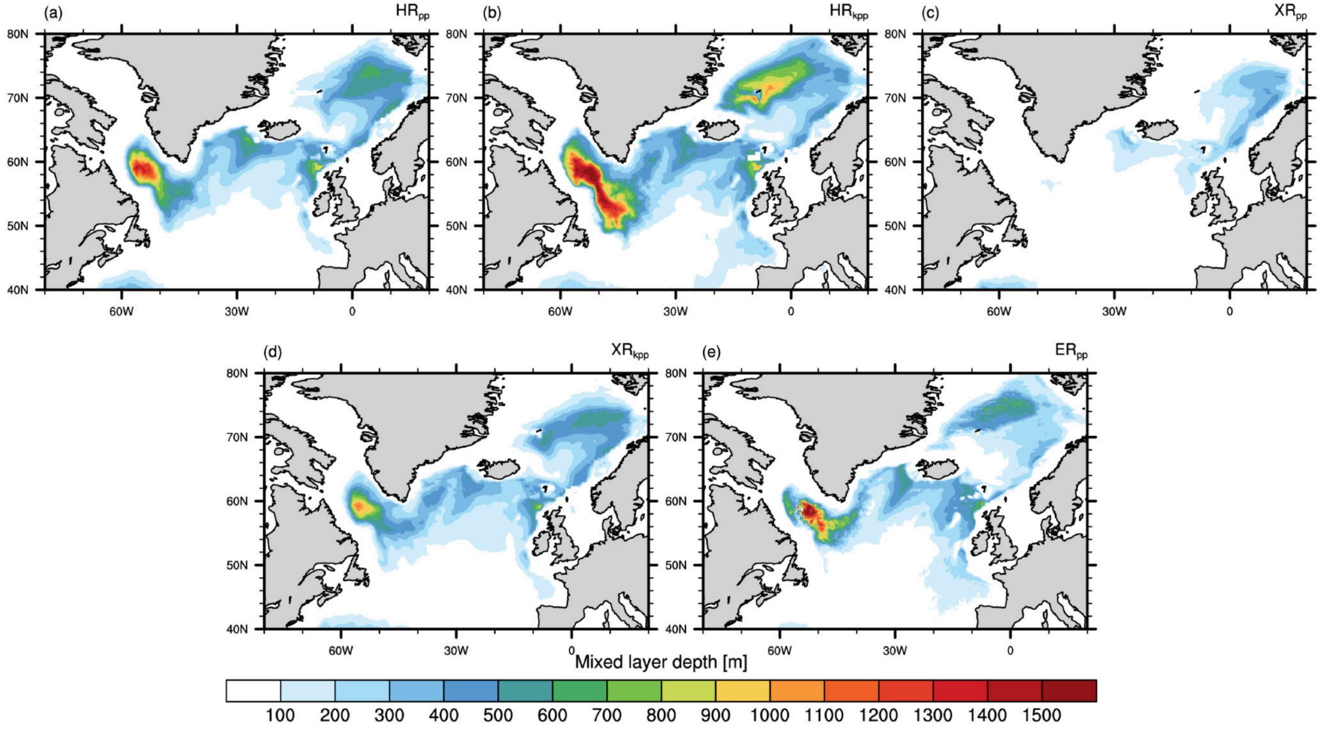

Figure 10. Time-averaged mixed layer depth ($\sigma_t = 0.01\,\mathrm{kg\,m^{-3}}$) in March in the North Atlantic and the Nordic Seas for (a) HR$_{\mathrm{pp}}$, (b) HR$_{\mathrm{kpp}}$, (c) XR$_{\mathrm{pp}}$, (d) XR$_{\mathrm{kpp}}$, and (e) ER$_{\mathrm{pp}}$.

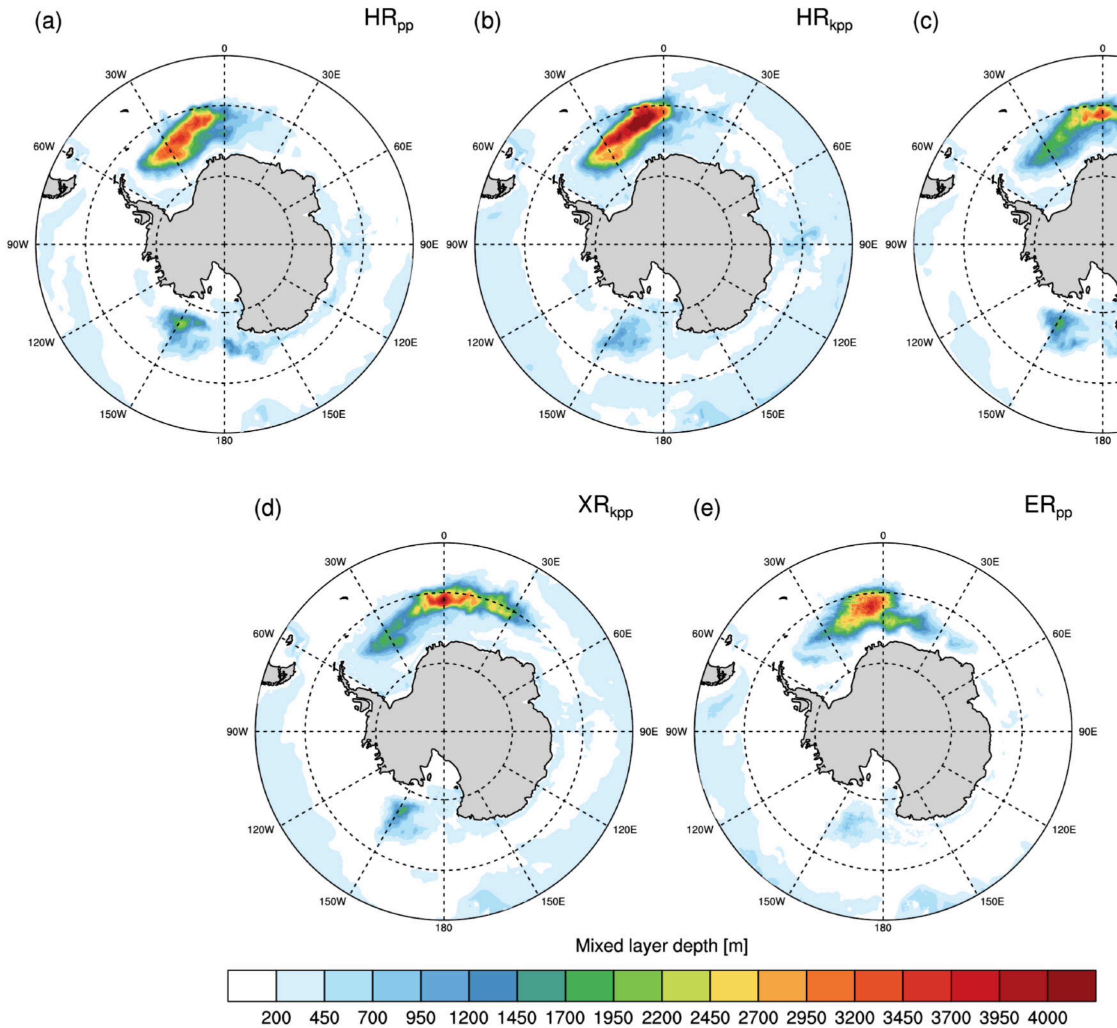

Figure 11. Time-averaged mixed layer depth ($\sigma_t = 0.03\,\mathrm{kg\,m^{-3}}$) in September in the Southern Ocean for (a) $\mathrm{HR_{pp}}$, (b) $\mathrm{HR_{kpp}}$, (c) $\mathrm{XR_{pp}}$, (d) $\mathrm{XR_{kpp}}$, and (e) $\mathrm{ER_{pp}}$.

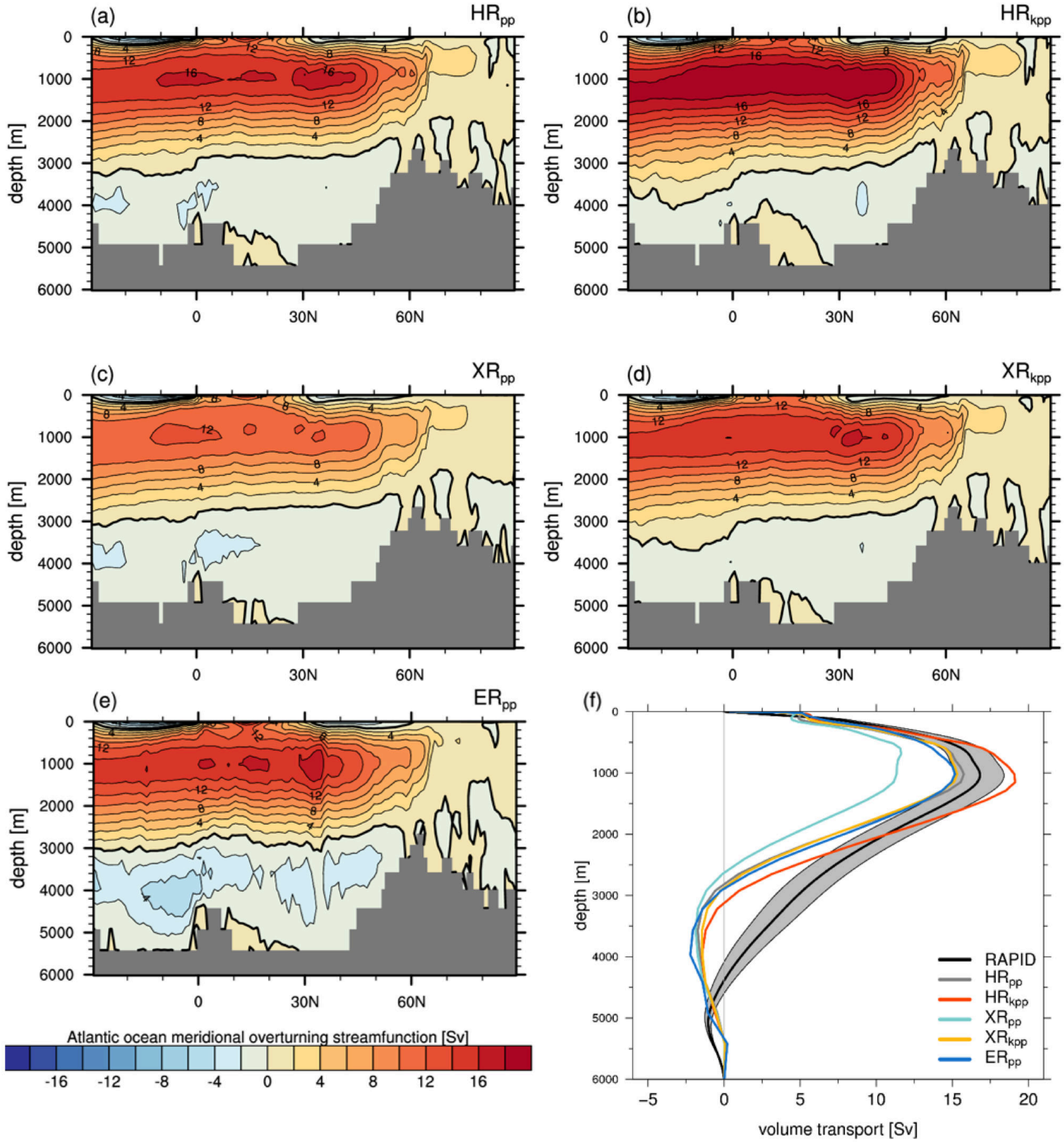

Figure 12. Eulerian stream function ($\mathrm{Sv} := 10^6\,\mathrm{m}^3\,\mathrm{s}^{-1}$) of the Atlantic Meridional Overturning Circulation (AMOC) for (a) $\mathrm{HR_{pp}}$,(b) $\mathrm{HR_{kpp}}$, (c) $\mathrm{XR_{pp}}$, (d) $\mathrm{XR_{kpp}}$, and (e) $\mathrm{ER_{pp}}$. The zero contour is drawn as a thicker line. In (f) annual mean profiles of the AMOC at 26.5° N are shown as observed from Apr 2004 to Feb 2017 by the RAPID-MOCHA-WBTS array (± one standard deviation marked by grey shading) (Smeed et al., 2017) and simulated by MPI-ESM1.2.

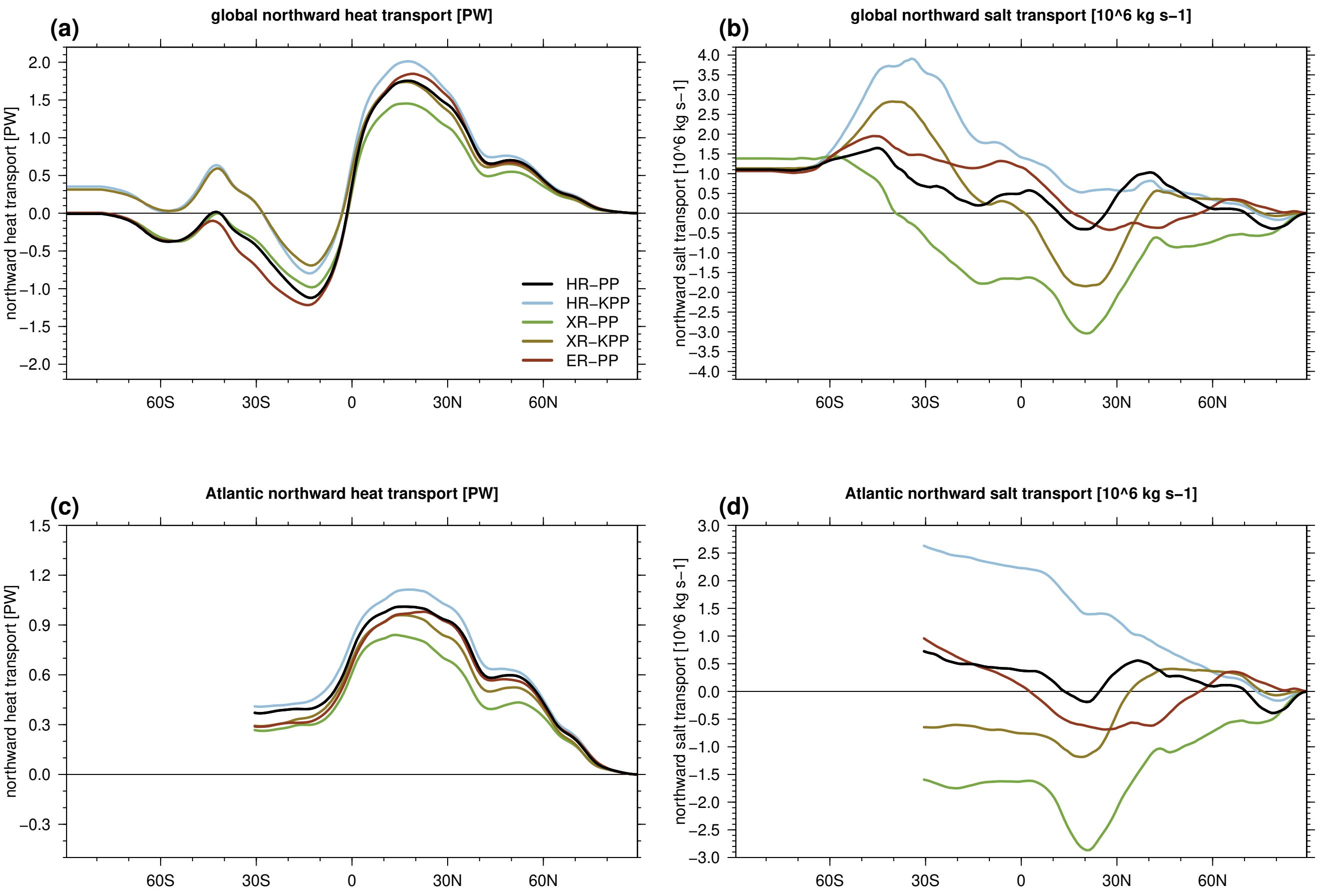

Figure A1. [..333]Time-averaged northward heat ([..334]PW) [..335]and salt transport ($10^6\,\mathrm{kg\,s^{-1}}$) in the [..336]global ocean (a[..337],[..338]b) [..339]and in the Atlantic basin (c[..340],[..341]d)[..342]. Note the different scaling in (c) and ([..343]d)[..344].

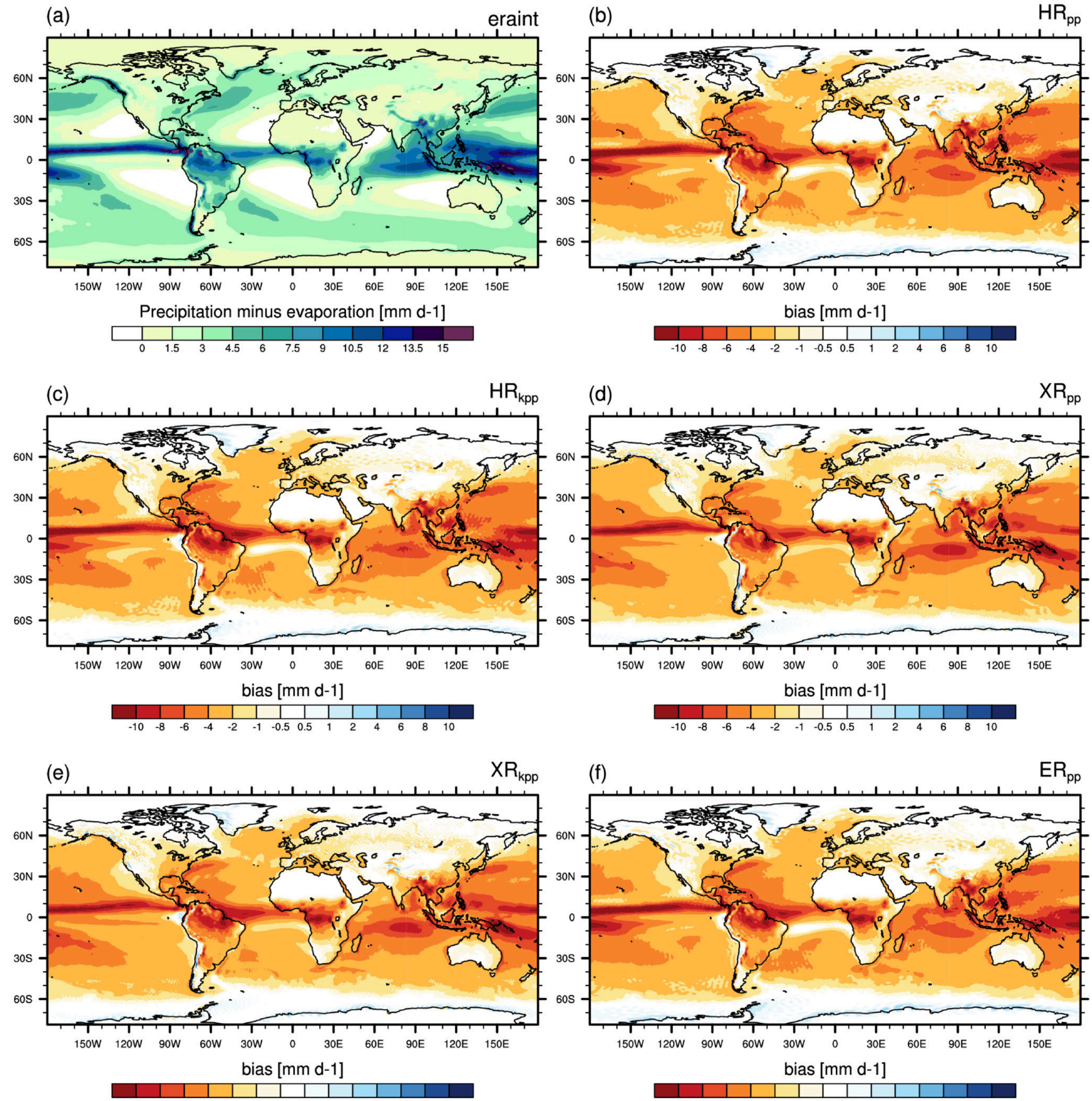

Figure A2. [..[345]]Time-averaged precipitation minus evaporation from ([..[346]]a) [..[347]]ERA-Interim (1979–2005) and the [..[348]]bias of: ([..[349]]b) HR_{pp}, ([..[350]]c) HR_{kpp}, ([..[351]]d) XR_{pp}, ([..[352]]e) XR_{kpp}, and ([..[353]]f) ER_{pp}.[..[354]]

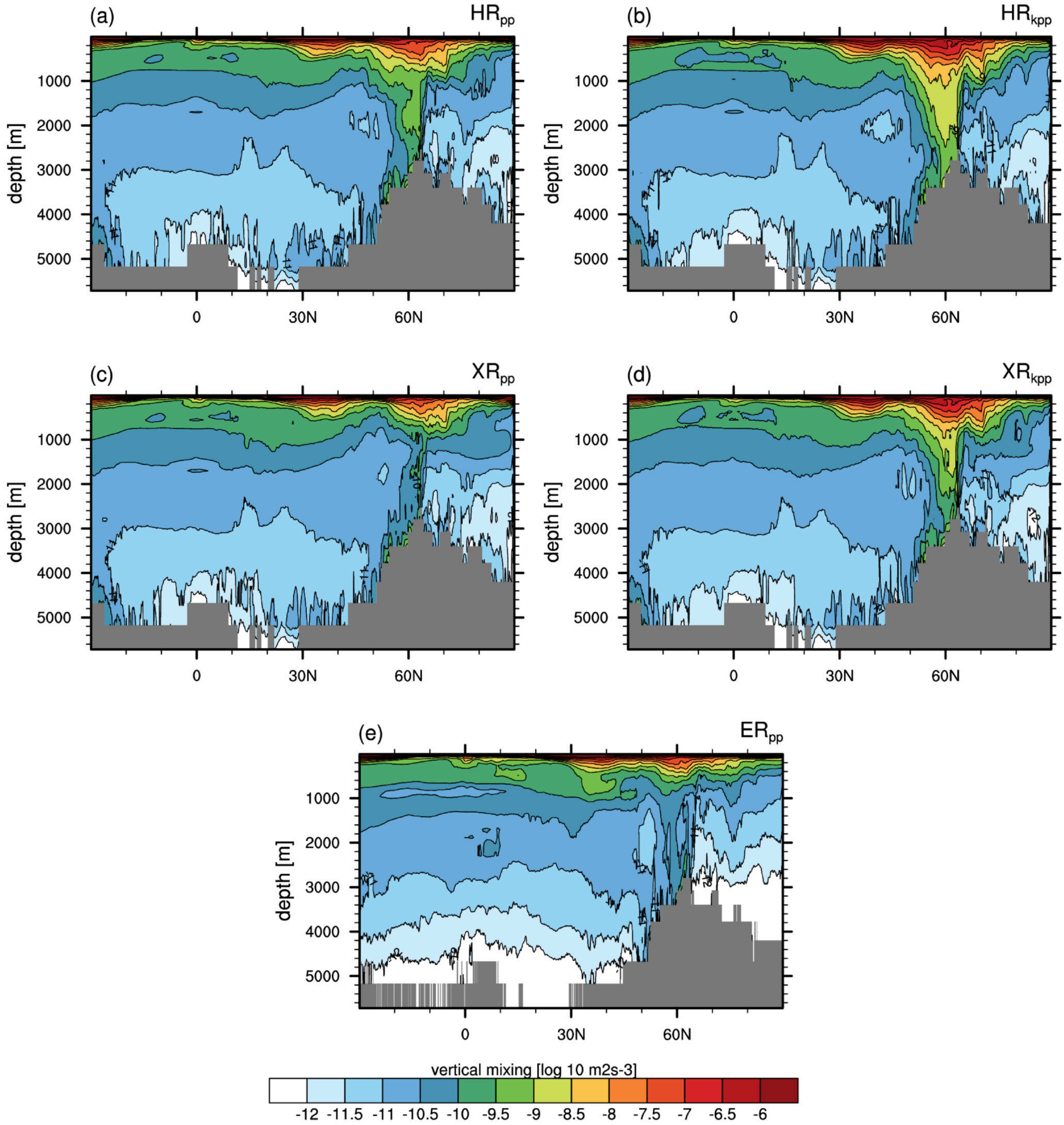

Figure A3. [..[355]]Transect of zonal mean vertical mixing ([..[356]]$log_{10}(k_v N^2)$) [..[357]]through the [..[358]]Atlantic basin and the Arctic Ocean of (a) [..[359]]HR$_{pp}$, ([..[360]]b) HR$_{kpp}$, ([..[361]]c) XR$_{pp}$, ([..[362]]d) XR$_{kpp}$, and ([..[363]]e) ER$_{pp}$.

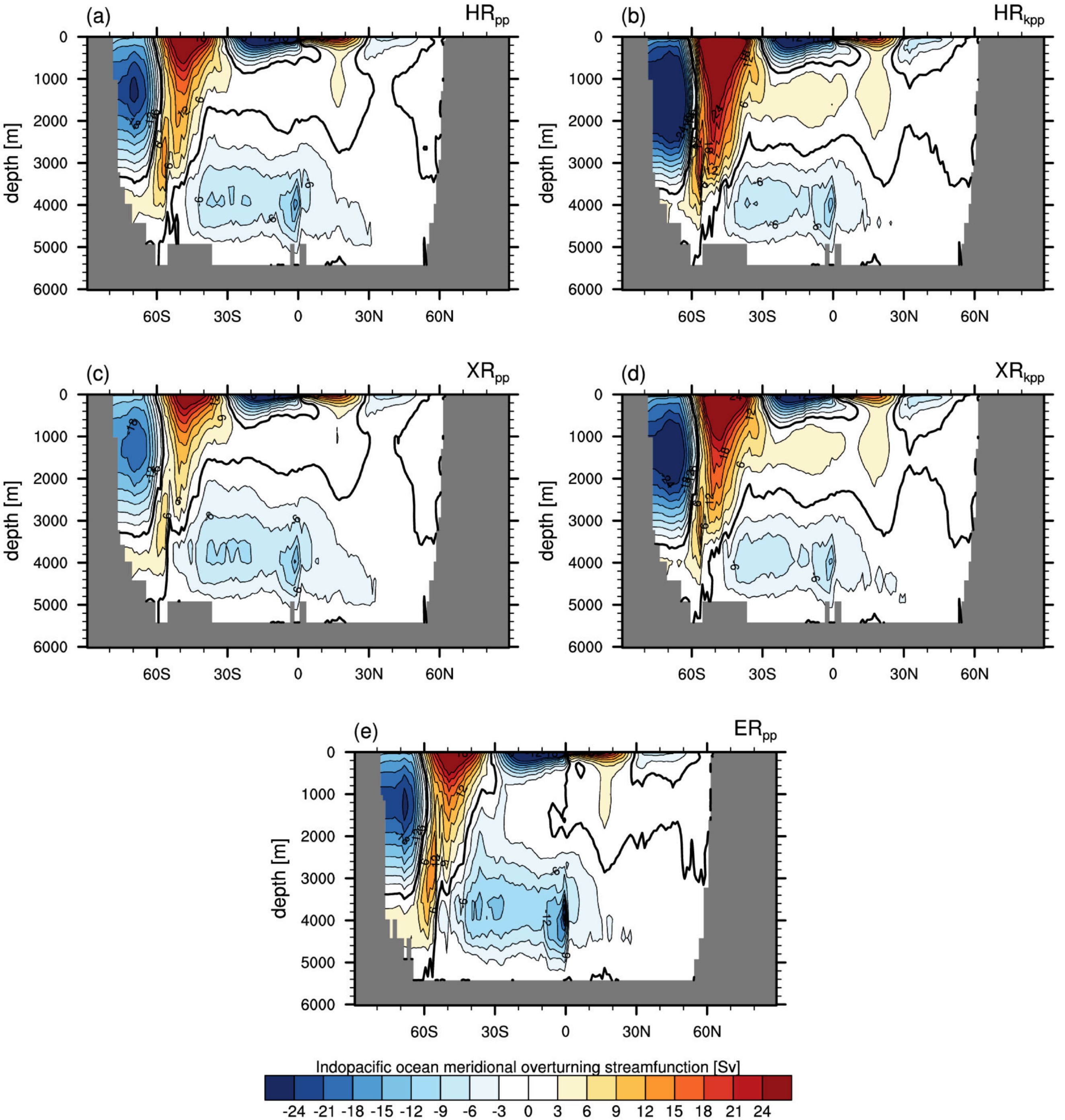

Figure A4. Eulerian stream function ($\mathrm{Sv} := 10^6\,\mathrm{m}^3\,\mathrm{s}^{-1}$) of the Pacific meridional overturning circulation for (a) HR$_{pp}$, (b) HR$_{kpp}$, (c) XR$_{pp}$, (d) XR$_{kpp}$, and (e) ER$_{pp}$. The zero contour is drawn as a thicker line.

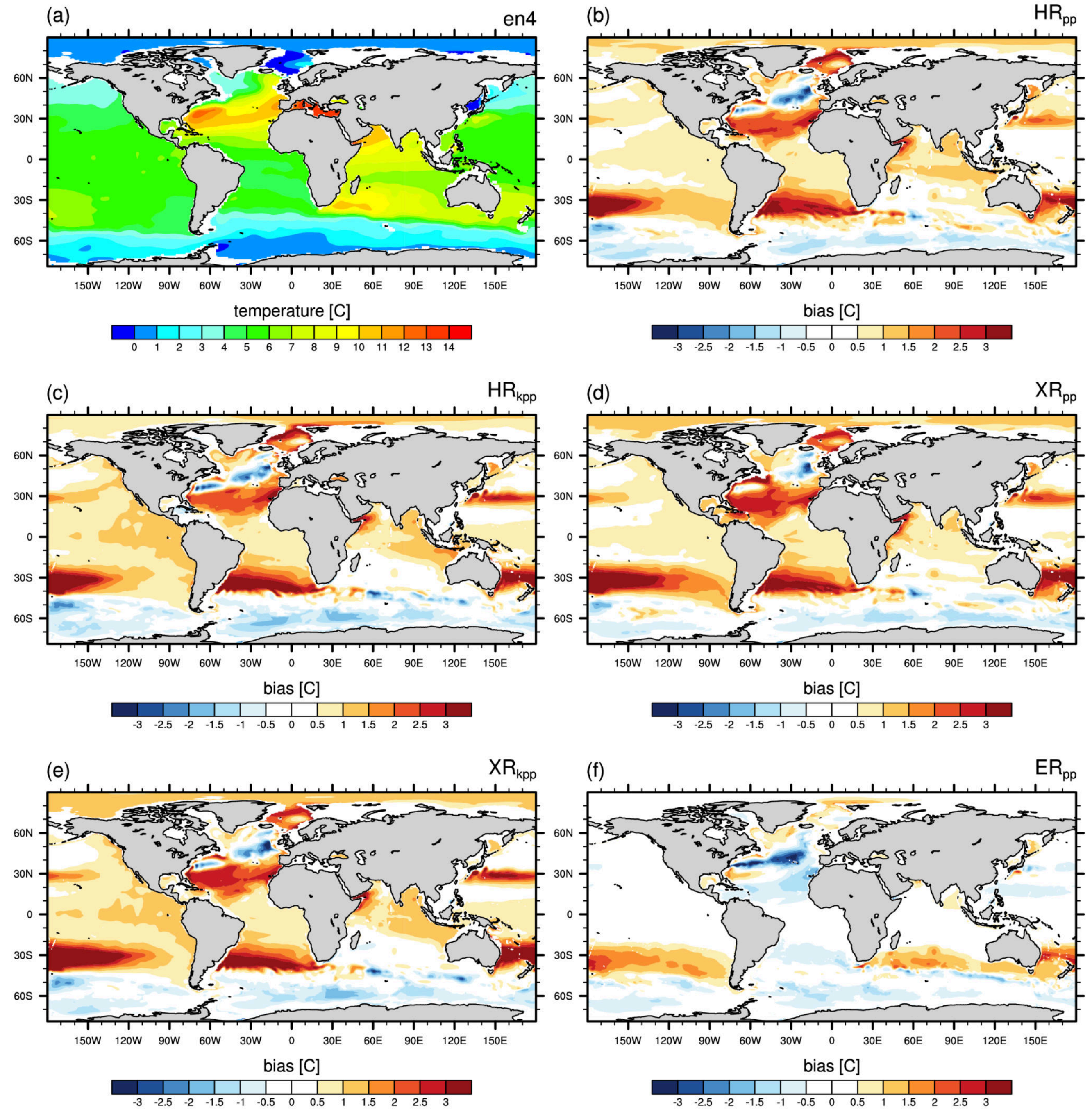

Figure A5. Sea water potential temperature (°C) at a depth of 740 m from (a) EN4 (averaged over 1945–1955) and differences: MPI-ESM1.2 minus EN4 for (b) HR_{pp},(c) HR_{kpp}, (d) XR_{pp}, (e) XR_{kpp}, and (f) ER_{pp}.

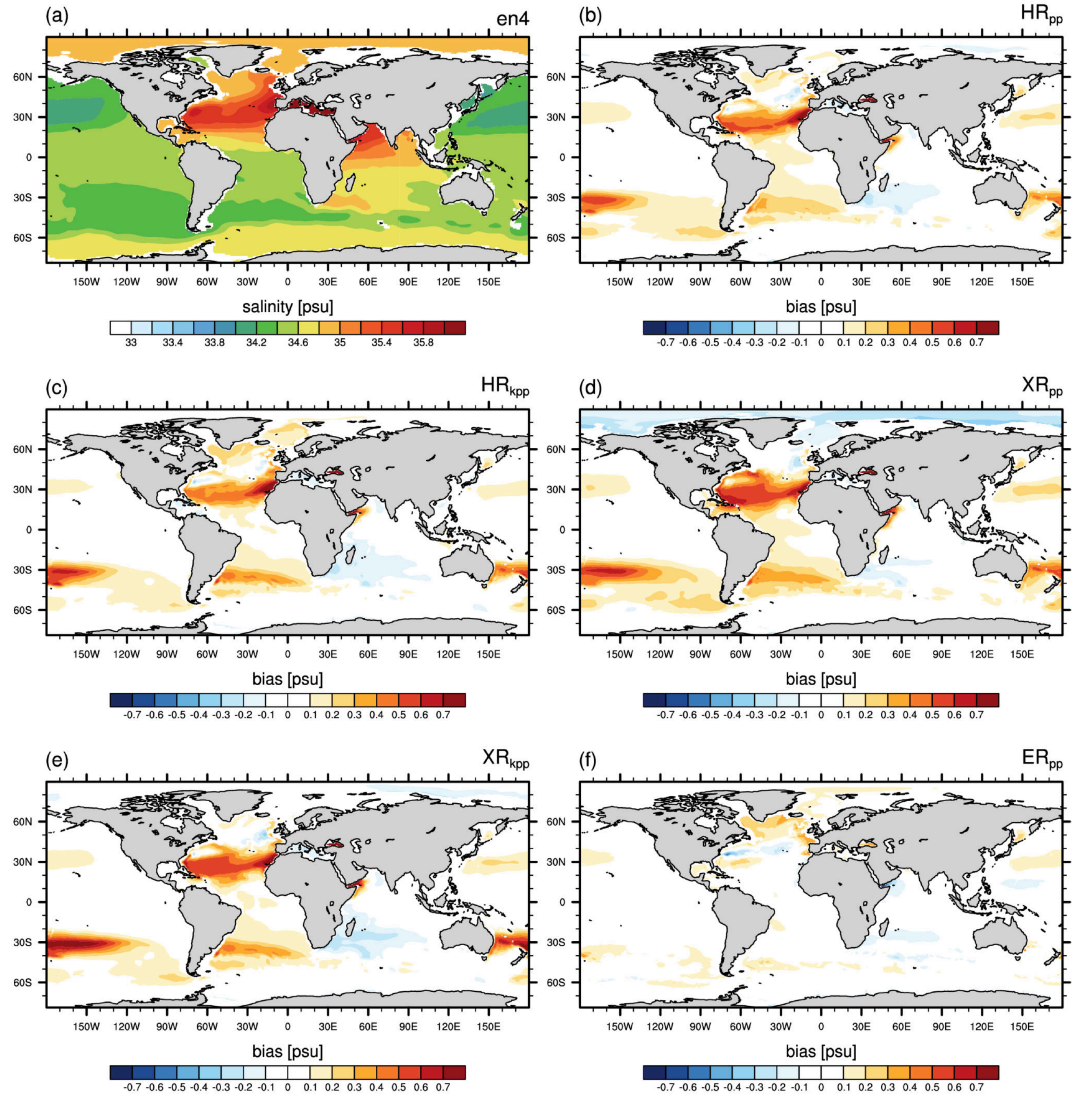

Figure A6. Sea water salinity (psu) at a depth of 740 m from (a) EN4 (averaged over 1945–1955) and differences: MPI-ESM1.2 minus EN4 for (b) HR_{pp},(c) HR_{kpp}, (d) XR_{pp}, (e) XR_{kpp}, and (f) ER_{pp}.

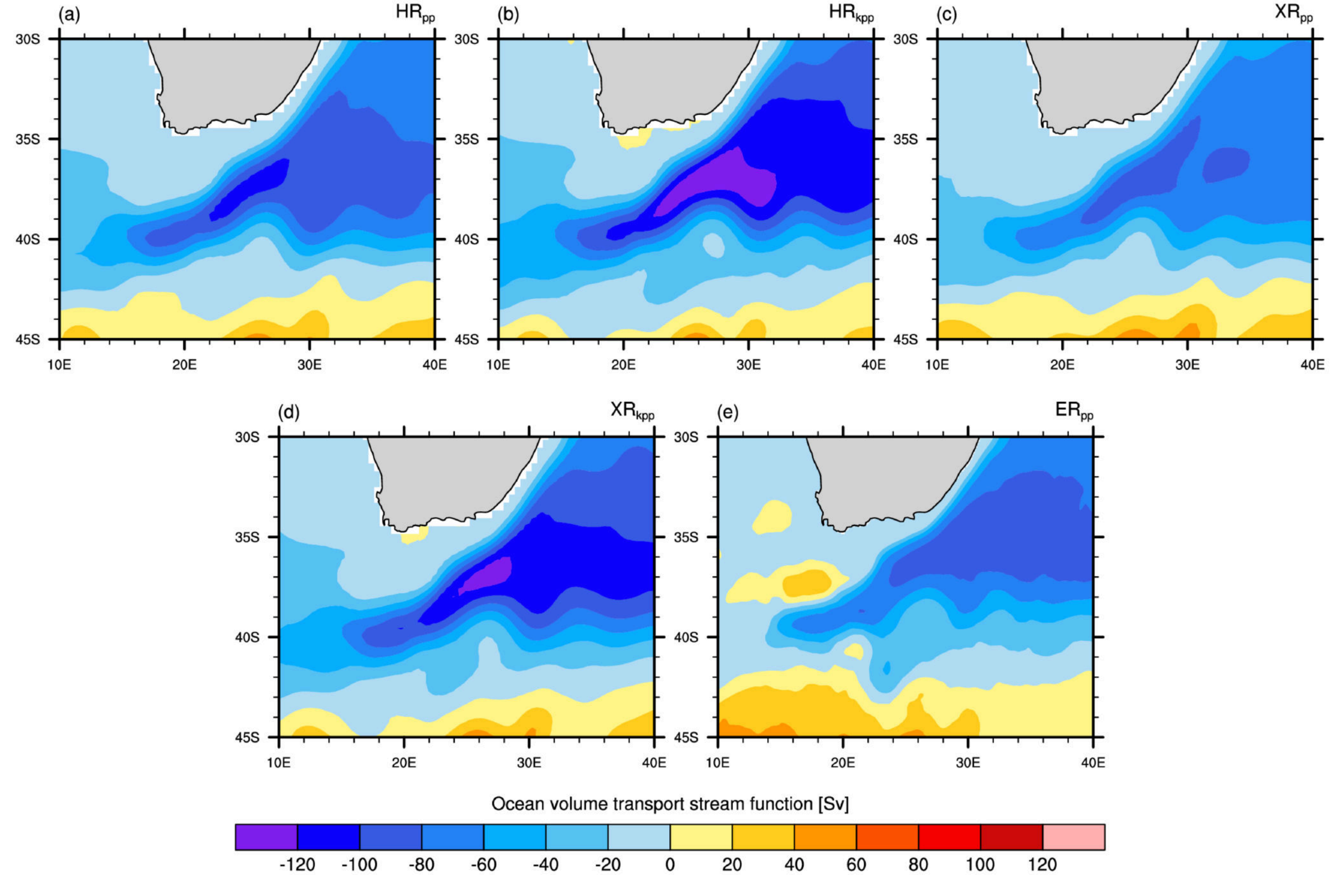

Figure A7. Time-averaged barotropic volume transport (Sv) stream function of the Agulhas Current system simulated by (a) HR_{pp}, (b) HR_{kpp}, (c) XR_{pp}, (d) XR_{kpp}, and (e) ER_{pp}.

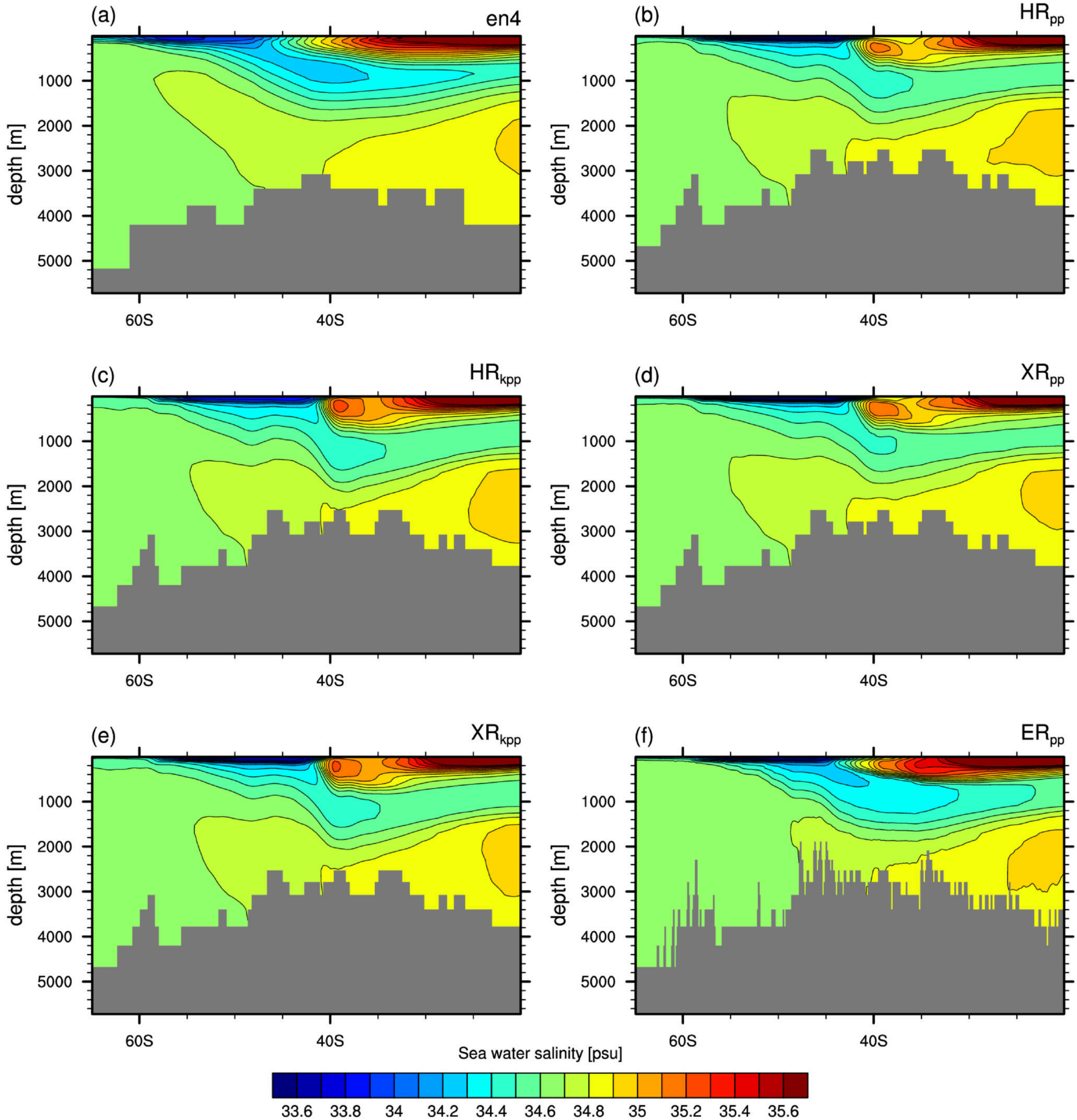

Figure A8. Time-averaged salinity section along 15°W (from 65°S to 20°S) in the Southern Ocean of (a) EN4 (1945-1955), (b) HR_{pp}, (c) HR_{kpp}, (d) XR_{pp}, (e) XR_{kpp}, and (f) ER_{pp}.

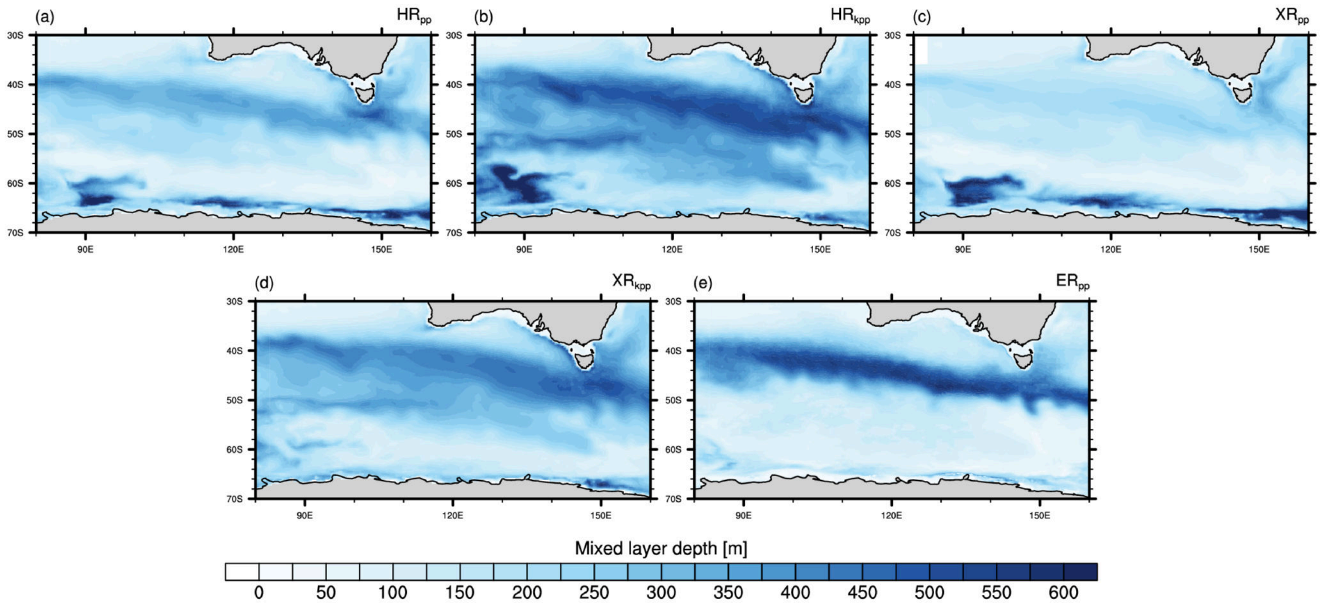

Figure A9. Time-averaged mixed layer depths ($\sigma_t = 0.03\,\mathrm{kg\,m^{-3}}$) across the Subantarctic Frontal zone in September simulated by (a) $\mathrm{HR_{pp}}$, (b) $\mathrm{HR_{kpp}}$, (c) $\mathrm{XR_{pp}}$, (d) $\mathrm{XR_{kpp}}$, and (e) $\mathrm{ER_{pp}}$.